Soft Matter

ARTICLE TYPE

Cite this: DOI: 00.0000/xxxxxxxxxx

Hierarchical Assemblies of Superparamagnetic Colloids in Time-Varying Magnetic Fields

Aldo Spatafora-Salazar,‡ Dana M. Lobmeyer,‡ Lucas H. P. Cunha,‡ Kedar Joshi,‡ and Sibani Lisa Biswal

Received Date
Accepted Date

DOI: 00.0000/xxxxxxxxxx

Magnetically-guided colloidal assembly has proven to be a versatile method for building hierarchical particle assemblies. This review describes the dipolar interactions that govern superparamagnetic colloids in time-varying magnetic fields, and how such interactions have guided colloidal assembly into materials with increasing complexity that display novel dynamics. The assembly process is driven by magnetic dipole-dipole interactions, whose strength can be tuned to be attractive or repulsive. Generally, these interactions are directional in static external magnetic fields. More recently, time-varying magnetic fields have been utilized to generate dipolar interactions that vary in both time and space, allowing particle interactions to be tuned from anisotropic to isotropic. These interactions guide the dynamics of hierarchical assemblies of 1-D chains, 2-D networks, and 2-D clusters in both static and time-varying fields. Specifically, unlinked and chemically-linked colloidal chains exhibit complex dynamics, such as fragmentation, buckling, coiling, and wagging phenomena. 2-D networks exhibit controlled porosity and interesting coarsening dynamics. Finally, 2-D clusters have shown to be an ideal model system for exploring phenomena related to statistical thermodynamics. This review provides recent advances in this fast-growing field with a focus on its scientific potential.

1 Introduction

From chains to sheets, magnetically responsive colloids can be directed into unique materials that span multiple dimensions. Under an applied external magnetic field, paramagnetic particles acquire magnetic dipoles whose interparticle interactions can be made attractive or repulsive, governing their assembly.[1,2] The direction and intensity of the field tunes these interactions and allows for the formation of different types of structures, ranging from linear[3–5] to higher-dimensional arrangements.[6–10] By increasing the complexity of the applied field and/or particles used, *e.g.* anisotropy in size and shape, researchers have accessed new colloidal assemblies with a multitude of structures, which have new properties and dynamics.[11–17] Considering spatial uniformity, the complexity of a magnetic field is defined by how it varies in time. Figure 1 depicts several configurations of applied magnetic fields that are possible with a triaxial electromagnetic coil apparatus. The complexity of magnetic particles is introduced through anisotropy in shape[13,18] and composition.[12,19] However, even simple spherical particles can be assembled into complex structures with dynamics that are far from fully explored.

In this review, the assembly of spherical superparamagnetic colloids into hierarchical structures, and their resulting dynamics under the action of time-varying magnetic fields, are discussed. In time-varying fields, magnetic colloidal systems can assemble into a multitude of structures that display novel dynamics. Under low-frequency rotating magnetic fields, colloidal chains that follow the field are realized, with lengths and phase lag angles defined by the balance between magnetic and viscous forces.[29–33] By increasing the field frequency, breakup dynamics[21,34,35] and subsequent shortening of the chains are observed.[36,37] In contrast, for high-frequency rotating magnetic fields, the attractive magnetic interactions dominate in an effectively isotropic manner. Such a phenomenon results in the formation of two-dimensional (2-D) clusters in the plane of the field.[8] By increasing field strength or particle concentration, the cluster packing fraction increases, leading to the formation of colloidal crystals.[7] This behavior is of great value to investigate fundamental problems in condensed matter physics, such as phase transitions and crystal defects.[38–40]

Hard spherical colloidal particles have long been used as analogous models for atomic and molecular systems.[38,40,41] The advantage has been that colloidal systems are of sizes that can be visualized with optical microscopy, while their dynamics are still governed by thermal energy. Colloidal systems have illustrated phenomena such as glass transition, crystallization, and melting. Paramagnetic colloids have the additional advantage in that their interactions can be tuned by an applied magnetic field. Moreover,

---

Department of Chemical and Biomolecular Engineering, Rice University, Houston, TX 77005, USA. E-mail: biswal@rice.edu; Tel: + 1 713-348-6055

‡ These authors contributed equally to this work.

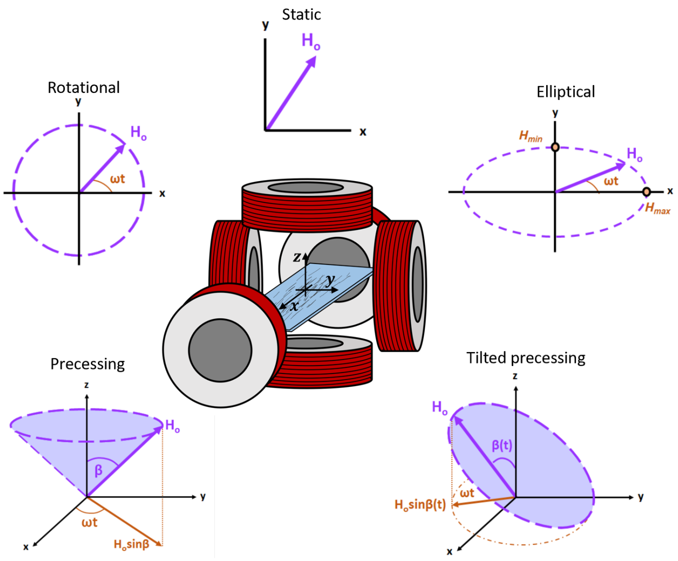

Fig. 1 Schematic representation of several types of fields that can be achieved with a set of three orthogonal and independent pairs of Helmholtz coils. The magnetic field equations for each type are presented as follows. For a static field: $\mathrm{H}_0 = H_0\hat{\mathrm{e}}$, where $\hat{\mathrm{e}}$ is a unit vector and H_0 is the field strength. For a circular field: $\mathrm{H}_0(t) = H_0[\cos(\omega t)\hat{e}_x + \sin(\omega t)\hat{e}_y]$, where $\omega = 2\pi f$ is the angular frequency of the field. For an elliptical field: $\mathrm{H}_0(t) = H_{max}\cos(\omega t)\hat{e}_x + H_{min}\sin(\omega t)\hat{e}_y$, with time-dependent strength $H_0(t) = \sqrt{H_{max}^2\cos^2(\omega t) + H_{min}^2\sin^2(\omega t)}$. For a precessing (conical) field: $\mathrm{H}_0(t) = H_{xy}[\cos(\omega t)\hat{e}_x + \sin(\omega t)\hat{e}_y] + H_z\hat{e}_z$, where $\beta = \tan^{-1}(H_{xy}/H_z)$ is the precessing angle, and the constant strength is $H_0 = \sqrt{H_{xy}^2 + H_z^2}$. For a tilted precessing field: $\mathrm{H}_0(t) = H_{xy}[\cos(\omega t)\hat{e}_x + \sin(\omega t)\hat{e}_y] + H_z\cos(\omega t + \phi_z)\hat{e}_z$, where the phase, ϕ_z, controls the direction of inclination of the field, and $\beta(t)$ corresponds to the time-dependent precessing angle. The time-dependent strength of this field is $H_0(t) = \sqrt{H_{xy}^2 + H_z^2\cos^2(\omega t + \phi_z)}$.

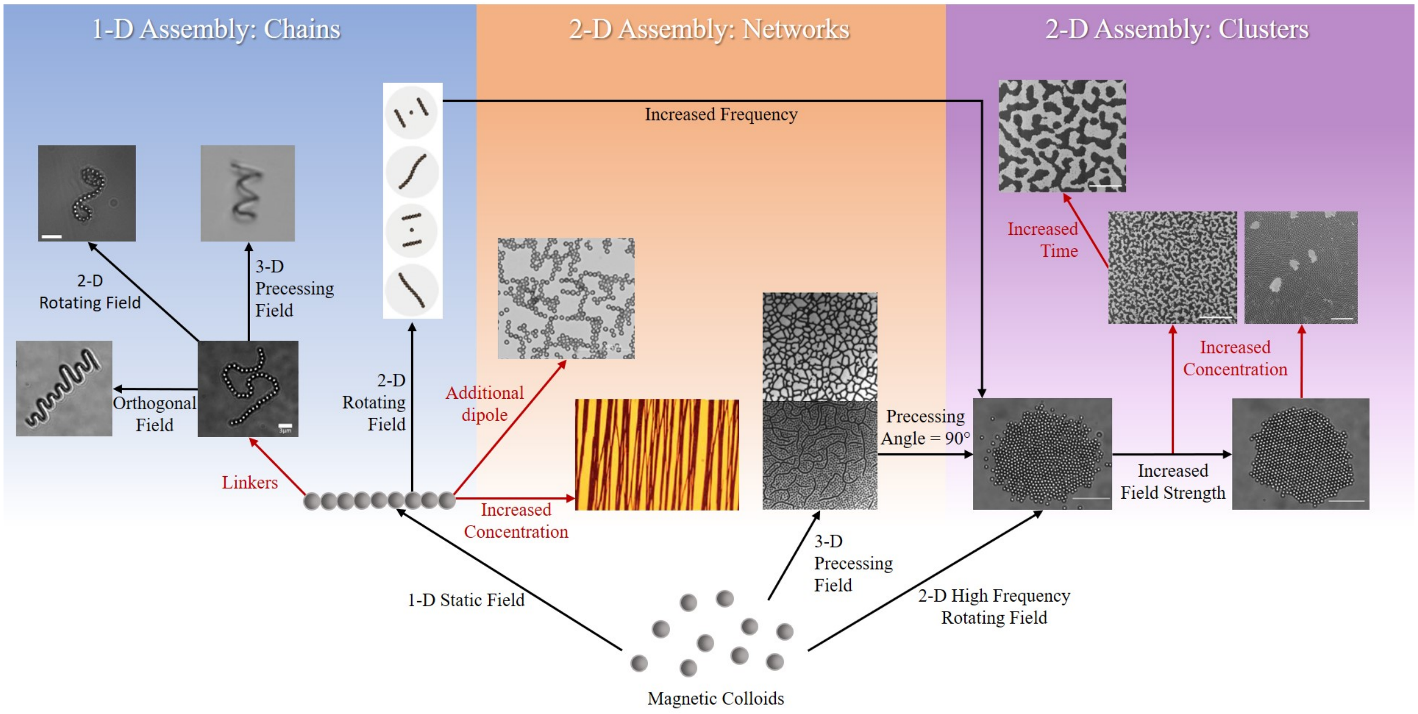

Fig. 2 Illustrative representation of the hierarchical colloidal assemblies that can be obtained with superparamagnetic colloids in static and time-varying fields. This review outlines how increased complexity spans from 1-D chains to 2-D networks and clusters. Reprinted figures with permission from ref. 20, Copyright (2017) by the American Physical Society; ref. 21, Copyright (2012) by the American Physical Society; ref. 22, Copyright (2018) by the American Physical Society; ref. 7, Copyright (2018) by the American Physical Society; ref. 23, Copyright (2014) by the American Chemical Society; ref. 24, Copyright (2014) by the American Chemical Society; ref. 25 from the Royal Society of Chemistry; ref. 26 from the Royal Society of Chemistry; ref. 27 from the Royal Society of Chemistry; and ref. 28 from PNAS.

this tunability broadens the range of colloidal assemblies that can be investigated.[42]

Aggregates of paramagnetic colloidal particles can assemble into structures of increasing hierarchy, from 1-D chains to 2-D networks and 2-D clusters. This spatial dimension refers to the hierarchy of the assembly conformation, but their dynamics can span multiple dimensions. The pathways to build these hierarchical colloidal assemblies using static and time-varying fields are illustrated in Fig. 2. This review highlights the increasing complexity in structure and dynamics that is possible with these directed colloidal assemblies. Section 2 presents background information regarding the theoretical aspects and numerical computations that describe the interactions of magnetizable particles under the action of an external magnetic field. Following the scheme presented in Fig. 2, the dynamics of chains of paramagnetic particles in static and time-varying fields are described in Sec. 3. Cross-linked chains of paramagnetic particles are then discussed in Sec. 4. These more recent assemblies display novel configurations and dynamics because of their elasticity. Section 5 is devoted to network-like structures that arise in static and precessing fields. Section 6 describes clusters formed through magnetically induced isotropic interactions. Finally, Sec. 7 provides a perspective of possible future directions of these magnetic colloidal assemblies.

2 Magnetic Dipolar Interactions

Particle magnetization, characterized by a magnetic susceptibility, is an important variable that can be used to control colloidal assembly.[2] However, magnetization will vary based on the type of magnetic particle used. Ferromagnetic particles have permanent dipoles. A common colloidal suspension of this type of particle is a ferrofluid, where magnetic nanograins are suspended in a liquid. In contrast, paramagnetic particles contain magnetic dipoles that are induced by an external magnetic field. An important aspect of paramagnetic particles is that they have no net magnetization in the absence of an applied field. Superparamagnetic colloids consist of single-domain ferromagnetic nanoparticles embedded in a diamagnetic medium, *e.g.* iron oxide nanoparticles in a polystyrene matrix. These particles present the same magnetic behavior as paramagnetic particles, but with a much higher magnetic susceptibility. Note that it is common to see superparamagnetic colloids referred to as paramagnetic colloids in the literature. For the purpose of this review, paramagnetic is used when describing the governing equations and superparamagnetic is used when describing experimental results.

This section summarizes the interactions that arise when paramagnetic colloids are placed in external magnetic fields. Understanding the magnetic interactions of paramagnetic particles, under an external magnetic field, is essential to describe the assembly dynamics of magnetic colloids. Such interactions are typically described using the dipolar model (DM), which assumes that spherical particles subjected to an external magnetic field, $\mathbf{H}_0$, acquire a uniform magnetization:

$$\mathbf{m} = \frac{4\pi a^3 \chi \mathbf{H}_0}{3} \tag{1}$$

where a is the particle radius, and $\chi = 3\chi_m/(3+\chi_m)$ is the effective magnetic susceptibility for a spherical particle, χ_m being the susceptibility of the material. Equation 1 assumes the magnetization of the particle is linearly related to the applied external field, *i.e.* far from the saturation magnetization of the particle. By treating the particle as a single dipole with magnetic moment $\mathbf{m}$ located at its center, $\mathbf{x}_0$, the magnetic field produced by the particle at the position $\mathbf{x}$ is given by:[1]

$$\mathbf{H}_{\text{dip}}(\mathbf{r}) = \frac{1}{4\pi}\left[\frac{3(\mathbf{m}\cdot\mathbf{r})\mathbf{r}}{r^5} - \frac{\mathbf{m}}{r^3}\right] \tag{2}$$

where $\mathbf{r} = \mathbf{x} - \mathbf{x}_0$ and $r = \sqrt{\mathbf{r}\cdot\mathbf{r}}$. It is important to note that Eq. 2 recovers the exact solution for the magnetic field induced by a spherical particle in a uniform magnetic field for $r > a$.[43]

In the absence of electric fields and nonsteady currents, Maxwell's equations reduce to the magnetostatic regime: $\nabla\cdot\mathbf{B} = 0$ and $\nabla\times\mathbf{H} = \mathbf{0}$, where $\mathbf{B}$ and $\mathbf{H}$ correspond to the magnetic induction field and magnetic field, respectively. These two vectorial quantities relate to each other by $\mathbf{B} = \mu_0(\mathbf{H}+\mathbf{M})$, where $\mu_0 = 4\pi\times10^{-7}$ N·A^{-2} is the magnetic permeability of free space, and $\mathbf{M}$ is the magnetization of the medium. In general, medium refers to both the particle and background solution in the event both can be magnetized. For paramagnetic materials far from the saturation magnetization, $\mathbf{M} = \chi_m\mathbf{H}$. Under such conditions, $\mathbf{B} = \mu\mathbf{H}$ and $\nabla\cdot(\mu\mathbf{H}) = 0$, where $\mu = \mu_0(\chi_m+1)$ is the magnetic permeability of the medium. Since the magnetic field is irrotational, it can be rewritten as the gradient of a magnetic potential field, ζ, such that $\mathbf{H} = -\nabla\zeta$. Therefore, the magnetic equations reduce to: $\nabla\cdot(\mu\nabla\zeta) = 0$, or more simply, $\mu\nabla^2\zeta = 0$, a Laplace equation that assumes constant magnetic permeability throughout the medium. By applying the superposition principle, the magnetic field around the particle can be expressed as $\mathbf{H} = \mathbf{H}_0 + \mathbf{H}_{\text{dip}}$.

In the magnetostatic limit, the force experienced by a dipole subjected to a magnetic field is given by $\mathbf{F}_{mag} = -\nabla U$, where $U = -\mu_0\mathbf{m}\cdot\mathbf{H}_0$ is the potential energy. In a uniform magnetic field, a single particle experiences no magnetic forces. However, neighboring particles exert forces on each other because of their induced magnetic fields. The potential energy between two interacting dipoles, $\mathbf{m}_i$ and $\mathbf{m}_j$, can be written as:

$$U_{ij} = \frac{\mu_o}{4\pi}\left[\frac{\mathbf{m}_i\cdot\mathbf{m}_j}{r_{ij}^3} - \frac{3(\mathbf{m}_i\cdot\mathbf{r}_{ij})(\mathbf{m}_2\cdot\mathbf{r}_{ij})}{r_{ij}^5}\right] \tag{3}$$

where $\mathbf{r}_{ij}$ is the distance vector between $\mathbf{m}_i$ and $\mathbf{m}_j$.

From the superposition principle, for a system of M dipoles, the magnetic force on the i^{th} dipole is a result of the magnetic interactions between all other dipoles in the system:

$$\begin{aligned}\mathbf{F}_i = -\sum_{j\neq i}^{M}\frac{3\mu_0}{4\pi r_{ij}^5}\Bigg[&(\mathbf{m}_i\cdot\mathbf{r}_{ij})\mathbf{m}_j + (\mathbf{m}_j\cdot\mathbf{r}_{ij})\mathbf{m}_i \\ &+ (\mathbf{m}_i\cdot\mathbf{m}_j)\mathbf{r}_{ij} - 5\frac{(\mathbf{m}_i\cdot\mathbf{r}_{ij})(\mathbf{m}_j\cdot\mathbf{r}_{ij})\mathbf{r}_{ij}}{r_{ij}^2}\Bigg]\end{aligned} \tag{4}$$

Continuing with the DM, Eq. 1 inherently assumes that the magnetic field is produced by a single dipole, such that Eq. 2 is not influenced by the magnetization of other particles.[33,44] By assuming this is the case, Eq. 3 can be rewritten as a function of the angle θ between $\mathbf{r}$ and the particles' parallel magnetic moments: $U_{ij} \sim [1-3\cos^2(\theta)]$. Figure 3 illustrates the relevant parameters to determine the interaction potential between two particles, according to this model. This interaction can either be attractive, $U_{ij} < 0$, or repulsive, $U_{ij} > 0$, and the transition from one to the other exists at $U_{ij} = 0$. The angle at which this occurs is $\theta = 54.7^\circ$ and is referred to as the magic angle.[43] The strongest attractive interaction occurs at $\theta = 0$, which leads to the assembly of linear chain structures, further discussed in Sec. 3. For the scope of this review, another important phenomenon arises from the application of high-frequency rotating magnetic fields. In such cases, the time period of the applied field is much shorter than the characteristic relaxation time of the particle in the background solvent. Essentially, the magnetic dipole is time-averaged over the particle, resulting in an effective isotropic interaction between particles. The equivalent potential between particles is given by $-\mu_0 m_i m_j / 4r_{ij}^3$, which is easily verified by integrating Eq. 3 with respect to θ, from 0 to 2π, *i.e.* over one period. These effective isotropic interactions result in 2-D colloidal clusters, as is further discussed in Sec. 6.

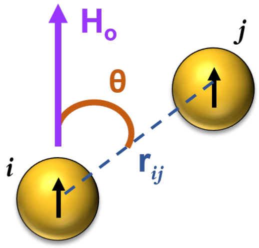

Fig. 3 According to the DM, the dipolar interactions between two spherical magnetic colloids (i and j), upon application of a uniform magnetic field, depend on the external magnetic field (H_0), the center-to-center interparticle distance (r_{ij}), and the angle (θ) formed between them. The black arrows inside the particles represent the magnetic moments (m_i and m_j), which are equal to each other and parallel to the direction of the external magnetic field.

The DM is widely used to describe the dynamics of paramagnetic colloidal systems. One motivation for using the DM is that it simplifies the analytical calculations. It also lends itself to being computationally efficient for simulating systems of thousands of particles. However, the DM assumes a constant dipole, as given by Eq. 1, and neglects the additional magnetization induced by neighboring particles. Thus, the computed magnetic forces become inaccurate, particularly when the particles are in close proximity, *i.e.* dense systems. To overcome this limitation, the mutual dipolar model (MDM) was developed to provide a better description of a particle's magnetization, while still assuming that the particles are uniformly magnetized.[45] This methodology leads to a linear system of equations. The dipole moment for particle i in a solution of N particles can be written as:

$$\mathbf{m}_i = \frac{4}{3}\pi a^3 \chi \left[\mathbf{H}_0 + \sum_{j=1, j\neq i}^{N} \mathbb{M} \cdot \mathbf{m}_j \right] \tag{5}$$

where $\mathbb{M} = (3\mathbf{r}_{ij}\mathbf{r}_{ij}/r_{ij}^5 - \mathbf{I}/r_{ij}^3)/4\pi$ is the grand potential tensor,[46] and $\mathbf{r}_{ij} = \mathbf{x}_j - \mathbf{x}_i$. Note that $\mathbb{M} \cdot \mathbf{m}_j$ results in the induced dipolar magnetic field in Eq. 2. The magnetic moments are determined by solving the linear system of equations, which can then be used to compute the magnetic force acting on each particle, according to Eq. 4. The MDM is considerably more computationally intensive when compared to the DM because of the need to solve a large system of equations ($3N \times 3N$) for each time step.[43]

Furthermore, despite the greater accuracy of the MDM when compared to the DM, particles may not have a homogeneous magnetization throughout their volume. This inhomogeneity is particularly evident for particles in close contact or anisotropic particles.[43,44] Figure 5 illustrates the inhomogeneity of the magnetic field for particles in close contact or of varying shape. For example, when two spheres are considerably close to each other, the magnetic field intensity within the spheres is highest in the region where the particles are closest. For square-shaped particles, the inhomogeneous magnetic field leads to a torque that rotates the particle. Lastly, variations in the magnetic field within ferrofluid droplets can be observed due to deformations of the interface.

The most accurate method to compute the magnetic force on each particle is to solve Maxwell's equations. This procedure involves computing the solution of the magnetic field through the system domain, followed by the integration of the magnetic force density ($\nabla \cdot \sigma^{\mathrm{M}}$) over the volume of each particle, or by the integration of the magnetic stress ($\mathbf{n} \cdot \sigma^{\mathrm{M}}$) over the surface of each particle, where σ^{M} is the Maxwell stress tensor, and $\mathbf{n}$ is the normal direction on the particle surface. To accomplish this task, different numerical methodologies can be used, such as finite element, boundary element, and finite difference methods.[47,48] The greatest challenge in applying these methods is the proper application of the boundary conditions at the particles' surfaces. Some groups have implemented a Heaviside function to smooth the interface between the particle and solvent.[49,50] When this continuous function is used in place of a discrete interface, boundary conditions are no longer necessary. Such a technique is of great value when considering anisotropic particles because it does not require further modifications.[51] Additionally, this method is straightforward for simulating soft particles, *e.g.* ferrofluid droplets.[52,53]

Du *et al.*[44] compares the solutions from the DM and MDM methodologies, where the exact solutions obtained use a numerical Laplace's equation solver (LES) with a smoothing interface technique. As shown by Fig. 5, the MDM method leads to a close estimate of the magnetic force between a pair of spherical particles; however, it deviates from the exact solution when the particles are in close proximity. Additionally, the magic angle of 54.7° only applies for the DM model. With the LES method, the magic angle becomes a function of the particle distance, *e.g.* $\approx 60^\circ$ when the interparticle distance is 10% greater than the particle diameter. Du & Biswal[54] proposed a new methodology to compute particle interactions, known as the micro-mutual-dipolar model

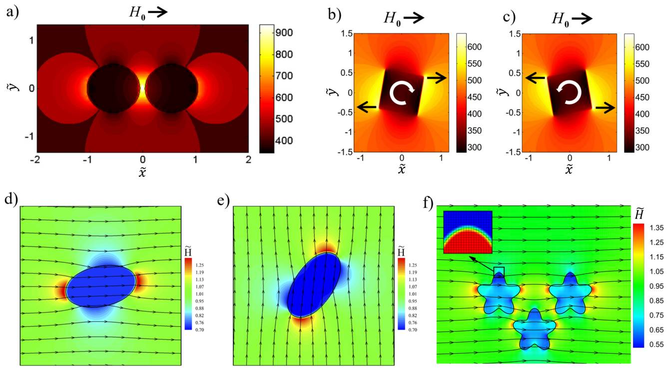

Fig. 4 a) Magnetic field intensity for a pair of interacting paramagnetic spheres subjected to a uniform magnetic field, H_0. The tilde refers to the non-dimensionalization with respect to the particles' diameter. Reprinted figure with permission from ref. 44. Copyright (2014) by the American Physical Society. b)-c) Magnetic field intensity for a paramagnetic square subjected to a uniform magnetic field, H_0. The tilde refers to the non-dimensionalization with respect to the length of the squares' sides. Reprinted from ref. 51, Copyright (2016), with permission from Elsevier. d)-e) Magnetic field lines and intensity for a ferrofluid droplet subjected to a shear flow and an external field d) parallel to and e) perpendicular to the main flow direction. The tilde refers to the non-dimensionalization with respect to the applied field strength. Reprinted from ref. 53, with the permission of AIP Publishing. f) Magnetic field lines and intensity for three interacting paramagnetic star-shaped particles subjected to an external field, where the magnetic permeability ratio equals 2. The tilde refers to the non-dimensionalization with respect to the applied field strength. The solution is obtained in a 2-D space using the finite difference method and the interface smoothed technique. The inset elucidates the smooth transition of the local magnetic permeability from inside the particle (red) to outside the particle (blue), with the squares representing the mesh discretization.

(MMDM). This methodology considers the nonuniformity of the magnetic field within the particles by shifting the magnetic moments away from their centers. Such a model presents a great improvement in accuracy when compared to the MDM, however, its implementation is not simple, and the computational cost is considerably greater.

3 1-D Chains of Superparamagnetic Colloids

Linear chains of superparamagnetic colloids are the simplest type of assemblies formed upon the application of an external magnetic field. This chain formation is due to the induced dipoles' preference to align in a tip-to-tail manner. However, the dynamics of these chains under the action of time-varying magnetic fields stray far from simplicity because of the interplay between magnetic and viscous forces. Steady rotation, breakup instabilities, higher-order fragmentation events, and structural collapse are examples of the various phenomena displayed. Through these complex dynamics, chains can form precursor structures that assemble into higher-order colloidal systems, which are presented in Sec. 5 and Sec. 6.

This section begins with a description of the magnetic forces involved in the thermodynamics and kinetics of colloidal chain assembly. Next, the growth kinetics are emphasized because they determine the average chain length, which governs chain dynamics. Lastly, the core of this section focuses on detailing the dynamics of colloidal chains exposed to circular time-varying magnetic fields.

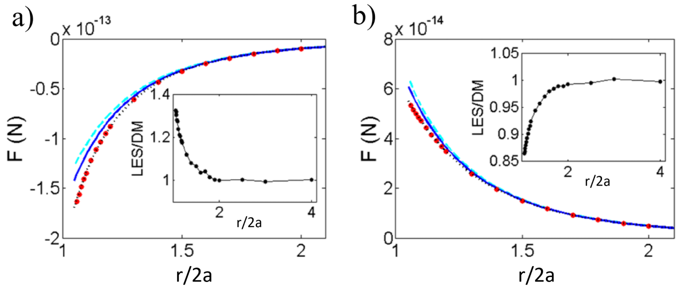

Fig. 5 a)-b) Magnetic forces between a pair of paramagnetic spheres, subjected to an external field that is applied a) parallel and b) perpendicular to their distance vector. The forces are computed with the DM (light blue dashed lines), MDM (dark blue solid lines), and LES (red dots), as a function of the interparticle distance, r, normalized by the particle diameter, $2a$. Negative values represent attractive interactions and positive represent repulsive. The insets in both graphs display the ratio of the force computed with LES to the force computed with the DM. Reprinted figures with permission from ref. 44. Copyright (2014) by the American Physical Society.

3.1 Chain assembly

3.1.1 Principles of chain formation

As described in Sec. 2, paramagnetic particles acquire dipole moments parallel to the direction of the magnetic field and begin to interact with each other through the pair potential described by Eq. 3. The magnetic moments acquired by the colloids can be approximated by the dipolar model (DM) from Eq. 1. As a result, the magnetic interactions between two identical superparamagnetic particles can be expressed in terms of a particle's moment, m, and the angle, θ, between the external field and the interparticle separation, $\mathbf{r}_{ij}$:

$$U_{ij}(r_{ij},\theta) = \frac{\mu_o m^2}{4\pi r_{ij}^3}\left[1 - 3\cos^2\theta\right] \tag{6}$$

where $\cos\theta = \mathbf{m}\cdot\mathbf{r}_{ij}/mr_{ij}$.

As shown in Fig. 6, the interactions between paramagnetic colloids are governed by θ. The strongest repulsion and attraction between two particles occurs when their dipoles are arranged side-by-side ($\theta = 90°$, Fig. 6a) and head-to-tail ($\theta = 0°$, Fig. 6b), respectively. The potential energy in Eq. 6 vanishes at the magic angle ($\theta_{\text{magic}} = 54.7°$). Above this threshold ($\theta_{\text{magic}} < \theta \le 90°$), the particles become repulsive, whereas below the threshold ($0° \le \theta < \theta_{\text{magic}}$) they are attractive,[55] with a minimum at $\theta = 0°$. Thus, this pair interaction potential is spatially anisotropic.[56] As a result of these interactions, the j^{th} particle exerts a magnetic force on the i^{th} particle with radial and tangential components described by:

$$F_i^r(r_{ij},\theta) = \frac{3\mu_o m^2}{4\pi r_{ij}^4}(1 - 3\cos^2\theta) \tag{7}$$

$$F_i^\theta(r_{ij},\theta) = -\frac{3\mu_o m^2}{4\pi r_{ij}^4}\sin(2\theta) \tag{8}$$

These magnetic forces drive the organization of the particles into chains aligned with the field direction,[57] as shown in Fig. 6c.

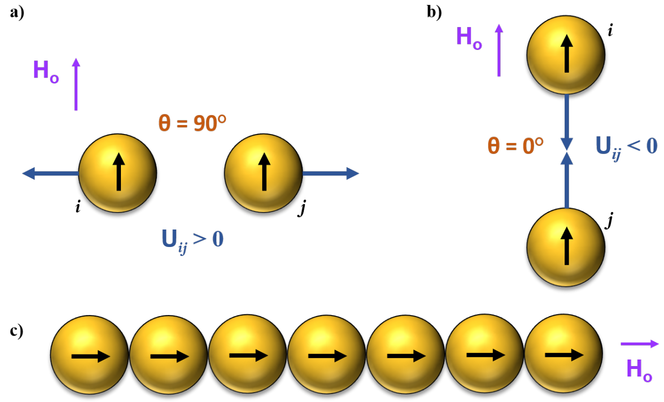

Fig. 6 Dipolar interactions are anisotropic based on the angle (θ) between the external magnetic field and the interparticle separation. a) Two dipoles aligned side-by-side ($\theta = 90°$) experience the strongest repulsion ($U_{ij} > 0$). b) Two dipoles aligned head-to-tail ($\theta = 0°$) experience the strongest attraction ($U_{ij} < 0$). c) The particles assemble into chains because the head-to-tail alignment of the dipoles minimizes the dipolar interactions.

Oftentimes, the colloids have surface coatings that render them electrostatically charged. In such cases, the interparticle spacing between two particles is dictated by the balance between the attractive magnetic forces (Eq. 7) and repulsive surface forces.[58,59] This property has been previously utilized to accurately measure short-ranged electrostatic or steric forces using micron-sized particles.[60,61] For a long chain of N particles, rather than a pair, the total radial magnetic force acting on each bead can be approximated using the scheme proposed by Zhang & Widom[62] for an infinitely long chain of equally spaced particles:

$$F^r_{i,\text{total}}(r_{ij}, \theta = 0°) = -1.202\frac{3\mu_o m^2}{2\pi r_{ij}^4} \tag{9}$$

Equation 9 is derived from the total magnetic interaction potential for a particle in such a chain: $U_{ij}(r_{ij},\ \theta = 0°) = -\mu_o m^2/2\pi r_{ij}^3 \sum_{k=1}^{\infty} 1/(k-1)^3$, where $\sum_{k=1}^{\infty} 1/(k-1)^3 \approx \sum_{k=1}^{\infty} 1/k^3 = \xi(3) = 1.202$ is the Riemann-Zeta function.

The competition between magnetic and thermal forces is measured in terms of the dimensionless magnetic coupling parameter (λ):[63]

$$\lambda = -\frac{U_{min}}{k_B T} = \frac{\mu_o \pi a^3 \chi^2 H_0^2}{9 k_B T} \tag{10}$$

where k_B is the Boltzmann constant, T is the temperature of the fluid, and U_{min} is the strongest attraction between two beads, computed from Eq. 6 as $U_{min} = U_{ij}(r_{ij} = 2a,\ \theta = 0°)$. For $\lambda < 1$, thermal fluctuations dominate over magnetic interactions, inhibiting the particle aggregation process. This situation occurs when applying weak fields to particles with low χ. In contrast, for $\lambda > 1$, the magnetic interactions dominate over thermal fluctuations, making the formation of chains possible. However, this formation is not guaranteed when working at $\lambda \sim 1$ and with very low particle concentrations.[56,64] Upon removal of the external field, superparamagnetic particles lose their net magnetization instantaneously, such that thermal fluctuations cause the disassembly of the chains and the redispersion of colloids in the fluid.[57,63] Alternatively, ferromagnetic particles retain a net magnetization under zero-field conditions. If the residual dipolar interactions are strong enough such that $\lambda > 1$, then the ferromagnetic chain structures persist. The competition between the residual magnetization and thermal fluctuations drive the reorganization of the ferromagnetic chains into bent configurations, and eventually, some close into rings or lassos.[4,65,66]

3.1.2 Chain aggregation kinetics

Although the magnitude of λ indicates that the formation of chains is possible, this parameter by itself does not provide any information about how fast the assembly occurs. The chaining process itself is not immediate because several length-scales and time-scales become relevant when defining the overall mechanism of chain growth. During field-induced aggregation, multiple chains of different sizes are formed throughout the sample, leading to a polydisperse size distribution that broadens over time as new particle-particle, particle-chain, and chain-chain coalescence events transpire.[67,68] However, the average length evolves with time. Hence, the amount of time a suspension is exposed to a static field will dictate the possibility of finding a chain of a desired size for subsequent single-level actuation dynamics. Length is a characteristic property of the chain-like structure that alters the dynamical behavior during actuation with a time-varying field. The importance of length will become more evident in Sec. 3.2 and 4.2. Therefore, characterizing the kinetics of chain assembly represents the first step in probing novel types of dynamical complexity in magnetic colloids.

The kinetics of field-induced chain assembly can be described as either diffusion-limited or deterministic (ballistic) cluster aggregation, based on two relevant length-scales.[56,70] The first of these length-scales is the capture radius, the interparticle separation at which the attractive dipolar interactions (for $\theta < 54.7°$ in Eq. 6) are equal to the thermal energy, $k_B T$:[71]

$$R_c = [4(3\cos^2\theta - 1)]^{\frac{1}{3}} a \lambda^{\frac{1}{3}} \tag{11}$$

Particles separated beyond this threshold are not influenced by one another. Therefore, such particles must rely on random diffusion to bring them to a distance shorter than R_c. Within R_c, the magnetic interactions dominate, changing the particle motion from diffusive to ballistic, which drives head-to-tail aggregation.[69] The threshold distance R_c decreases with θ and has a maximum value at $\theta = 0°$. This maximum value, R_1, only depends on the magnetic coupling parameter and the particle size:

$$R_1 = 2a\lambda^{\frac{1}{3}} \tag{12}$$

The second important length-scale, R_0, defines the initial average interparticle spacing of the randomly distributed suspension prior to field exposure:

$$R_0 = \begin{cases} \sqrt{\pi} a/(\phi_{3D})^{1/3}, & \text{for 3-D systems} \\ \sqrt{\pi} a/(\phi_{2D})^{1/2}, & \text{for 2-D systems} \end{cases} \tag{13}$$

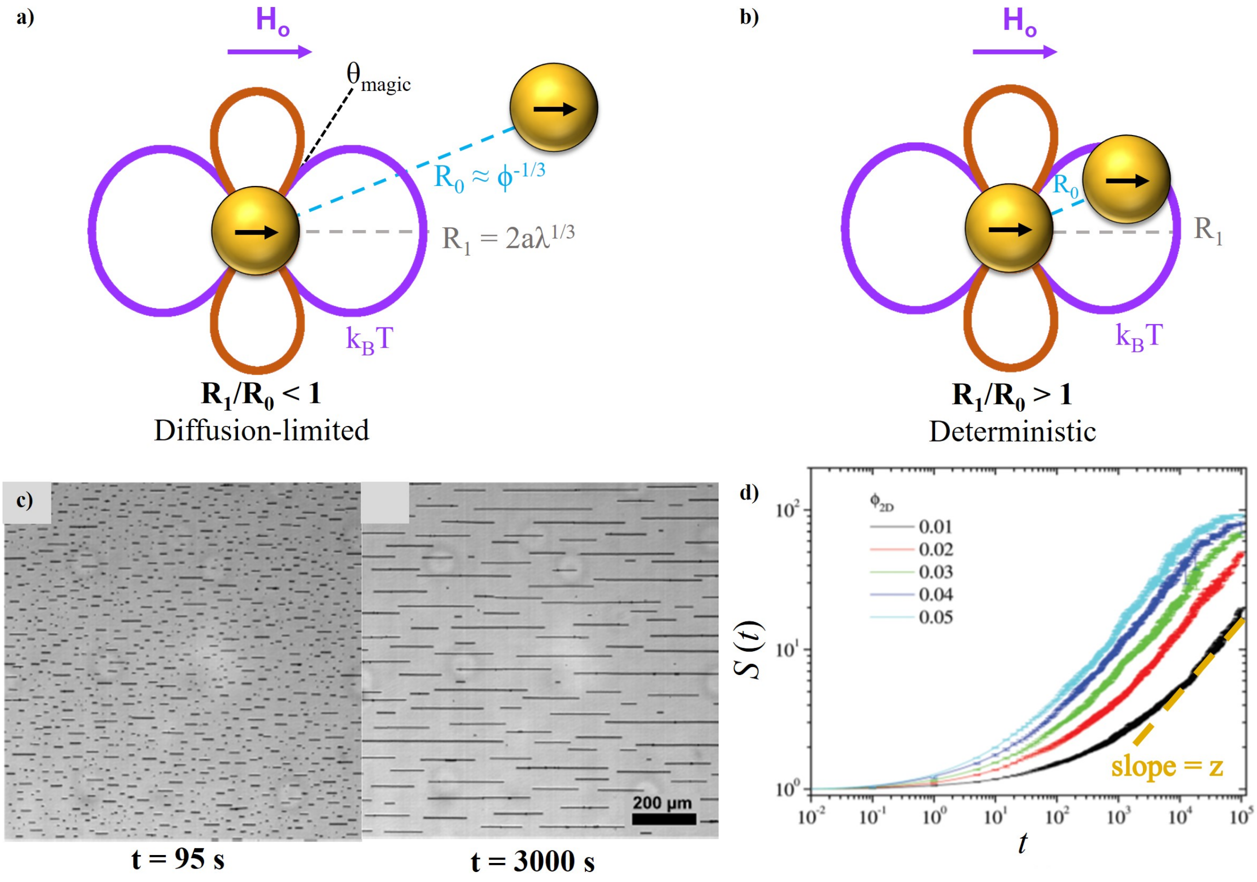

Fig. 7 Kinetics of superparamagnetic particle aggregation into linear chains under the application of a uniform, static magnetic field, H_0. a) Schematic of diffusion-limited aggregation between two particles, characterized by $R_1 < R_0$. b) Schematic of deterministic aggregation kinetics between two particles, characterized by $R_1 > R_0$. The interactions in a) and b) are modeled in terms of a capture volume, defined by the interaction potential U_{ij}, that has an attractive region (enclosed in purple) and a repulsive region (enclosed in orange). c) Experimental observation of deterministic chain kinetics. Reprinted from ref. 69, with the permission of AIP Publishing. d) Log-log plot of the size-weighted average chain length, $S(t)$, as a function of t for different particle fractions in deterministic aggregation. At long times, $S(t)$ grows linearly with t and the slope corresponds to the dynamic exponent z. Adapted from ref. 70 with permission from the Royal Society of Chemistry.

where ϕ_{3D} and ϕ_{2D} are the volume and surface packing fractions, respectively.[72,73] In experiments, the first definition (for 3-D systems) is applicable for particles that diffuse unrestrictedly and for which gravity is negligible compared to thermal fluctuations. The second definition of R_0 (for 2-D) systems is employed for dense particles that sediment to a quasi-2-D plane and remain confined due to negligible out-of-plane fluctuations. If $R_1/R_0 \leq 1$, and equivalently $\lambda\phi_{3D} \leq (\sqrt{\pi}/2)^3$ for 3-D and $\lambda^{1/3}\phi_{2D}^{1/2} \leq \sqrt{\pi}/2$ for 2-D, the thermal energy dominates over magnetic interactions, such that the colloidal system follows diffusion-limited cluster-cluster aggregation (DLCA) kinetics.[55] Else if $R_1/R_0 > 1$, the magnetic interactions dominate over the thermal energy, such that the kinetics are deterministic and therefore, faster than the DLCA scenario.[69,74] However, even for the deterministic case, chaining does not occur immediately because of the viscous drag acting on the particles. Schematics illustrating the relevant length-scales for both types of kinetics are presented in Fig. 7a and b. Overall, the transport process that leads to chain formation is completely defined by λ and ϕ, since the relevant length-scales (R_1 and R_0) depend on these two parameters.

Both kinetic mechanisms have corresponding characteristic time-scales that represent the amount of time required for two magnetic particles to form a dimer.[75] For the diffusion-limited case, this time is defined as $t_B \sim a^2/D\lambda\phi$,[71,76,77] with D being the diffusion coefficient of a single bead. On the other hand, the characteristic time for ballistic aggregation behaves as $t_{det} \sim a^2/D\lambda\phi_{2D}^{5/2}$ (or $t_{det} \sim a^2/D\lambda\phi_{3D}^{5/3}$ for 3-D). This expression was initially derived from a force balance between Stokes' drag and the maximum magnetic force acting on the particle (Eq. 7).[75,78] Note that from this point forward, ϕ refers to ϕ_{2D} because the systems in reference are confined to a quasi-2-D plane.

The temporal evolution of the elongated structures in the suspension is usually assessed in terms of the size-weighted average chain length, $S(t) = \sum_N N^2 G_N(t)/NG_N(t)$, where N is the number of particles within a chain, and $G_N(t)$ is the total number of chains containing N particles at time t.[79] Experimentally, this statistical measurement can be computed via image processing of optical microscopy, such as the snapshots in Fig. 7c, or from the effective diffusion coefficient of the aggregates, determined with dynamic light scattering (DLS).[67,80,81] After a short-time transient regime of practically null growth determined by the characteristic time-scale, $S(t)$ scales as a power law, $S(t) \sim t^z$, for intermediate to long times. The dynamic scaling exponent, z, measures the steady growth rate of the chains and is determined from the slope of the linear region of the log-log plot of $S(t)$ and t,[82] as shown in Fig. 7d. Furthermore, curves of $S(t)$ and t can be collapsed into a single master curve that fully characterizes the kinetics by using the appropriate characteristic time-scale (t_B or t_{det}).

Early DLCA theoretical studies predicted that $z = 1/2$ for 2-D and 3-D aggregation, and $z = 1/3$ for the low limit of 1-D aggregation, based on the assumption that the drag coefficient of a chain increases linearly with the number of particles.[83,84] Subsequent experiments and simulations showed that $z = 0.6$ for 2-D chains. This deviation is a result of the anisotropic shape of the chains.[85,86] For ballistic aggregation, theory predicts that $z = 2/3$;[69] though a broad range of values, as high as $z = 1.01$ and as low as $z = 0.12$, have been reported.[87,88] The impact of salt concentration, surfactant, and confined spaces on z and $S(t)$ have also been analyzed recently,[68,73,74,81,89] allowing for more control over the average chain size.

3.1.3 Lateral chain aggregation

Lateral chain aggregation is a long-time coarsening process that is a result of short-range attractive interactions between neighboring chains. If the chains are within a certain distance from one another, bundling occurs at large ϕ and λ, *i.e.* when $S(t)$ saturates. Furst *et al.*[90] studied the lateral aggregation kinetics of two chains using the Halsey-Toor (HT) equation to calculate the magnetic field around an infinite chain of dipoles:

$$H(r_l, y) = -(2\pi)^2 \left(\frac{m}{4\pi\mu_0 r_l^2 a} \right) \left(\frac{a}{r_l} \right)^2 \exp\left(\frac{-2\pi r_l}{a} \right) \cos\left(\frac{2\pi y}{a} \right) \tag{14}$$

where r_l is the lateral separation between two chains, y is the position along the chain in the applied field direction, and m is defined according to Eq. 1.

The lateral interactions between two rigid chains can be calculated by integrating Eq. 15 with respect to y for infinitely long chains:

$$U_l(r_l) = \pm(2\pi)^2 \frac{2m^2}{4\pi\mu_0 r_l^2 a} \exp\left(\frac{-2\pi r_l}{a} \right) \tag{15}$$

Since both the field and interaction potential are periodic in space, particles out-of-registry are attractive and particles in-registry are repulsive, as shown in Fig. 8a. However, the HT model applies to perfectly rigid chains. For colloidal chains that exhibit thermal fluctuations, there are instantaneous changes in the particle dipoles that enhance long-range attraction between two colloidal chains. These interactions are analogous to the London and Keesom dispersion forces observed in molecular systems. Furst *et al.*[90] and Laskar *et al.*[91] derived more detailed models based on statistical fluctuations that account for these attractive interactions, resulting in a long-term coarsening of the chains with a power law of $t^{0.75}$. Figure 8b illustrates the different degree of lateral aggregation as the applied magnetic field increases.

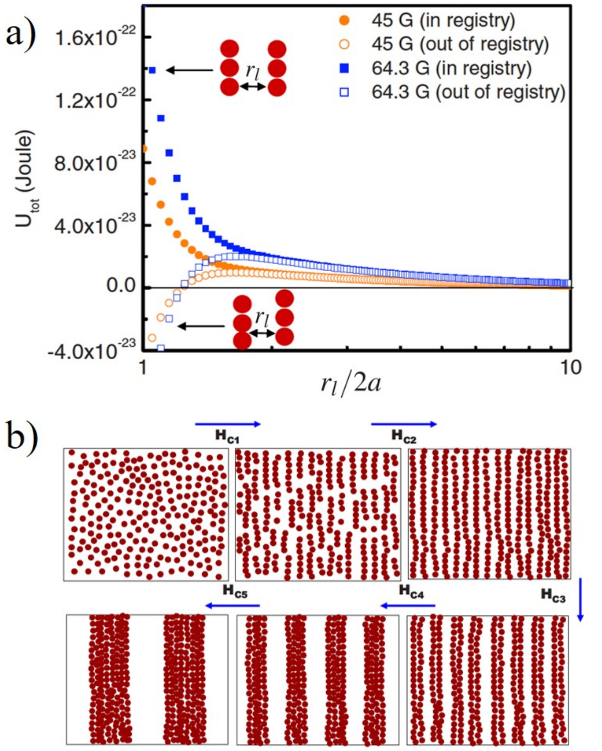

Fig. 8 a) Interaction energy between two chains, each containing 50 superparamagnetic particles, as a function of their lateral spacing. The energy values are calculated for two fields and two chain configurations: in-registry and out-of-registry. The insets depict the two types of chain configurations. b) Schematic of superparamagnetic particle arrangement before, and after, magnetic field application for increasing field strengths. Reprinted figures with permission from ref. 91. Copyright (2009) by the American Physical Society.

3.2 Chain dynamics in circular time-varying magnetic fields

The previous section, Sec. 3.1, focused on chain dynamics in the form of assembly and aggregation kinetics in static magnetic fields. When time-varying magnetic fields are utilized, the dynamics of these paramagnetic particle chains take on a host of complex phenomena. One of the simplest time-varying magnetic fields is the rotating magnetic field, defined by two sinusoidal waves that are separated by a phase of $\pi/2$:

$$\mathbf{H}_0 = H_0 \begin{bmatrix} \cos(\omega t)\hat{\mathbf{e}}_x \\ \sin(\omega t)\hat{\mathbf{e}}_y \end{bmatrix} \tag{16}$$

where H_0 is the field strength, and ω is the angular frequency of the magnetic field.

Chains of paramagnetic particles undergo rotational motion at low frequencies. The resultant dynamics depend on the external field parameters, the magnetic nature of the particles, and the rheological properties of the continuous phase. For a Newtonian medium, these dynamics are captured by the Mason number, a dimensionless quantity that gives the ratio between viscous and magnetic forces, defined as:

$$\text{Ma} \equiv \frac{72\eta\omega}{\mu_o \chi^2 H_0^2} \tag{17}$$

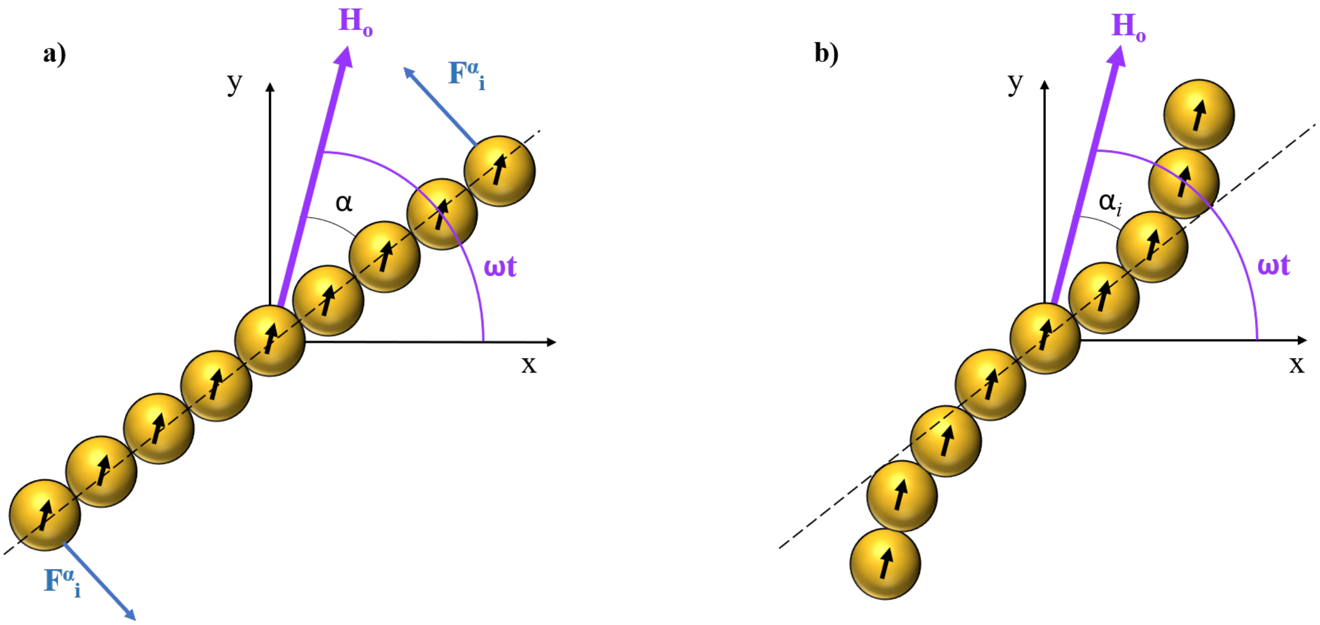

Fig. 9 Schematic of chain configurations of paramagnetic particles in circular time-varying magnetic fields. Chain orientation is determined by the field angle, ωt, where ω is the angular frequency of the field and t is time. a) The linear chain model assumes the driving tangential forces act only on the terminal particles, resulting in a single phase lag angle, α. b) More accurately, the rotating chain adopts an S-shaped configuration with a phase lag angle, α_i, for each particle pair. The largest α_i occurs at the center of the chain. Compared to the linear model, the S-shaped chain experiences deviations from the theoretical Ma_c.

---

where η is the viscosity of the solvent. The prefactor in Ma depends on the assumptions used for the Stokes' drag and magnetic forces. For example, the prefactor of 72 in Eq. 17 describes the breakup of dimers when $\mathrm{Ma} > 1$. Thus, large differences in the Mason number can be found in the literature under the same experimental conditions. Furthermore, modifications to this definition have been proposed for charged suspensions (and validated experimentally) to account for greater interparticle spacing ($r_{ij} > 2a$) caused by repulsive electrostatic forces between the particle surfaces.[92]

A chain rotates due to a magnetic torque that seeks to realign the dipoles and ultimately minimize the potential energy (see Eq. 6). An opposing viscous torque impedes complete alignment between the chain's long-axis and the external magnetic field. Consequently, the chain's orientation follows behind the external field with a phase lag angle, α, as shown in Fig. 9a. Since α defines the linear chain orientation with respect to the external magnetic field, it therefore describes the angle between the interparticle spacing and the external field for all particle pairs along the chain. Consequently, α can be substituted for θ for all angular dependencies in the magnetic interactions and forces induced by time-varying magnetic fields.

To understand α, it is necessary to analyze the magnetic and viscous torques acting on the chain. The chain is modeled to be rigid and linear,[34,93] where the particles remain in close contact, but do not overlap. In this sense, the dynamics of the chain depend exclusively on the forces perpendicular to its main axis. Moreover, each particle is treated as a point dipole with a magnetic moment, **m**, located at its center, calculated using the DM. Lastly, the particles only interact with their nearest neighbors. Following these assumptions, the net magnetic force on a particle within the chain is zero, because the neighboring particle interactions cancel each other. The exception is the terminal particles, which have opposing tangential forces, F_i^{α} (Eq. 8), as shown in Fig. 9a. The magnetic torque based on this model is:

$$\Gamma_m = 2F_i^{\alpha}\left(2a\frac{N}{2}\right) = \frac{1}{6}\pi N a^3 \mu_o \chi^2 H_0^2 \sin(2\alpha) \tag{18}$$

where N is the number of particles. Note that different expressions for the magnetic torque have been reported in the literature based on varying assumptions of the tangential dipolar force and chain length.[29,94,95]

The viscous torque on a chain can be determined using a shish-kebab model for N aligned spheres in contact:[96]

$$\Gamma_v = \frac{8\pi a^3 N^3 \eta}{3\ln(N/2)}\frac{\mathrm{d}\theta_L}{\mathrm{d}t} \tag{19}$$

where $\mathrm{d}\theta_L/\mathrm{d}t$ is the angular velocity of the chain, and θ_L is the angle between the chain orientation and the reference axis. Note that θ_L can be also expressed in terms of the field angle, ωt, and α: $\theta_L = \omega t - \alpha$. The balance between magnetic and viscous torques leads to a nonlinear differential equation for α, given by:

$$\frac{\mathrm{d}\alpha}{\mathrm{d}t} = \omega - \frac{\mu_o \chi^2 H_0^2 \ln(N/2)}{16\eta N^2}\sin(2\alpha) \tag{20}$$

Note that this expression is for $\lambda > 1$ and low Reynolds numbers, where thermal and inertial forces can be neglected. Solutions to this equation are given by Singh *et al.*[93] and Petousis *et al.*[34] At steady-state, the chain rotates with the same frequency as the external magnetic field. Therefore, α can be expressed in terms of N and Ma:[20]

$$\sin(2\alpha) = \frac{2\text{Ma}N^2}{9\ln(N/2)} \tag{21}$$

Longer chains rotate with a larger α because length increases the drag force. In addition, α increases with η and ω, whereas it decreases with H_0.

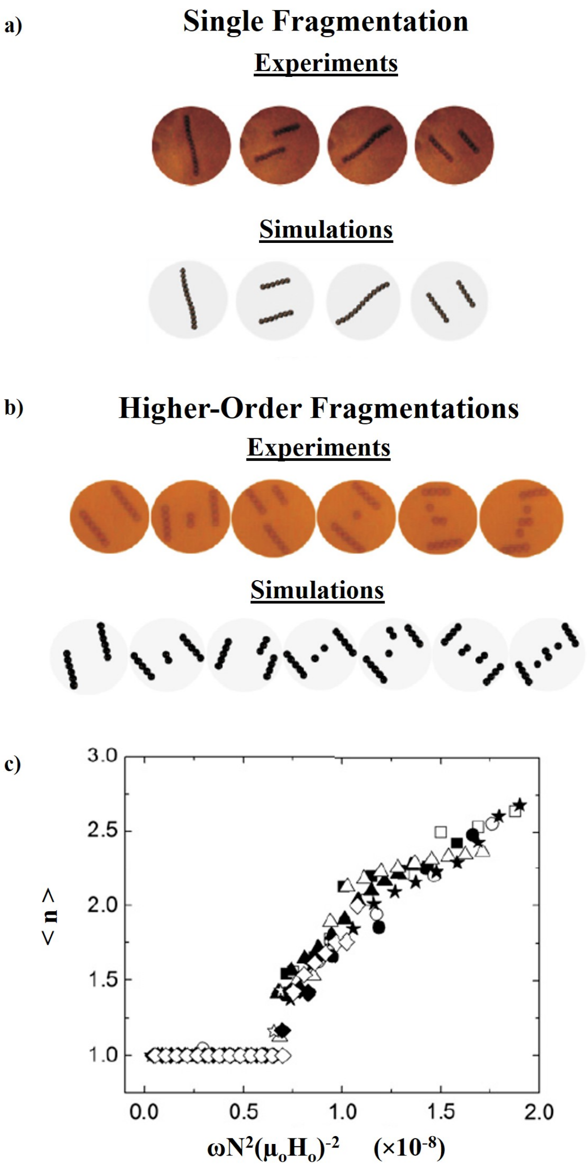

Fig. 10 Fragmentation dynamics of superparamagnetic chains under the action of an external rotating magnetic field at high Ma. a) Experiments and simulations of single fragmentation in a $N = 13$ chain, occurring above Ma_c. b) Higher-order fragmentation of an $N = 12$ chain at Ma $>$ Ma_c of the original chain length. Images a) and b) reprinted with permission from ref. 21. Copyright (2012) by the American Physical Society. c) Master curve predicting the time-averaged number of fragments, $\langle n \rangle$, as a function of the rescaled frequency, $\omega N^2(\mu_o H_0)^{-2}$. At sufficiently low values, the chain rotates synchronously with the external field as a single intact object. Adapted from ref. 97 with permission from PNAS.

The regime of synchronous rigid-rod rotation is restricted to relatively low Ma. As Ma increases, α rises, increasing Γ_m until the chain reaches the critical phase lag value of $\alpha_c = \pi/4$. This threshold represents the limit between steady phase-locked rotation and chain instability. Substituting the critical angle in Eq. 21 yields a critical Ma, at which a chain of length N^* breaks symmetrically at its midpoint:[30,31,33,34]

$$\text{Ma}_c = \frac{9}{2}\frac{\ln(N^*/2)}{N^{*2}} \tag{22}$$

Above Ma_c, the magnetic torque is not sufficient to rotate the chain with the same angular velocity as the external magnetic field, resulting in a continuous increase in α . Once α reaches the magic angle of $\alpha_{magic} = 54.7°$, the radial magnetic restoring forces vanish (Eq. 7), culminating in chain breakup. Ma_c delineates the separation between the synchronous and unsteady regimes. However, thermal fluctuations may drive a chain to rupture below Ma_c. Because of these fluctuations, a metastable chain regime exists over a range of phase lag angles.[33]

There have been a number of deviations from Eq. 22 demonstrated in both experiments and numerical simulations. The previous analysis assumes a linear shape, which is only valid at low Ma. However, as Ma increases, the relative motion of each particle results in phase lag angles that vary along the chain, leading to an S-shaped configuration.[33,34] As shown in Fig. 9b, the terminal particles of a chain are able to follow the external rotating magnetic field more closely than the center section of the chain.[33,95] At the center of the chain, the interparticle interactions are weakest, and therefore, α is largest. Thus, the chain ruptures symmetrically (at its midpoint) and forms daughter chains that can synchronously rotate with the external field because of a smaller viscous torque.[30,31,33,34] This interesting phenomenon of cyclical chain breakup and reformation is shown in Fig. 10a.[21,35] Furthermore, the chains can also break up asymmetrically (off-center) as a result of nonuniform magnetic properties among the particles.[34]

Breakup at multiple points along the chain is possible at Ma $>$ Ma_c.[21] A single chain may fragment into multiple daughter chains to achieve synchronous rotation, as shown in Fig. 10b. Such higher-order fragmentation occurs because the operating Ma exceeds the Ma_c of the daughter chains obtained in a single breakup event. Breaking a chain into multiple fragments has been shown to enhance mixing via chaotic advection in microfluidic devices.[35] Thus, characterizing the breakup according to external field parameters is of practical importance. By varying different parameters, Sing *et al.*[97] showed that the time-averaged number of fragments, $\langle n \rangle$, could be collapsed onto a master curve when scaled with a normalized frequency ($\omega N^2(\mu_o H_0)^{-2}$), as shown in Fig. 10c.

Lastly, chain collapse is observed for even higher Ma. In such cases, the fast field frequency results in time-averaged dipolar interactions. As shown by Fig. 11a, a chain rearranges into a 2-D cluster with increasing field frequency. The pathway from a chain to a cluster displays unique dynamics and depends on the chain length. Shorter chains exhibit a do-si-do and other unstable dynamics, whereas longer chains curl at the ends and ultimately coil into cluster configurations, as shown in Fig. 11b. These attractive interactions are pseudo-isotropic with a limited angular

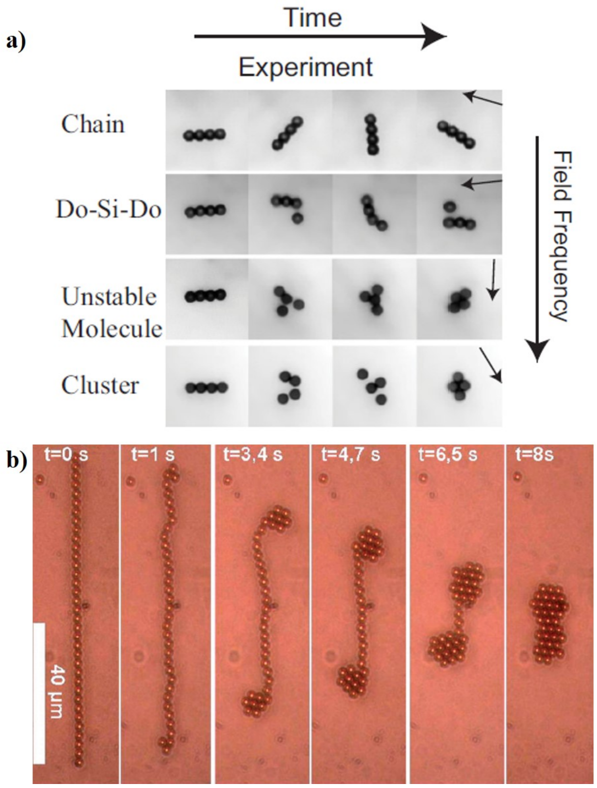

Fig. 11 Superparamagnetic chains can transition to clusters at high Ma, via different pathways determined by the chain length. a) Short chain: a chain of $N = 4$ transitions from synchronous rotation to asynchronous rotation and eventual collapse into a stable cluster at a high field frequency. Reprinted figure with permission from ref. 37. Copyright (2018) by the American Physical Society. b) Long chain: the ends of a chain with $N = 35$ initially curl to form equilateral triangular conformations that then grow and coil towards the center. This coiling causes the transition from a 1-D chain to a 2-D cluster-like assembly. Reprinted from ref. 36 with permission from IOP Publishing.

dependence. The dynamics of these 2-D cluster assemblies are discussed in more detail in Sec. 6.

While Ma_c in Eq. 22 is a good predictor of chain breakup, its value can deviate considerably from experimental and computational results because of inherent assumptions in the torque calculations. Recent analytical models of Ma_c have been developed to account for lubrication forces between neighboring particles, as well as additional corrections to the shish-kebab approximation of the viscous torque.[95] These models accurately predict chain fragmentation under a variety of conditions.

4 Cross-linked 1-D Superparamagnetic Chains

Thus far, the dynamics have been analyzed for chains that can be disassembled when the external field is removed. More recently, colloidal particles have been cross-linked to result in chains that persist in the absence of a magnetic field. Chemical and physical cross-linking methods can be used to confer elasticity to the chains. Introducing elasticity further complicates the observed dynamics in time-varying magnetic fields. Elastic resistance develops novel modes of motion such as buckling instabilities and asynchronous rotation. Interest in harnessing these magnetoelastic dynamics has led to advanced microrobotics, as well as analogous polymer-like systems.

In this section, different linking strategies are first introduced. Afterward, the discussion focuses on the increased structural and dynamical complexity of these chains under static and time-varying magnetic fields. Finally, applications of both linked and unlinked chains are presented to showcase the practical relevance of colloidal chain dynamics.

4.1 Chain cross-linking strategies

The chain structures of superparamagnetic particles can be preserved upon removal of the external magnetic field if neighboring particles along the chain backbone are physically or chemically bonded during the assembly procedure. These linking strategies provide elasticity to the overall chain structure. For instance, under a strong magnetic field and sufficient screening of electrostatic repulsion, particles align in close proximity and become physisorbed to one another because of attractive van der Waals interactions, resulting in rigid chains.[77,98] Another type of physical adhesion consists of the adsorption of polymers to the surface of the particles, followed by entanglement of these polymers during field alignment. This process yields semiflexible chains whose stiffness decreases with the molecular weight of the polymer.[99,100] Lastly, Huang *et al.* reported that aligned superparamagnetic particles embedded in soft polymer gels behave like elastic filaments.[101]

Chemical cross-linking of functionalized particles under an external magnetic field allows for greater control of the elastic properties of the chains. Conjugation between functional groups on the particle surface and small molecules yields rigid chains. For example, amine groups on neighboring particles will covalently bond with glutaraldehyde.[102] More flexible chains are generated with thiol-coated beads that react with bis PEG-maleimide,[103] or streptavidin-coated particles that form strong noncovalent bonds with bis PEG-biotin or bis DNA-biotin.[23,104]

Upon removal of the external magnetic field, the chains undergo thermal fluctuations. The magnitude of the shape fluctuations are governed by the chain's bending rigidity, EI. Note that for macroscopic materials, the bending rigidity is the product of the Young's modulus, E, and the moment of inertia, I. From polymer physics, the persistence length ($l_p = EI/k_BT$) defines the ratio of bending energy to thermal energy. Rigid chains are characterized by large EI, whereby their contour length is much shorter than their persistence length ($L << l_p$). Semiflexible chains have lower EI, where their contour length is of the same order of magnitude as l_p ($L \sim l_p$). Regardless of the chemistry used for linking, increasing the length of the linker decreases EI, making the chain more flexible.[23,103] The impact of linker length on flexibility can be seen in Fig. 12a. In the absence of an external magnetic field, chains connected with longer DNA linkers, *i.e.* 4k base pairs (bp), exhibit more pronounced shape fluctuations compared with shorter DNA, *i.e.* 2k base pairs. In contrast, when increasing field strengths are used during chain assembly, EI increases, resulting in stiffer chains. This increased stiffness is caused by the strong field bringing the particles into proximity, allowing for a larger cross-linking area. Figure 12b illustrates how the rigidity of the chain can be modified by changing the DNA linker length and the strength of the external magnetic field.

Experimentally, EI can be measured from thermal fluctuations, as demonstrated for actin filaments and microtubules.[105,106] A Fourier mode analysis of the dynamics in the chain shape due to thermal fluctuations provides EI.[107] Additionally, force methods such as optical tweezers[108] and orthogonal magnetic fields have been used to bend the chain and compute EI.[99,109]

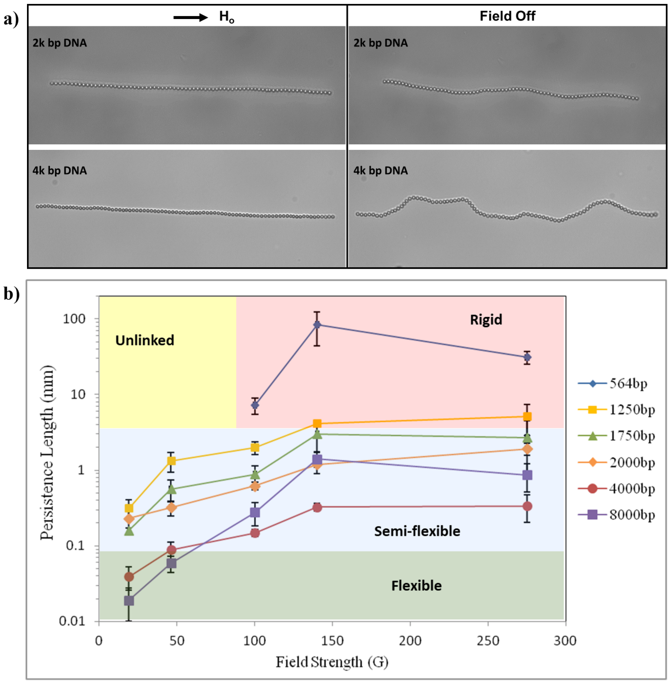

Fig. 12 a) Microscopy images of streptavidin-coated particles of $2a = 1$ μm connected by biotinylated DNA linkers of different length. Straight chains (left) are initially aligned in a static magnetic field of 60 Gauss. Upon removal of the field, the chains exhibit flexibility (right). When the magnetic field is removed, the chain linked by the longer 4k bp DNA (bottom) experiences more pronounced shape fluctuations compared to the chain linked by shorter 2k bp DNA (top). b) A plot illustrating how DNA linker length and magnetic field strength can be used to tune the rigidity of a chain from rigid to semiflexible and flexible. An unlinked region exists where stable chains cannot be generated. Adapted with permission from ref. 23. Copyright (2014) American Chemical Society.

4.2 Dynamics of cross-linked chains

4.2.1 Configurations in orthogonal static fields

Linked chains present more complex shapes and dynamics compared to unlinked chains. The tethers between particles introduce chain elasticity, which competes with magnetic and viscous forces. For example, chain buckling is observed under orthogonal magnetic fields, resulting in hairpin, S-shaped, and multifolded configurations.[110] If the dipolar interactions are strong enough to overcome the elastic energetic penalty, the chain buckles, such that the dipoles recover their preferred alignment to the greatest possible extent.[111]

The simplest buckled structure is the U-shaped hairpin, shown in Fig. 13a. For longer, more flexible chains, or strong magnetic fields, multiple buckling modes (arches) can develop along the chain length. The resultant number of bending modes, n_b, and their curvature depend on several parameters of the system, including EI, aspect ratio, and magnetization.[109,112] Consequently, the ratio of magnetic to elastic forces is described by the magnetoelastic number (Mn), which is commonly used to analyze chain buckling:

$$\mathrm{Mn} = \frac{\pi \mu_o \chi^2 H_0^2 a^4 N^2}{6EI\left(1-\frac{\chi}{6}\right)\left(1+\frac{\chi}{12}\right)} \tag{23}$$

High values of Mn represent more buckled structures.

Guidelines to generate higher-order buckled structures have been derived based on Mn. To generate n_b bending modes, Belovs & Cebers[113] and Roper *et al.*[109] determined that the minimum Mn scales with n_b^2, using slender-body theory for a magnetic filament. Figure 13b shows that a long semiflexible chain can develop more than 10 bending arches with pronounced amplitudes, whereas shorter chains acquire less bending modes (*e.g.* a hairpin) or simply rotate to reorient with the applied field. Buckling of magnetoelastic filaments in viscous fluids has been recently reviewed by Cebers & Erglis[114] with emphasis on the mathematical models and numerical simulations. Recently, Zhao *et al.*[22] presented higher-order buckling dynamics using experiments and numerical analysis. Their analysis demonstrates that upon buckling, the bending modes coarsen by growing in amplitude, while the original long-axis of the chain contracts, until a quasi-stable configuration is realized. Figure 13c and d demonstrate the growth and coarsening buckling dynamics in experiments and simulations, respectively. Furthermore, unlinked particle chains suspended in a viscoelastic medium have been reported to depict a similar buckling behavior when an orthogonal field is applied. Longer chains develop more arches for the same field conditions and additionally, follow the scaling between Mn and n_b^2. In such cases, the amplitude of the bending modes can be correlated to the elastic modulus of the suspending polymer gel.[101]

4.2.2 Cross-linked chain dynamics in circular time-varying fields

The buckling dynamics of magnetoelastic chains in static orthogonal fields are precursors for more complex phenomena displayed in time-varying fields. In contrast to unlinked chains, linked chains are unable to fragment. In addition to magnetization, field frequency, and chain length, EI plays a significant role on linked chain dynamics.[109,112] Therefore, rigid and semiflexible filaments behave very differently when actuated with the same field conditions. In these systems, both the Ma and Mn numbers are needed to describe and classify the dynamical states.

The linear chain model, introduced in Sec. 3.2, is useful to delineate the conditions that separate phase-locked (synchronous) rotation from more complex dynamics that arise because of the chain elasticity in a 2-D circular rotating magnetic field (Eq. 16). Below Ma_c (Eq. 22), a linked chain rotates at a steady phase lag, α, with the same angular frequency, ω, as the external field.[104] While a linked chain may also deform into S-shaped structures,[116] as was in the unlinked case, the linear chain model remains a good approximation.

When $\mathrm{Ma} > \mathrm{Ma}_c$, rigid chains exhibit an asynchronous back-

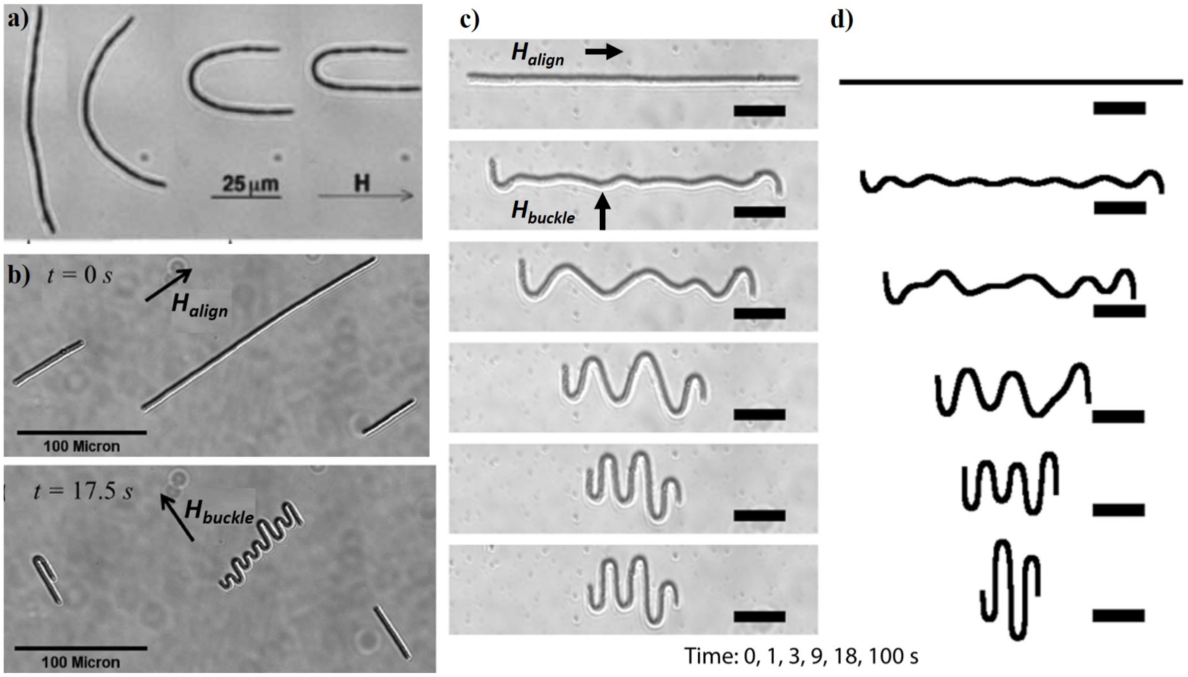

Fig. 13 Buckled configurations of linked superparamagnetic chains subjected to a static field. The field is initially used to align each chain, and then an orthogonal field is applied to buckle the chains. a) A chain linked by adsorbed polyacrylic acid bends into a hairpin configuration, which is the lowest bending mode. Reprinted figure with permission from ref. 99. Copyright (2003) by the American Physical Society. b) Long semiflexible chains buckle with up to 14 bending modes. Shorter chains display less or no bending modes, such as in the case of the hairpin structure and the reoriented chain, respectively. c) Experiments and d) simulations of buckling dynamics in long semiflexible chains show the development and coarsening of high-order bending modes. While the final number of arches differs between the experiment and simulation, both illustrate the same process of buckling initiation and evolution. Scale bars = 24 μm. Images b)-d) reprinted with permission from ref. 22. Copyright (2018) by the American Physical Society.

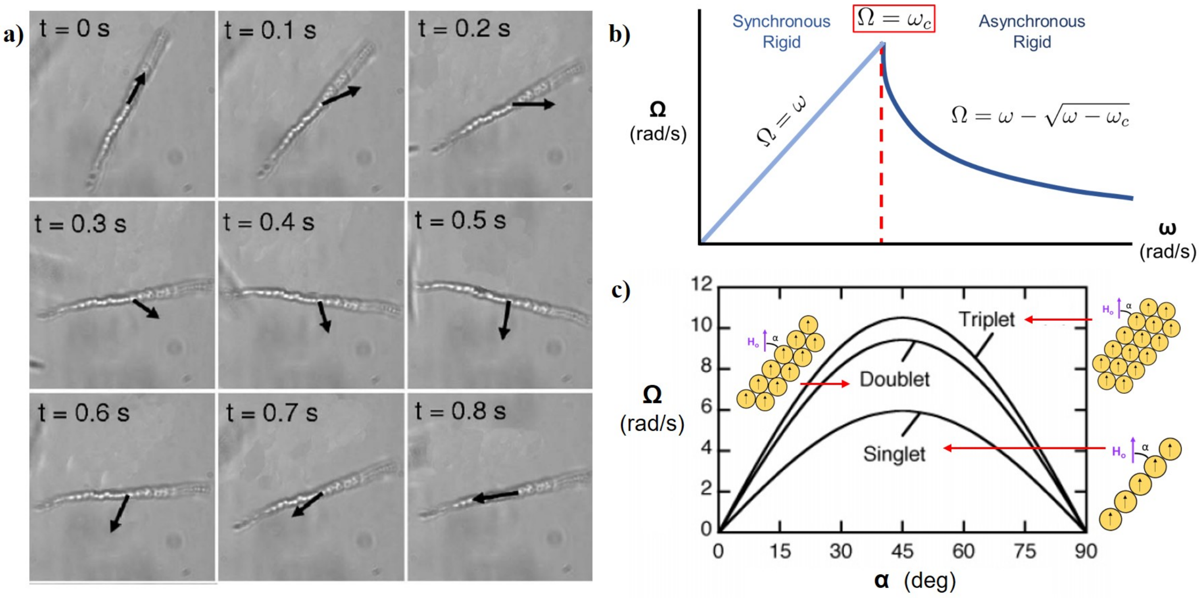

Fig. 14 Asynchronous rotation of rigid chains under a time-varying magnetic field. a) Time series images of asynchronous rotation of a linked chain. The black arrows indicate the instantaneous direction of the external field. At 0.5s, the field is orthogonal to the chain. After which, the chain reverses rotation until it realigns with the field. Reprinted figure with permission from ref. 104. Copyright (2004) by the American Physical Society. b) Plot of angular frequency of a linked chain (Ω) as a function of the angular frequency of the field (ω). Below the critical frequency (ω_c), the chain rotates with the same frequency as the field. Above ω_c, the rotation becomes asynchronous and Ω decreases with increasing ω. Adapted with permission from ref. 115. Copyright (2006) American Chemical Society. c) Ω as a function of the phase lag angle (α). A single chain is compared with doublet and triplet chain bundles that rotate asynchronously. Increasing the number of chains in a bundle increases Ω because of an increase in magnetization. Adapted with permission from ref. 93. Copyright (2005) American Chemical Society.

and-forth rigid-rod rotation, denoted as the phase-slipping regime,[93,104] shown in Fig. 14a. Initially, the rigid chain rotates with an increasing phase lag angle, α. At the critical angle $\alpha_c = \pi/4$, a chain experiences the maximum driving torque (Eq. 18). As α increases beyond α_c, the magnetic torque decreases, resulting in a decrease in the angular frequency of the chain. Once α surpasses α_{magic}, the radial interactions switch from attractive to repulsive, but the tethers prevent chain fragmentation. At $\alpha = \pi/2$ the chain temporarily halts and reverses its direction of rotation until it is able to realign with the external magnetic field. Once it realigns, the entire cycle restarts.

Even though the chain rocks back-and-forth, its net rotation follows the same direction as that of the field, but with a slower angular frequency.[93] The effective angular frequency of the chain (Ω) in the asynchronous regime follows:[115]

$$\Omega(\omega) = \omega - \sqrt{\omega^2 - \omega_c^2} \tag{24}$$

where ω is the field frequency and $\omega_c = \mu_o \chi^2 H_0^2 \ln(N/2)/16\eta N^2$ is the critical frequency necessary to undergo asynchronous motion (see the factor multiplying $\sin(2\alpha)$ in Eq. 20). Equation 24 is only valid for $\omega > \omega_c$ since ω_c is the frequency that produces the Ma_c that leads to asynchronous rotation (Eq. 22). For $\omega \leq \omega_c$, the chain rotates synchronously with an angular frequency $\Omega = \omega$. Figure 14b shows how Ω changes with ω. Experimentally, Ω can be determined by computing the discrete Fourier transform (DFT) of the vertical displacement of one of the terminal ends of the chain over time, and these results have very good agreement with the predictions from Eq. 24.[115] Additionally, as shown in Fig. 14c, chain bundles consisting of laterally linked doublet and triplet chains rotate asynchronously at a higher Ω compared to a single chain under the same Ma.[93] It is also worth noting that this asynchronous motion is observed at high Ma for other rigid dipolar systems, such as superparamagnetic ellipsoids,[117] irregularly shaped ferromagnetic colloids,[115] unlinked dimers of either diamagnetic or paramagnetic spherical particles,[42,118] and optically actuated nanorods.[119] Furthermore, chains with a high aspect ratio may buckle as they rotate because of an interplay between the rod elasticity and viscous drag forces, similar to buckling of chains in static fields.[104,120]

When considering semiflexible chains of particles, more complex dynamics are observed because of the development of elastic deformations during the phase-slipping regime. For example, particles linked with DNA form filaments that can achieve higher Mn values. For these chains, various dynamical regimes are characterized by wagging, coiling, and folding, as shown in Fig. 15a.[20] The wagging regime occurs at high Ma for chains of $N > 20$ particles. Wagging chains rotate while displaying a cyclical beating motion that is characterized by rapid bending into highly curved S-shapes, followed by immediate relaxation into straight configurations. Coiling consists of long filaments ($N \geq 35$) whose terminal ends initially bend, while the rest of the chain remains unresponsive to changes in α.[20,121] As the field rotates, the bent ends curl into ellipses that continue to coil towards the center. Once the chain sufficiently reduces its drag, it sustains synchronous rotation with the external field. This behavior is analogous to the folding pathway of longer unlinked chains collapsing into clusters, presented in Fig. 11b. However, for linked chains, the chain elasticity inhibits the transition into a cluster. Finally, chains of $N \geq 40$, buckle into pronounced S-shapes and rotate synchronously in a folded configuration. The folded structure arises from the lateral attractions between parallel segments of the chain that are out-of-registry.[104] This mechanism is the same that produces zippered bundles of chains, described in Sec. 3.1.3.[90,91] These dynamical regimes can be described by a state diagram of Ma versus N, as shown in Fig. 15b. Boundary lines that separate the various regimes can be derived by balancing magnetic, viscous, and elastic torques.

4.2.3 Cross-linked chain dynamics in precessing time-varying fields

The complexity of linked chain structures and dynamics can be expanded when actuated with precessing time-varying magnetic fields. These 3-D rotating magnetic fields can be generated by a combination of an in-plane rotating field (Eq. 16) and an orthogonal static field:

$$\mathbf{H}_0 = H_0 \begin{bmatrix} \sin\beta\cos(\omega t)\hat{\mathbf{e}}_x \\ \sin\beta\sin(\omega t)\hat{\mathbf{e}}_y \\ \cos\beta\,\hat{\mathbf{e}}_z \end{bmatrix} \tag{25}$$

where $H_0 = \sqrt{H_{xy}^2 + H_z^2}$, H_{xy} and H_z being the field strengths of the in-plane rotating field and the out-of-plane static field, respectively, and β the precessing angle between the resultant field and the precessing axis ($\beta = \tan^{-1}(H_{xy}/H_z)$). A schematic for this type of field is shown in Fig. 1.

Recent numerical simulations of chains in these precessing fields highlight the formation of hairpin and S-shaped configurations, whose tip-to-tip separation vector lies along the precessing axis.[122,123] Under certain conditions of β and Mn, the chains adopt more interesting configurations, such as a quasi-static helical arrangement that coils around the precessing axis.

To understand these configurations, consider the time-averaged pair dipolar interactions, based on the DM, in a high-frequency precessing field:

$$\langle U_{ij}(r_{ij}, \beta, \vartheta)\rangle = \frac{\mu_o m^2}{8\pi r_{ij}^3}(1 - 3\cos^2\beta)(3\cos^2\vartheta - 1) \tag{26}$$

where ϑ is the angle formed between the center-to-center separation, r_{ij}, and the precessing axis. The precessing magic angle, $\beta_{magic} = 54.7°$, delineates two different regimes of magnetic interaction that dictate the final structure of the chain. In the attractive regime ($0° < \beta < \beta_{magic}$), the magnetic interactions are minimized when $\vartheta \to 0$, favoring an overall orientation along the precessing axis. However, due to competition with elastic forces, the filament buckles, resulting in short, curved segments that lie perpendicular to the precessing axis. This configuration is shown in Fig. 16a. Increasing Mn leads to the bent regions becoming more localized, thus creating structures that have very long, straight segments aligned with the precessing axis, separated by very short, but highly curved arches. The repulsive regime ($\beta_{magic} < \beta < \pi/2$) presents greater structural complexity. In this case, minimization

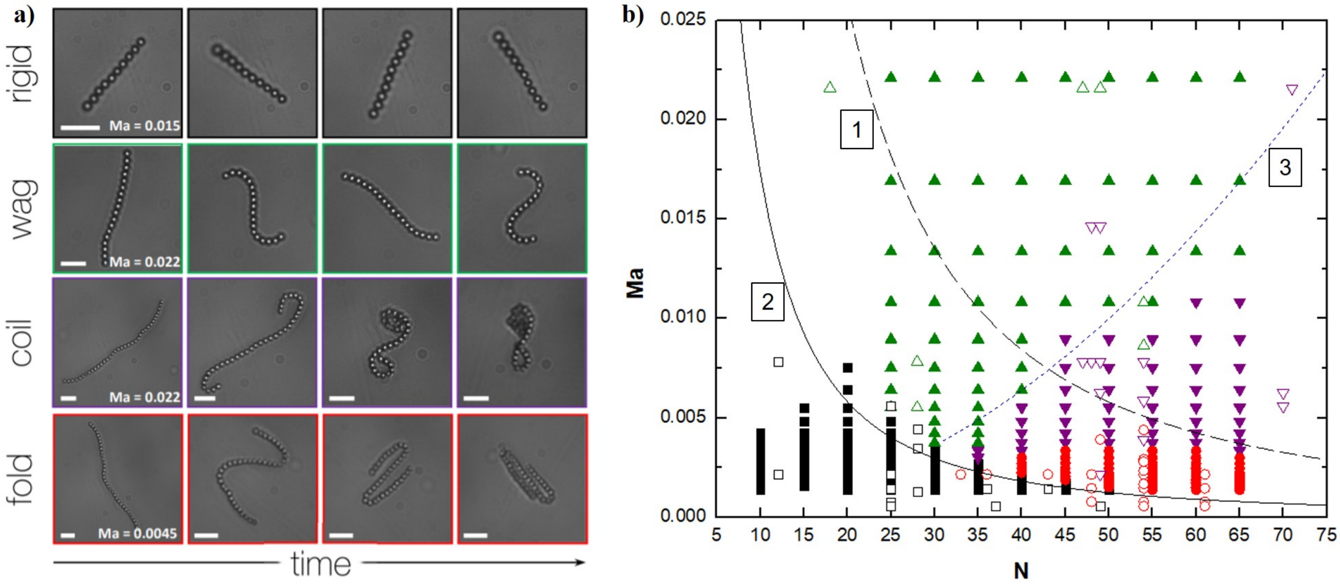

Fig. 15 DNA-linked superparamagnetic semiflexible chains undergo complex dynamics in circular time-varying magnetic fields. a) Snapshots of the different types of chain dynamics: rigid rotation, wagging, coiling, and folding. Rigid rotation corresponds to typical synchronous rotation with respect to the magnetic field. Wagging, coiling, and folding dynamics represent asynchronous motion observed in the chains. b) State diagram delineating each of the dynamical regimes according to the chain length (expressed as the number of particles N along the chain) and Ma. Boundary line 1 marks the Ma$_c$, from Eq. 22, that separates synchronous from asynchronous rotation, according to the linear chain model. Boundary line 2 marks the critical Ma that accounts for interparticle spacing along the chain. Boundary line 3 marks the Ma at which the Mn buckles the chain into higher-ordered bending modes. This boundary separates wagging from coiling and folding. The symbols in the state diagram correspond to the various regimes: rigid rotation (black squares), wagging (green triangles), coiling (purple inverted triangles), folding (red circles). Filled symbols represent simulations and unfilled symbols are experimental observations. Reprinted figures with permission from ref. 20. Copyright (2017) by the American Physical Society.

of the magnetic interactions occurs as $\vartheta \to \pi/2$, so that preferred alignment of the chains is perpendicular to the precessing axis. At very high Mn, in this repulsive regime, the chains can also adopt planar buckled structures, but the orientations reverse. Localized bending regions are aligned parallel to the precessing axis, while the long straight segments approach orthogonality with respect to the axis, as shown in Fig. 16b. In addition, at low to intermediate Mn, helices become the preferred configuration in this regime. This novel phenomenon emerges from the competition between elastic and magnetic forces in a helical segment.[122] Briefly, the magnetic forces seek to collapse the chain into a closed circular loop confined to the plane perpendicular to the precessing axis. However, this loop comes at the expense of a large bending energy. To balance this energy cost, the elastic energy attempts to minimize the curvature by straightening the chain along the axis to minimize the curvature by distributing it throughout the length of the chain. The balance between both contributions dictates the final pitch of the quasi-static helix.

Experimental realization of this helical configuration in precessing fields has been recently reported.[28] As depicted in Fig. 16c, a chain initially curls at its terminal ends, similar to circular fields, and then coils and rotates with respect to the precessing axis. The rotation and coiling generates bending waves that propagate toward the center, leading to contraction of the chain length along the precessing axis and radial expansion in the rotating plane. This phenomenon produces the helical shape that changes dynamically as it rotates; however, the helix maintains a constant pitch to circumference ratio. Additionally, the helix displays self-propulsion because of its proximity to the substrate and elastic heterogeneity along the chain. Simulations show that the helices form for $\beta > \beta_{magic}$,[123] but experimental demonstration occurs in a much narrower window of β above β_{magic}. When $\beta >> \beta_{magic}$, the chains coiled and collapsed into the rotating plane since the rotational component of the magnetic field was stronger than the static component. In contrast, for $\beta \leq \beta_{magic}$, the chains remained in a mostly linear configuration aligned with the static component of the magnetic field. Thus, none of the hairpin configurations predicted by simulations were observed in these experiments. Furthermore, the initial configuration prior to application of the precessing field can lead to even more complex dynamics, as shown in Fig. 16d and e. Depending on the initially folded configuration (hairpin or S-shape), the chain can transition into different types of twisted and knot-like morphologies that continually evolve as a result of rotation and bending wave propagation.

Colloidal assemblies that reversibly coil into helices or knot-like structures via external actuation provide an opportunity to generate microscale propulsive systems. Nature often employs chirality of helical filaments to sustain motion at low Reynolds number (Re), such as in the case of prokaryotic flagella.[124,125] In fact, soft ferromagnetic helices have been manufactured through sequential steps of photolithography, metal deposition, and etching;[126,127] and have proved to be efficient artificial swimmers during magnetic actuation. However, inducing a helical shape

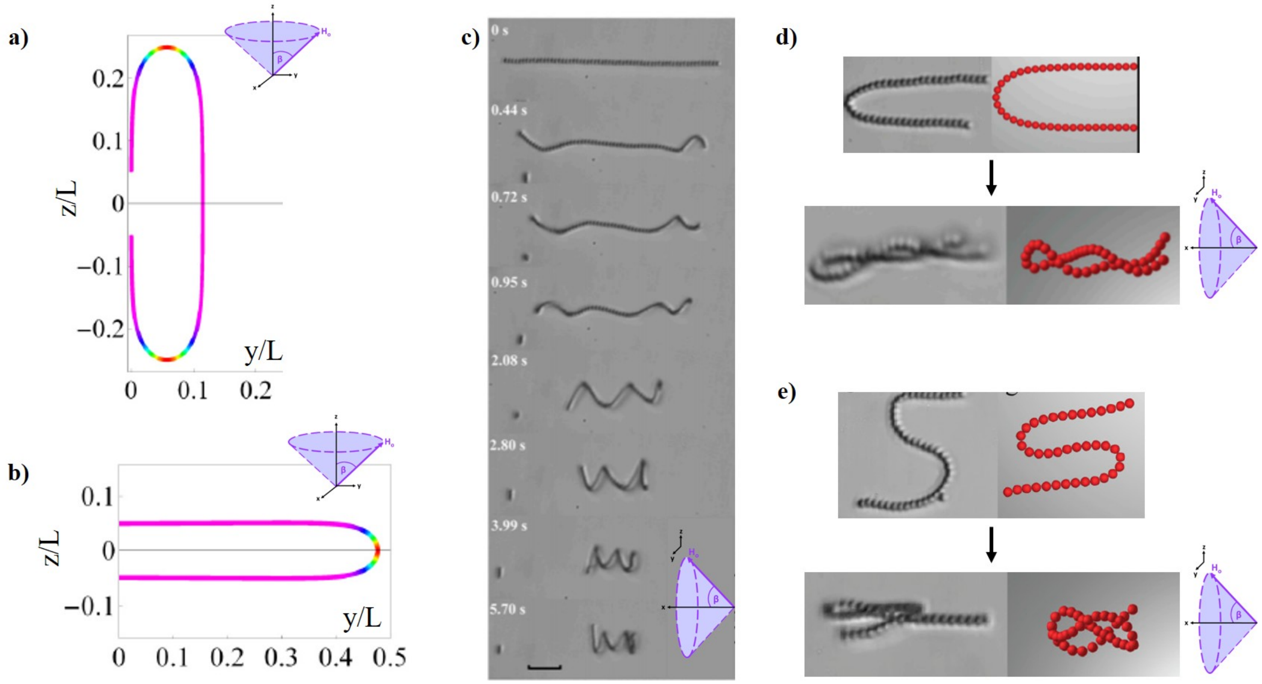

Fig. 16 Static and dynamic chain structures under precessing time-varying fields. a) For $\beta \leq \beta_{magic}$, chains turn into hairpin structures with localized segments of curvature perpendicular to the precessing axis. b) For $\beta > \beta_{magic}$, chains turn into hairpin structures with localized segments of curvature perpendicular to the precessing axis. This shape is one of the possible configurations for $\beta > \beta_{magic}$. Images in a) and b) reprinted with permission from ref. 123. Copyright (2017) by the American Physical Society. c) For β slightly above β_{magic}, the chain coils into a dynamic helix. d) A hairpin and e) an S-shaped chain acquire different knotted shapes in a precessing field. Images in c)-e) adapted from ref. 28 with permission from PNAS. The insets indicate the orientation of the precessing field for each case.

in a simple colloidal chain provides an alternative, tunable, and cheaper method to produce artificial filaments for transport applications. Further applications that utilize the dynamics of these chains are detailed in the subsequent section.

4.3 Applications of 1-D chains

A chains' ability to interact hydrodynamically with the suspending fluid and magnetically with applied fields make these systems of great interest for flow control in microfluidic devices. Both linked and unlinked chains have been designed as pumps, valves, mixers, and microswimmers in time-varying magnetic fields. In general, cross-linked chains display more complex dynamics, and consequently, can be used in a broader range of applications compared to unlinked chains.

One of the first applications demonstrated for linked chains was micromixing. Biswal & Gast[128] experimentally showed that linked chains in rotating fields could be used to enhance the effective mixing between fluids in a microfluidic channel, as shown in Fig. 17a. Within the creeping flow regime, the rotating chains lead to a cyclical stretching and folding of the fluid's lamella, analogous to kneading dough. Kang *et al.*[35] demonstrated a similar phenomenon with unlinked chains. Here, the periodic dynamics of chain breakup into smaller daughter chains, followed by their recombination, lead to a highly efficient mechanism of chaotic mixing, as shown in Fig. 17b.

Linked and unlinked rotating chains have also been used to transport cargo. The asymmetric hydrodynamic interactions of the chains near substrates lead to their translation, as observed in Fig. 18a i. This tunable motion generates a net flow in the system, transporting suspended cargo with a high degree of control. Figure 18a ii presents the experimental realization conducted by Sing *et al.*,[97] where a carpet of rotating unlinked chains transport a vesicle through a microfluidic device. More recently, Yang *et al.*[100] presented a new methodology to capture and transport cargo, based on the coiling dynamics of linked chains in rotating fields. Due to the reversibility of the coiling mechanism, this technique permits active loading and unloading of the cargo. Moreover, the translating mechanism of the system, which relies on the

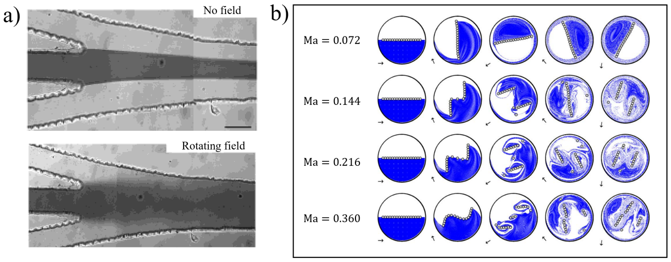

Fig. 17 Chains of superparamagnetic particles acting as micromixers. a) A three-lane channel geometry filled with a suspension of linked chains shows enhanced mixing of dye when a rotating magnetic field is applied. Adapted with permission from ref. 128. Copyright (2004) American Chemical Society. b) Numerical simulations of unlinked rotating chains mixing two fluids, blue and white, at different Mason numbers. Adapted figure with permission from Ref. 35. Copyright (2007) by the American Physical Society.

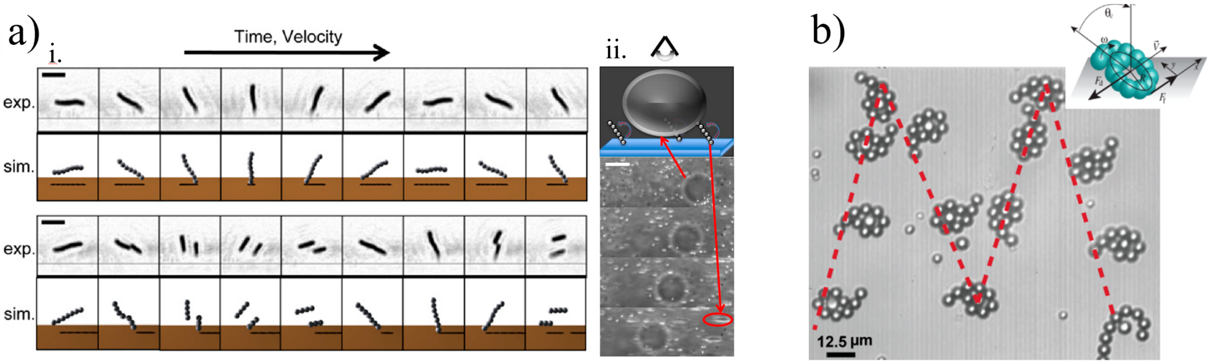

Fig. 18 a) Representation of rotating chain dynamics near a substrate (i.) and experimental realization of vesicle transport due to the flow generated by this mechanism (ii.). Scale bar = 20μm. Adapted from ref. 97 with permission from PNAS. b) Experimental realization of cargo transport using coiling dynamics of linked chains in rotating magnetic fields. Reprinted with permission from ref. 100. Copyright (2017) American Chemical Society.

inclination of the coiled system with an interacting wall, is proven to be precise, as demonstrated by the predetermined M-like path in Fig. 18b.

The design of linked and unlinked chain propulsion systems has led to the development of microswimmers and micropumps. Swimming dynamics at the microscale depend on breaking spatial symmetry. Dreyfus *et al.*[129] designed a microswimmer composed of a linked magnetic chain that had one end attached to a red blood cell. The chain was actuated with an oscillating (transverse) magnetic field, where a static and sinusoidal magnetic field were combined to generate a cyclical wave that propagated from the free end to the cargo, breaking spatial symmetry, as shown in Figs. 19a and 19b iii. Due to its similar motion, this linked chain has been referred to as an artificial flagellum. An alternative method to break spatial symmetry is to utilize elastic defects along the chain backbone,[109,114] as presented in Fig. 19b i. In another scheme, a hairpin chain translates by effectively forming two flagella with propagating bending waves, as shown in Fig. 19b ii. Roper *et al.*[112] provides an extensive analysis of the self-propulsion dynamics of magnetic filaments due to the application of time-varying fields. The magnitude and angular frequency of the applied magnetic field dictates the ratio between viscous to bending forces, also known as the dimensionless sperm number.[130]

Magnetic chains have also been implemented as artificial ciliated surfaces to generate flow. Vilfan *et al.*[131] reported unlinked chains attached to a substrate via nickel anchoring sites, shown in Fig. 20a. A tilted precessing magnetic field is applied to rotate the chain in a conical motion. The precessing angle, β, and the tilt angle dictate the resulting hydrodynamic flow. A zero tilt angle represents a standard precessing field. In general, larger tilted precessing angles generate faster fluid velocities near the rotating chains. Additionally, a higher field frequency and smaller distance between tethered chains influence the dynamics between the chains.[132] Babataheri *et al.*[133] showed that linked chains can induce fluid flow when actuated with an oscillating magnetic field that varies with time. As illustrated in Fig. 20b, these linked chains capture the beating cilia motion more effectively, but the observed pumping efficiency is low.

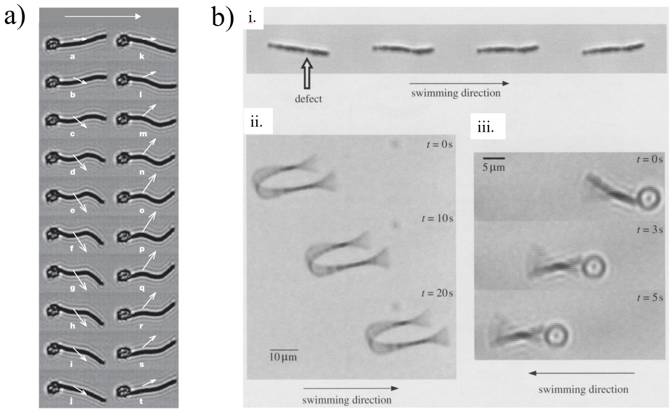

Fig. 19 Linked magnetic chains as artificial flagellated swimmers in a combined static and sinusoidal magnetic field. a) Snapshots (from a to t) of the swimming dynamics of a linked chain with a red blood cell attached to one of its ends. The direction and magnitude of the magnetic field is represented by the length of the white arrows. The arrow at the top of the image represents the direction of the swimmer. Reprinted by permission from Springer Nature Customer Service Centre GmbH: Nature, ref. 129, Copyright (2005). b) Images of three types of swimming patterns: i. Spatial symmetry breaking due to elastic defects, as highlighted by the white arrow; ii. Chain with an imposed hairpin shape forms effectively two flagella; and iii. Chain with attached cargo to one end. Image republished with permission of The Royal Society (U.K.), from ref. 112, Copyright (2008); permission conveyed through Copyright Clearance Center, Inc.

5 2-D Networks of Superparamagnetic Colloids

The interplay between different colloidal interactions, *e.g.* magnetic, electric, or hydrodynamic, can also be controlled to form large-scale 2-D network systems. These structures are more complex and interconnected than the 1-D magnetic chains previously discussed. Oftentimes, 1-D magnetic chains are the precursors to network structures. Moreover, these networks enable the design of tunable materials with hierarchical organization and multilevel functionality. Furthermore, investigations with these colloidal assemblies have led to new insights into the principles behind networks used in biological organization.[134,135] The assembly dynamics of these colloidal networks will be first explained with

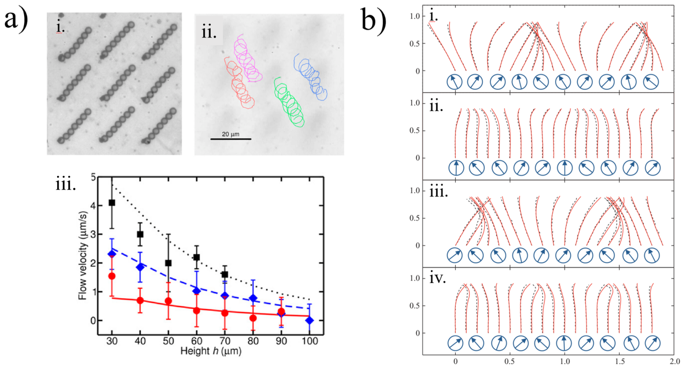

Fig. 20 Cilia-like motion of paramagnetic chains. a) Unlinked chains anchored to a substrate via nickel sites are placed in a tilted precessing magnetic field. Tracer particles illustrate the fluid motion created by the rotating chains. The fluid velocity generated by the chains is shown as a function of the height from the wall, obtained by numerical simulations (lines) and experiments (symbols), for different tilt angles: 20° (red), 30° (blue) and 40° (black). Reprinted from ref. 131 with permission from PNAS. b) Images illustrating the motion of a linked chain driven by a constant oscillating field (i. and ii.) and a time-varying oscillating field (iii. and iv.). The dashed lines show experimental results and solid lines are for numerical predictions. The arrows represent the orientation of the instantaneous magnetic field. Adapted from ref. 133, Copyright (2011), with permission from Cambridge University Press.

static fields. Next, the influence of particle heterogeneity, *e.g.* magnetization, size, and dipolar interactions, on network formation will be described. Finally, networks formed in time-varying fields will be presented.

5.1 Networks assembled by lateral chain aggregation

Lateral interactions between chains have led to interconnected, network-like structures in static fields. As described in Sec. 3.1.3, the lateral aggregation of chains is a result of short-range dipolar interactions, which are diffusion-limited. Because of this short-range attraction, network formation is mainly observed in highly concentrated superparamagnetic suspensions, *i.e.*, where the particle fraction, ϕ, is greater than 0.5.[136] In such concentrated systems, column-like structures are formed in the direction of the field and become interconnected because of lateral chain aggregation. The existence of these segments requires some chains to bend away from the field direction, resulting in an elastic-like potential energy that is a function of the chains' curvature and the applied magnetic field. This energy is reflected in the magnetorheological response of the system, a property widely explored in the design of tunable damping materials.[137–139]

Fermigier & Gast[136] reported the first entangled network-like structures with superparamagnetic colloidal particles in static field. They showed that the chains would bundle into fibers with a thickness that could be tuned by varying the applied field strength and surface particle packing fraction, ϕ. Interesting behavior was observed, analogous to condensed matter. For example, when the magnetic coupling parameter, λ, was decreased, the networks released individual particles into the dilute phase, thus thinning the fibers. A state diagram, shown in Fig. 21, details the various structures formed.[70,136]

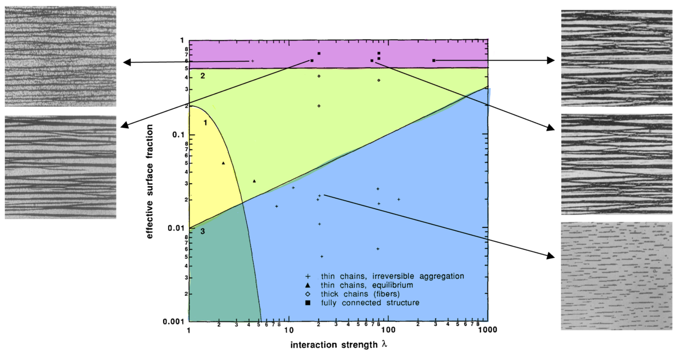

Fig. 21 Superparamagnetic colloids assemble into fiber and network-like structures in static magnetic fields as a function of ϕ and λ. Each colored section of the state diagram represents a different formed structure. Network-like structures are shown in purple at $\phi \geq 0.5$ for all λ. The other colored regions reference the various chain and fiber structures that form at either equilibrium or nonequilibrium conditions. Adapted from ref. 136, Copyright (1992), with permission from Elsevier.

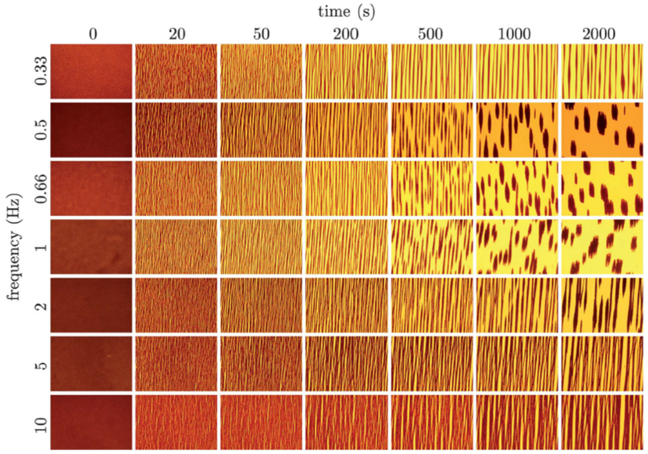

Fig. 22 Microscopy images of a 2-D system of superparamagnetic particles subjected to a static magnetic field pulsed at varying frequencies. Networks are initially formed, but then reorganize to form more ordered structures at intermediate frequencies. Reproduced from ref. 27 with permission from the Royal Society of Chemistry.

The networks formed with static magnetic fields are determined by the kinetics of particle aggregation, resulting in metastable, kinetically arrested states. Because structural reproducibility and control are difficult to achieve, several researchers have utilized toggled magnetic fields to generate more stable structures. For example, a square wave, which is generated by pulsing the field on and off at a given frequency, results in network structures that rearrange into condensed ellipsoidal aggregates aligned with the magnetic field direction.[141] Swan *et al.*[27] studied network breakup and crystallization as a function of pulse frequency and time, as shown in Fig. 22. The authors found that the pulse-off time governed the relaxation and resulting structure. There is a characteristic time associated with the distance a particle may diffuse away during the pulse-off state. Figure 23 illustrates the various reorganization pathways that are possible when this characteristic time is compared with the pulse-off time, t_{off}.[46] For short pulses (high-frequency), t_{off} is insufficient for

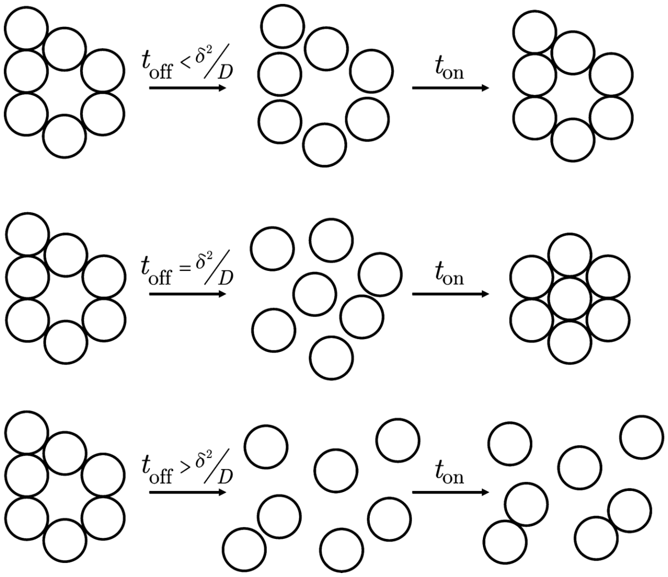

Fig. 23 A schematic representation of the structural rearrangements that occur under toggled fields. The particles diffuse as hard spheres for the time the field is off, t_{off}. Here, δ represents the interaction range and D is the diffusivity. The pulse-off time governs the extent of structural rearrangement. Reprinted with permission from ref. 140. Copyright (2016) American Chemical Society.

structural relaxation to occur. For long pulses (low-frequency), t_{off} allows the system to relax, whereby it retains no memory of its previous structure. There exists, however, a t_{off} that allows for just enough relaxation, such that more ordered structures are formed. Additional variables, such as the duty cycle of the field, have been recently used to provide more precise control over the structure.[142]

5.2 Networks assembled by anisotropic interactions

Networks in static magnetic fields can also be accomplished by introducing more than one type of interaction through heterogeneity, *i.e.* different particle types, multiple induced dipoles, particle size distribution, or surface functionalization. Such heterogeneity can cause chaining in more than one direction, thereby creating an interconnected network. Byrom *et al.*[15] created interconnected structures by using particles with varying magnetic susceptibilities. Fractal-like aggregates were generated by assembling superparamagnetic and diamagnetic particles in a ferrofluid with a static magnetic field. Both parallel and perpendicular attractive interactions were achieved, as shown by Fig. 24a. The relative strength of these interactions can be tuned by varying ferrofluid susceptibility, and thus the fractal dimension is controllable.

Additionally, multiple interactions can be induced to a homogeneous particle suspension through the use of electric and magnetic fields. Static electric fields can induce dipoles within dielectric particles. When such particles are also magnetic, multiple induced dipoles can be used to generate network structures. Bharti *et al.*[26] demonstrated this phenomenon by applying orthogonal electric and magnetic fields to a suspension of superparamagnetic particles. The perpendicular fields caused bidirectional chains to form that evolved into networks, as shown in Fig. 24b. The structures formed were shown to be dependent on the ratio of the applied fields, *e.g.* when the applied magnetic field was stronger than the electric field, more dominant chaining occurred in the direction of the magnetic field.

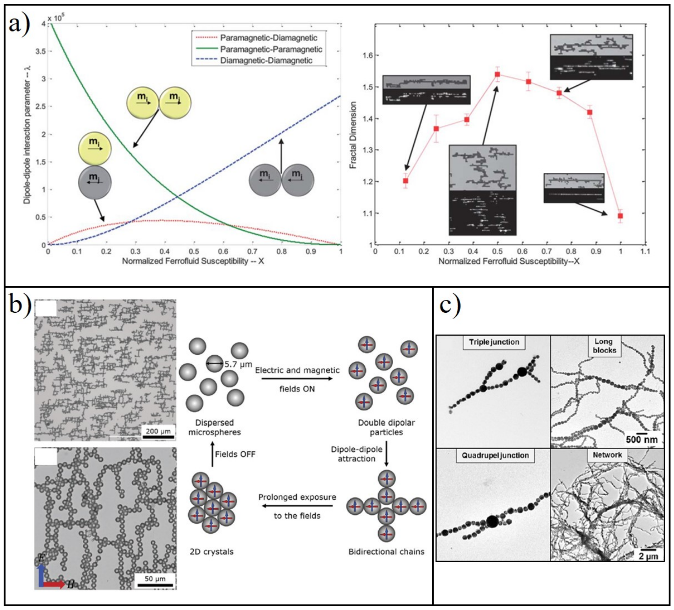

Fig. 24 a) Particle-particle interactions in a mixed suspension of superparamagnetic and diamagnetic colloids in a ferrofluid can be attractive in both the parallel and perpendicular direction of the applied magnetic field. Left: Interactions as a function of normalized ferrofluid susceptibility. Right: The fractal dimension of the aggregate as a function of normalized ferrofluid susceptibility. Reproduced from ref. 15 with permission from the Royal Society of Chemistry. b) Microscopy images of networks formed by superparamagnetic particles in perpendicular magnetic and electric fields (left), and a schematic of their induced dipoles and subsequent formations (right). Reproduced from ref. 26 with permission from the Royal Society of Chemistry. c) Different types of junctions and branching found through size polydispersity in paramagnetic colloids. Reprinted with permission from ref. 143. Copyright (2015) American Chemical Society.

As mentioned previously, varying particle sizes can also be used to create networks in static fields. Bannwarth *et al.*[143] formed network-like structures using size polydispersity with superparamagnetic colloids. Figure 24c showcases the different types of junctions and networks they produced by controlling the ratio of particle sizes. Large particles were shown to be capable of interacting with multiple smaller particles, leading to multijunction features. The aggregates were formed under flow and were thermally sintered, resulting in complex network structures. Recent work by Al Harraq *et al.*[144] combined polydisperse particle sizes with inhomogeneous surface functionalization to generate more types of branching in concentrated systems.

5.3 Networks assembled in precessing time-varying fields

The previously described network structures were assembled under unidirectional static and pulsed fields. Greater complexity in networks can be achieved by utilizing a triaxial magnetic field.

These precessing fields (Fig. 1) vary in direction over time. A suspension of monodisperse superparamagnetic particles can form large-scale networks under an applied high-frequency precessing field rotating at the magic angle ($\beta_{magic} \approx 54.7°$).[134] Networks formed under these precessing fields are structurally different from those assembled under unidirectional fields. These networks have a structure analogous to wet foams, characterized by void spaces that are separated by colloidal lamella.[145] These network assemblies were first theoretically demonstrated by Martin *et al.*[146,147] with ferromagnetic colloids, and later, experimentally by Osterman *et al.*[16] with superparamagnetic colloids. The origin of these novel architectures is a combination of isotropic and anisotropic magnetic interactions arising in the magic precessing field. Therefore, it is important to revisit the dipolar interparticle interactions to understand these froth-like networks.

A dimer in a precessing magnetic field experiences negligible dipolar interactions at β_{magic}, as previously shown by the DM in Eq. 26. However, this model neglects the mutual dipolar effect between particles, which becomes important for concentrated suspensions. Therefore, the MDM can be used to determine the interaction potential, which can then be time-averaged over a single period of rotation to yield:[148]

$$\langle U_{ij}(r_{ij},\beta)\rangle = \frac{\mu_o\chi^2V^2H_0^2}{4\pi r_{ij}^3\left(1+\frac{\chi V}{4\pi r_{ij}^3}\right)}\left(1+\frac{3(\cos(2\beta)-1)}{4\left[1-2\frac{\chi V}{4\pi r_{ij}^3}\right]}\right) \qquad (27)$$

where $V = 4\pi a^3/3$ is the particle volume. As shown by Fig. 25a, the interaction between particles is repulsive at low β, with a long-range potential energy that scales as $1/r_{ij}^3$. At intermediate precessing angles ($\beta_1 \leq \beta < \beta_{magic}$), the particles experience short-range attraction and long-range repulsion (SALR) potential, where β_1 can vary between 44° and 52° depending on the product of χV found in Eq. 27. At $\beta \geq \beta_{magic}$, the interactions are only attractive[149] and decay as $1/r_{ij}^3$ (long-range) when the precessing angle is above β_{magic}. Interestingly, when $\beta = \beta_{magic}$, the DM predicts the interactions will vanish, but under the MDM, residual attractive interactions are still exhibited, as shown by the magenta curve in the inset of Fig. 25a. The spatial decay at this angle approaches $1/r_{ij}^6$, where the scaling can be obtained by fitting a radial power law to the plot of U_{ij} at $\beta = \beta_{magic}$ as a function of r_{ij} (computed using Eq. 27).[150] Alternatively, by assuming that $r_{ij}^3 >> V$, Eq. 27 can be approximated to $U_{ij} \sim -\mu_o\chi^3V^3H_0^2/\pi^2 r_{ij}^6$ at the magic angle.[151] This scaling corresponds to an isotropic (orientation-independent) short-range attraction, similar to the conventional van der Waals (vdW) attractions.[146]

However, these isotropic interactions are not sufficient to explain the formation of foam-like networks. To provide further insight into these assemblies, many-body interactions in colloidal trimers are considered. Trimers can form either linear structures or close-packed equilateral triangles in precessing magnetic fields, as shown in Fig. 25b for various precessing angles. The interaction potential is compared for a linear chain versus a close-packed isosceles triangle.[24,150,151] The resultant three-body magnetic interactions depend on the bond angle,[146,149] with the bond angles 0° and 120° corresponding to the chain and triangle, respectively. The three-body interactions are not merely the pairwise sum of the two-body interactions for a three-body system.[24,148] Instead, the full solution is obtained by solving a linear system of MDM equations for the magnetization of three particles (Eq. 5).[46] The complete MDM curve shows that at β_{magic}, the chain is more stable than the triangle, thus the linear structure is preferred. Therefore, the many-body interactions are anisotropic. These interactions are also short-range at β_{magic}, with the same scaling as the pair potential ($1/r_{ij}^6$),[151] which prevents further aggregation.

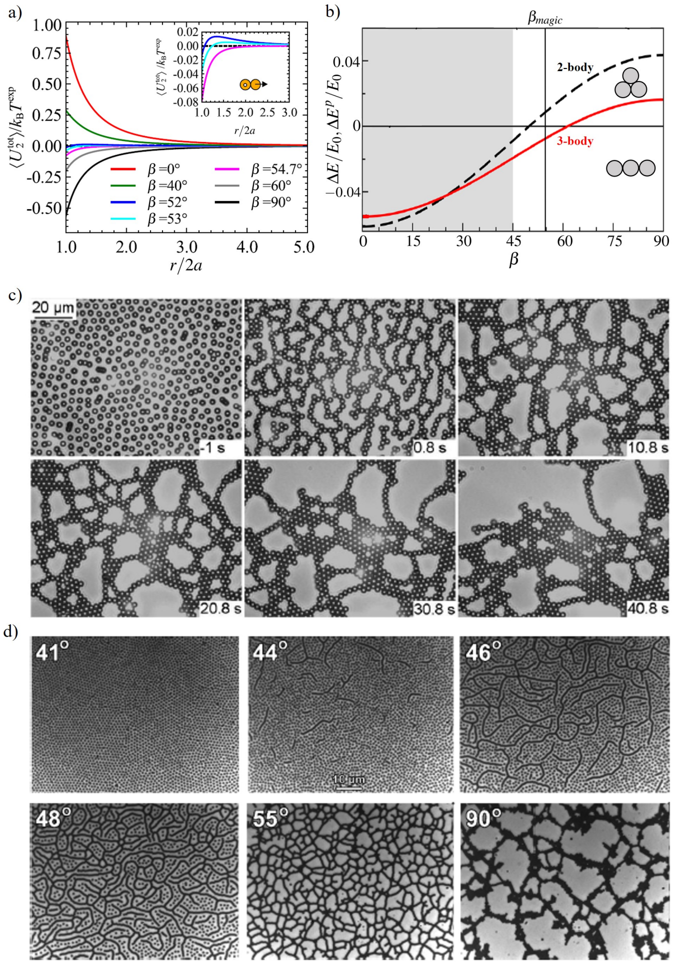

Fig. 25 Assembly of superparamagnetic colloids into network structures. a) The pair dipolar interactions calculated from MDM at various precessing angles. The magenta line in the inset shows that at β_{magic}, there are only short-range attractive interactions between particle pairs. Reprinted figure with permission from ref. 148. Copyright (2017) by the American Physical Society. b) Comparison of the many-body interactions for a trimer, calculated from a pairwise sum (2-body, black dashed line) versus the MDM system of equations (3-body, red). The energy for a chain and triangle is calculated, and the difference is plotted as the y-axis. The grey and white sections separate the repulsive and attractive interactions, respectively. Adapted with permission from ref. 24. Copyright (2014) American Chemical Society. c) Network coarsening under a precessing field at β_{magic}, via Ostwald ripening of the voids. Reproduced from ref. 152 with permission from the Royal Society of Chemistry. d) Quasi-steady-state images of 1 μm superparamagnetic particles in precessing fields with varying angles. Reprinted with permission from ref. 24. Copyright (2014) American Chemical Society.

Based on the previous analysis, two-body isotropic and many-body anisotropic interactions are important in precessing fields when forming network structures. The isotropic nature of the short-range vdW-like pair potential is necessary to initiate the assembly of colloidal networks in a precessing field at the magic angle. The magnetic potential in Eq. 27[146,147] induces the formation of randomly oriented dimers throughout the sample, where the lack of a prescribed direction confirms the isotropic features of the potential.[151] In concentrated suspensions, these dimers seed chains due to many-body anisotropic interactions that grow by head-to-tail aggregation and retain a random distribution.[16,151] The networks are then formed as these chains begin to intersect with each other, as shown in Fig. 25c. The network illustrates coarsening dynamics reminiscent of Ostwald ripening, in which voids shrink and grow, based on a critical size.[16,152] Subcritical (small) voids shrink as the surrounding chains coalesce into cluster patches with a close-packed arrangement. In contrast, supercritical voids increase in size in order to preserve the total volume of the system. This volume preservation results in network chains that support these larger void structures. Maier & Fischer[152] found that the critical void size remains constant throughout the coarsening dynamics of the network. This critical void size represents a characteristic length-scale for the network. Over the time-scale of their study, the network coarsened continuously over time without attaining a quasi-equilibrium state.

The role of β on the percolating structure was also evaluated by Müller *et al.*[24] Figure 25d shows the quasi-steady-state morphologies as a function of the precessing angle (β). When the precessing angle is well below β_{magic}, only repulsive interactions exist, and no structure is observed at $\beta = 41^\circ$. As the precessing angle approaches β_{magic}, the increase in attractive interactions results in chains that are phase separated from individual particles. This SALR potential is illustrated by the networks shown at $\beta = 44^\circ$, $\beta = 46^\circ$, and $\beta = 48^\circ$. At β_{magic} and beyond, all particles become part of an interconnected mesh-like network due to attractive interactions, shown by $\beta = 55^\circ$ and $\beta = 90^\circ$.

These networks have potential applications for the development of new materials that can enhance microscale transport processes. For instance, these networks can act as self-healing membranes, as observed by the immediate recovery of the original structure after its deformation.[16,134,153] This fast, self-healing property is inherent of the various dipolar interactions that aim to minimize the total magnetic energy throughout network assembly and coarsening. The network can also be utilized as an active system that propels nonmagnetic particles.[17] Pumping capabilities are conferred by creating an out-of-plane field rotation, through the application of an additional out-of-plane, time-varying magnetic field component. In this case, cooperative rotation of the chains and patches that constitute the network produces a conveyor belt effect that pumps the fluid above the network.[154] Interesting phenomena, such as ballistic motion above the colloidal lamella and diffusive motion on the voids, were observed.[17] Therefore, a combination of active and passive transport regions can be constructed with these foam-like architectures.

6 2-D Clusters of Superparamagnetic Colloids

Two-dimensional magnetic particle clusters are the next step in hierarchical colloidal assembly. In comparison to networks, magnetic clusters do not have a preferred orientation. The microstructure of these clusters ranges from a well-ordered colloidal crystal to a disordered colloidal droplet. Clusters have been used as experimental thermodynamic models because of this ability to mimic molecular phase transitions. They have also been applied for microfluidic control and microscale delivery.

In this section, the interactions governing assembly in 2-D and the different techniques employed to create and manipulate colloidal crystals with magnetic fields are first described. Briefly, commonly used order parameters for microstructure identification are also introduced. Next, the different phases and their transitions are presented, focusing on the thermodynamics and kinetics that govern them. Then, the bulk and interfacial rheological properties of the clusters are discussed. Lastly, applications of these magnetic clusters are highlighted.

6.1 Cluster assembly

As previously described in Sec. 3, unlinked particle chains rotate synchronously at low frequencies and breakup at higher frequencies in time-varying magnetic fields. Further increasing the frequency results in cluster formation because the magnetic dipole is effectively time-averaged over each particle. To understand this phenomenon, consider a rotating dimer, whose interaction potential is described by the mutual dipolar model (MDM) in polar coordinates:[42]

$$U_{ij}\left(r_{ij},\alpha\right) = \frac{m^2}{4\pi\mu_0 r_{ij}^3}\frac{1}{\left(1-\frac{2\chi a^3}{3r_{ij}^3}\right)^2}\left[1-3\cos^2\alpha+\left[\left(\frac{1-\frac{2\chi a^3}{3r_{ij}^3}}{1+\frac{a^3\chi}{3r_{ij}^3}}\right)^2-1\right]\sin^2\alpha\right] \quad (28)$$

The phase lag angle, α, is a result of the balance between magnetic and viscous forces. Above a critical frequency, a dimer no longer rotates and α-dependent terms in Eq. 28 can be time-averaged to a constant value. Du *et al.*[42] found this time-averaged value to be ~ 0.5, which collapses the interaction pair potential to an angle-independent form:

$$U_{ij}\left(r_{ij}\right) = -\frac{Cm^2}{8\pi\mu_0 r_{ij}^3} \quad (29)$$

where C is a constant defined as:

$$C = \frac{1}{\left(1-\frac{2\chi a^3}{3r_{ij}^3}\right)^2}\left[2-\left(\frac{1-\frac{2\chi a^3}{3r_{ij}^3}}{1+\frac{a^3\chi}{3r_{ij}^3}}\right)^2\right] \quad (30)$$

Thus, a high-frequency in-plane rotating magnetic field (HFRMF) above a critical frequency produces an isotropic attrac-

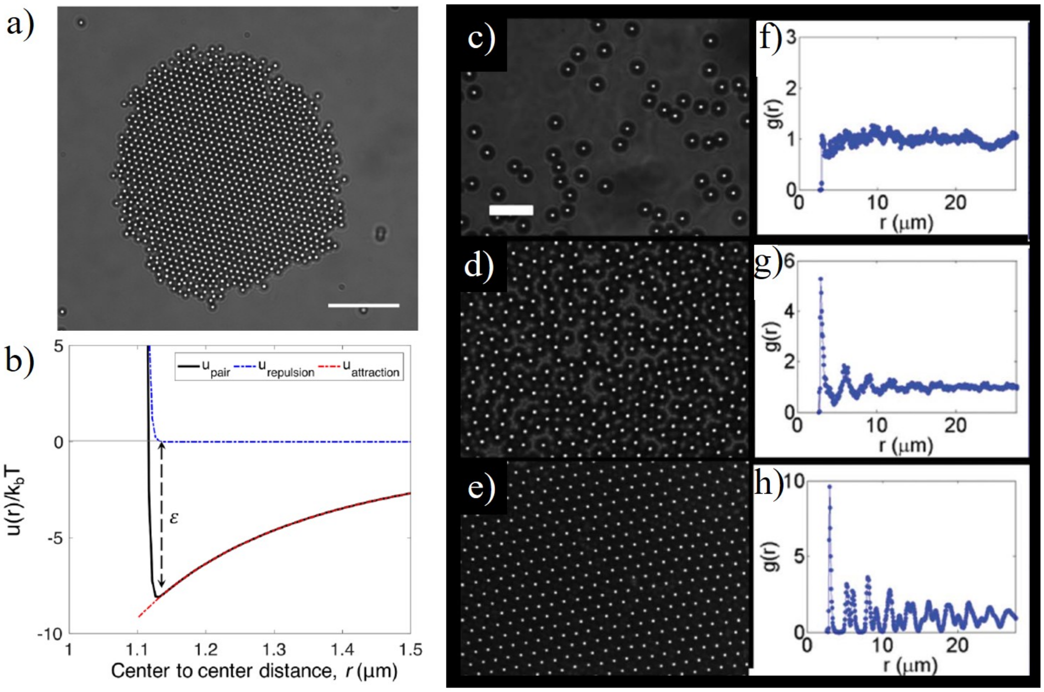

Fig. 26 Superparamagnetic particle assembly in a HFRMF. a) Microscopy image of a colloidal cluster formed with 1 μm particles. Scale bar = 10 μm. b) Interaction pair potential for a dimer in a HFRMF is composed of a long-range attraction (dotted red) and short-range repulsion (dotted blue). The well-depth (ε) can be tuned by the strength of the external magnetic field. Images a) and b) reprinted with permission from ref. 7. Copyright (2018) by the American Physical Society. c)-e) Microscopy images with increasing field strength and particle concentration. Scale bar = 5 μm. f)-h) The corresponding pair-distribution function for the microscopy images in c)-e), which further displays the increase in order with increasing field strength. Adapted from ref. 42 with permission from the Royal Society of Chemistry.

tive interaction that is dependent on the interparticle distance, r_{ij}. Note that a 2-D HFRMF can also be achieved using a precessing field at $\beta = 90°$. This isotropic interaction in the plane of assembly leads to 2-D clustering, as shown in Fig. 26a. Such nondirectional interactions are often compared to intermolecular forces. As a result of these interactions, cluster assemblies have configurations and dynamics that mirror those observed in molecular systems.

Additionally, the particles oftentimes have surface charges that lead to electrostatic repulsion, which can be accounted for using the Derjaguin-Landau-Verwey-Overbeek (DLVO) theory.[155] Combining both attractive and repulsive interactions, the interaction pair potential can be written as:

$$U_{ij}\left(r_{ij}\right) = -\frac{Cm^2}{8\pi\mu_0 r_{ij}^3} + \left(\frac{64\pi k_B T a \rho_\infty \gamma^2}{\kappa^2}\right) \exp -\kappa\left(r-2a\right) \qquad (31)$$

Here, the pair potential is plotted in Fig. 26b,[7] where the attractive (red) and repulsive (blue) components are summed to form the total interaction pair potential (black). In Eq. 31, ρ_∞ is the ion concentration in the bulk fluid, κ is the reciprocal of the Debye length, and γ is the reduced surface potential. The total pair potential in Fig. 26b is analogous to a Lennard-Jones (LJ) potential, with a long-range attraction and short-range repulsion. The well-depth (ε) and interparticle spacing can be tuned with either the magnetic field strength or the ion (salt) concentration. For example, at high field strengths and high salt concentration, the tightest particle packing within the cluster is achieved. The microscopy images shown in Fig. 26c-e display the transition between gas, fluid, and solid-like phases as the field strength is increased.

While cluster formation is achieved with long-range attractive interactions, long-range repulsive interactions have also been used to create and manipulate colloidal crystals (solid-like clusters), as compared in Fig. 27. In this case, an orthogonal external field is applied to a 2-D system of particles, resulting in a long-range repulsive dipolar interaction (Fig. 6a) that is isotropic. These repulsive interactions organize the particles into a colloidal crystal, albeit with larger interparticle spacings compared to crystals formed with attractive dipolar interactions. Researchers have used such crystals to study 2-D phase behavior by tuning the strength of the external magnetic field.[9,156] Zahn *et al.*[9] used this method to induce hexagonal order for particles trapped at an air-water interface and observed crystal melting through a hexatic phase, as theoretically described by Kosterlitz-Thouless-Halperin-Nelson-Young (KTHNY) theory for 2-D systems.[157–159]

6.1.1 Order parameters to characterize colloidal clusters

The structural organization within colloidal clusters is often characterized by different order parameters, briefly presented here. One of the most widely used order parameters for colloidal clus-

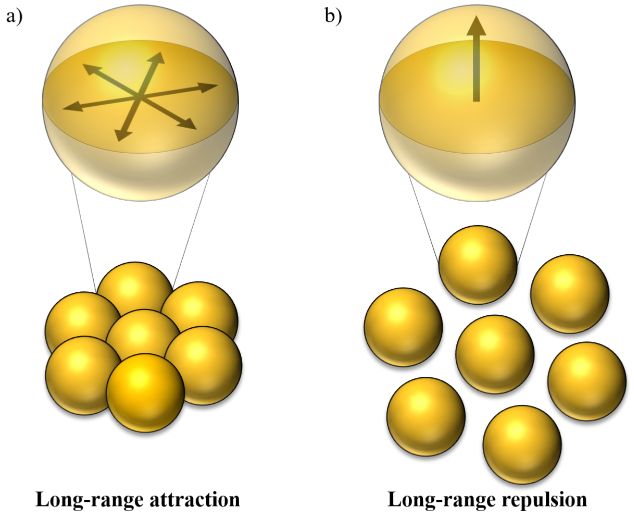

Fig. 27 A schematic of superparamagnetic particle assembly into a colloidal crystal via different interactions. a) A HFRMF induces a dipole that is averaged around each particle, resulting in an isotropic long-ranged attraction. b) An orthogonal magnetic field induces dipoles that are perpendicular to the plane of assembly, resulting in long-range repulsion. Note that long-range repulsion typically results in larger interparticle spacings.

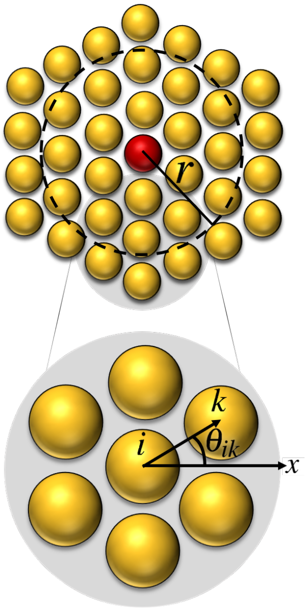

Fig. 28 A schematic of the variables utilized in $g(r)$ and ψ_6. The red colored particle represents a reference particle.

ters is the radial pair-distribution function ($g(r)$):

$$g(r) = \frac{A}{2\pi r N}\sum_{i}\sum_{i\neq j}\delta\left(r - r_{ij}\right) \tag{32}$$

where A is the area, N is the number of particles, and δ is the delta function. The radial pair-distribution function identifies order by calculating the probability of finding a particle at a distance, r, away from a reference particle, normalized by the probability of a uniform distribution. Gas-like clusters result in a constant $g(r)$, as shown in Fig. 26f for the corresponding microscopy image in Fig. 26c. Fluid-like clusters have regular peak spacing that decays with distance, characteristic of a lack of long-range order, as observed in Fig. 26g. Lastly, the $g(r)$ for colloidal crystals has well defined periodic peaks because of the ordered lattice spacing in the crystal, as shown in Fig. 26h.

In addition to radial distance, the angular orientation affects ordering within a cluster, which can be described by the local bond-orientational order parameter (ψ_6):

$$\psi_6 = \left\langle \frac{1}{N}\left|\sum_{i}\frac{1}{N_n(i)}\sum_{k(i)}\exp i6\theta_{ik}\right|\right\rangle \tag{33}$$

Here, N is the total number of particles in the area of interest, N_n is the number of nearest neighbors around particle i, determined through Delaunay triangulation, and θ_{ik} is the angle between the distance vector, connecting particle i and k, and the positive x-axis. Note that the $\langle\rangle$ brackets refer to a temporal average. Perfect crystalline order is represented by $\psi_6 = 1$, which is characterized by hexagonal packing with six nearest neighbors. The degree of cluster disorder is represented by a value of $\psi_6 < 1$, where zero is the lower limit.

Functions which depend on ψ_6 are also quite prevalent within colloidal cluster literature. The bond-orientational correlation function is one such function which contains a ψ_6 dependence:

$$g_6(r) = \langle \psi_6^*(0)\psi_6(r)\rangle \tag{34}$$

In this equation, ψ_6 is computed for a particle at some distance, r, away from a reference particle. Here, the reference particle value is denoted as $*$, and in this case, $\langle\rangle$ refers to a spatial average over all particles at distance r. The bond-orientational correlation function describes the decay of bond-orientational order as a function of distance. Note that the local orientation of a particle within a cluster can also be calculated as a function of ψ_6: $\theta_6 = \frac{1}{6}arg(\psi_6)$.

Another useful order parameter to characterize colloidal clusters is the structure factor, $S(k)$, typically determined from a Fast Fourier Transform (FFT) of a microscopy image of the cluster. For 2-D colloidal clusters, $S(k)$ can be calculated by:[148]

$$S(|\mathbf{k}|) = \frac{1}{N}\left[\left(\sum_{i}^{N}\cos\mathbf{k}\cdot\mathbf{x}_i\right)^2 + \left(\sum_{i}^{N}\sin\mathbf{k}\cdot\mathbf{x}_i\right)^2\right] \tag{35}$$

where $\mathbf{k}$ is the wave vector, $\mathbf{x}_i$ is the particle's position, and N is the number of particles in the image. The structure factor quantifies the intensity in an image by transforming spatial coordinates to the frequency domain. For a perfect hexagonal lattice, the structure factor displays distinct peaks representing the six-fold symmetry of the colloidal crystal. For less ordered clusters, the peaks are less distinct as the symmetry fades. This precursory description of order parameters serves as a basis to identify the different phases within colloidal clusters.

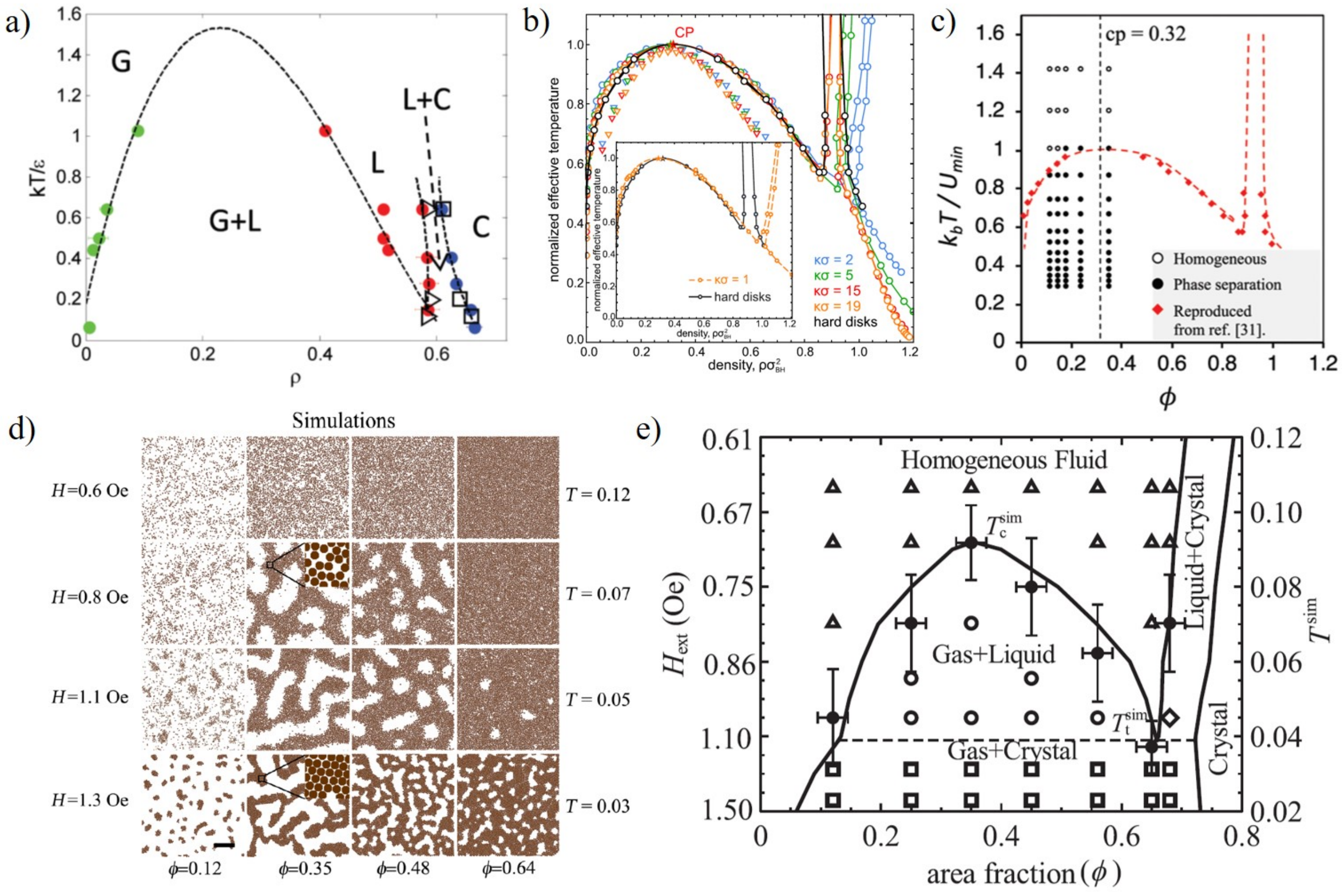

Fig. 29 Phase behavior of 2-D superparamagnetic clusters induced with a HFRMF. a) Phase diagram of the solid, liquid, and gas phase boundaries as a function of the normalized pair interaction potential and particle density. Reproduced from ref. 6 with permission from the Royal Society of Chemistry. b) Monte Carlo simulations of the phase diagram with varying Yukawa interactions. The inset showcases the phase boundaries normalized with the hard-sphere limit. Reprinted from ref. 160, with the permission of AIP Publishing. c) Data points (black) represent superparamagnetic particles in a high salt solution, which emulates the hard-sphere limit. The limited area fraction illustrates the practical limit that can be explored before colloidal multilayers form. Reproduced from ref. 25 with permission from the Royal Society of Chemistry. d) An illustration of the various phases, including liquid crystalline morphologies, and e) the resulting phase diagram as a function of effective temperature and particle area fraction. Reprinted figures with permission from ref. 148. Copyright (2017) by the American Physical Society.

6.2 Cluster phase behavior

Colloidal systems have been widely used to gain new insights into the dynamics of phase transitions.[161,162] As previously described, superparamagnetic clusters can transition from a disordered phase to a highly ordered crystalline phase by tuning the strength of the HFRMF. This behavior is reminiscent of phase transitions observed with molecular systems. For this reason, superparamagnetic clusters can be used as models for statistical thermodynamics. One advantage of these magnetic systems is that the interactions can be tuned *in situ*, allowing for nonequilibrium phase behavior to be probed.

6.2.1 Equilibrium cluster phase behavior

One characteristic of superparamagnetic colloids in a HFRMF is the ability of the colloids to undergo phase transitions by tuning the external magnetic field, as previously shown in Fig. 26. Experiments and simulations of these colloidal systems provide new insights into 2-D phase behavior. Du *et al.*[6] first investigated 2-D phase transitions of superparamagnetic colloids and generated a phase diagram, displayed in Fig. 29a. Using both experiments and simulations, the solid-liquid melting transition was described on this phase diagram as a function of a normalized minimum interaction potential and particle concentration. From Eq. 29, this pair potential is proportional to the square of the magnetic field. The phase diagram captures the liquid-gas binodal using a parabolic function through the critical temperature, which is in accordance with classical critical behavior.

Simulations of these systems use a canonical (NAT) ensemble, *i.e.* at constant number of particles, area, and temperature. The phase boundaries are obtained using thermodynamic integrations to calculate the free energies, which are then compared with particle densities.[163] Kryuchkov *et al.*[160] used Monte Carlo simulations to examine colloidal particles subjected to a long-range magnetic and short-range Yukawa interaction. They determined that the triple point and critical point can be tuned by adjusting the softness of the Yukawa repulsion, as shown by the phase diagram in Fig. 29b. Hilou *et al.*[25] experimentally showed that the hard-sphere limit of this phase diagram matched well for superparamagnetic particles suspended in a high salt brine, illustrated by Fig. 29c. The triple point is not experimentally realized due to the strong magnetic interactions, which form colloidal multilayers.

As previously discussed, Pham *et al.*[148] utilized precessing magnetic fields to assemble superparamagnetic colloids. At the precessing angle of 90°, liquid crystalline phases emerge, as displayed in Fig. 29d, in addition to the solid, liquid, and gas phases previously reported. Using a structure factor, $S(k)$, to characterize the phases, a phase diagram was constructed. Here, the interaction potential is presented as an effective dimensionless temperature, $T^* = (k_B T)/(V\mu_0 H_0^2)$, that is inversely proportional to the particle volume (V) and the square of the magnetic field strength, as shown in Fig. 29e. Recently, Li *et al.*[164] generalized the phase diagram to consider phase boundary alterations when the short and long-range attractive dipolar interactions are tuned.

Hilou *et al.*[7] examined the liquid-like properties of these clusters by defining the cluster interface as a function of the minimum pair potential, as shown in Fig. 30. The degree of order in the clusters is characterized using ψ_6.[7] At the lowest interaction potential, the cluster is completely disordered, analogous to a liquid droplet. For intermediate energies, a disordered interface surrounding a crystalline interior is observed. It is interesting to note that the interface is not a sharp transition, but occurs as a radial gradient of particle density. This gradient leads to a line tension, which is further discussed in Sec. 6.3. At the highest pair potential, the cluster becomes completely crystalline.

6.2.2 Nonequilibrium cluster phase behavior

The *in situ*, tunable interaction between colloids allows for exploration of nonequilibrium thermodynamics. Nonequilibrium dynamics provide routes to generating complex phases, which can be used to design new materials and functionalities. Pham *et al.*[148] showed how an initially homogeneous colloidal system undergoes coarsening in a HFRMF with time. The coarsening dynamics are governed by a power law, t^h, which is consistent with phase separation processes described by the Cahn-Hilliard equations.[165]

Hilou *et al.*[25] examined the dynamics of nucleation, coarsening, and phase inversion of these colloidal assemblies in HFRMF. Figure 31a illustrates the various states: clusters, voids, and a spinodal phase. Minkowski functionals, such as perimeter (p), characteristic length (L_s), and Euler characteristic (X), are used to identify the observed state as the colloidal system changes with time. The Euler characteristic is used to identify the more prevalent state. It is defined as the difference between the number of clusters and the number of voids. A positive X represents a phase dominated by clusters, and a zero X represents when the two states are present in equal quantities, characterizing the spinodal phase. The Euler characteristic quantifies the connectivity of the system and captures where phase inversion occurs. The characteristic length represents the average length-scale of the various states. Four distinct pathways are identified as a function of particle fraction, as shown in Fig. 31b. At high particle fractions, the system nucleates voids that coarsen with time. At intermediate particle fractions, phase inversion from voids to clusters can be observed, or a long-lasting metastable spinodal phase can form. At the lowest particle fractions, clusters nucleate and coarsen with time. From these pathways, the authors determined that L_s scales with H_0^2, $t^{0.4}$, and $\phi^{0.4}$. This direct control of the 2-D colloidal structure allows for the design of complex 2-D colloidal morphologies.

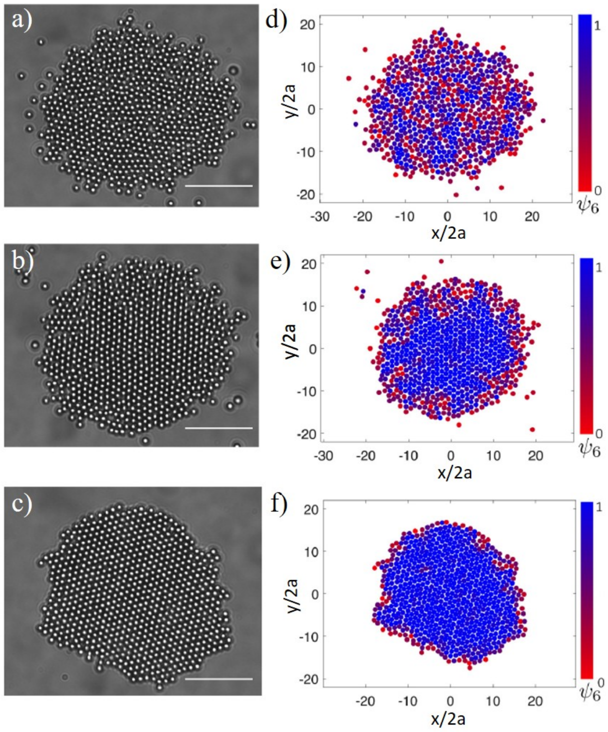

Fig. 30 Colloidal clusters under different magnetic field strengths. a)–c) Optical microscopy images of a colloidal cluster formed using a 20 Hz HFRMF of a) 8.5 Gauss, b) 9 Gauss, and c) 11 Gauss, corresponding to a pair potential with a minimum of 5.8, 6.6, and 9.8 $k_B T$, respectively. Scale bar = 10 μm d)–f) An overlaid colormap of ψ_6 for the corresponding microscopy images. Reprinted figures with permission from ref. 7. Copyright (2018) by the American Physical Society.

6.3 Rheological properties of clusters

The rheological properties of magnetically assembled clusters are of interest because of their unique dynamics. Since a change in interaction strength results in a change in phase, it follows that cluster rheological properties should also depend on the particles' interaction strength. Zahn *et al.*[10] found this dependence to be true for the bulk and shear elastic moduli in their colloidal crystals created at an air-water interface and organized with an orthogonal magnetic field. Both moduli were found to increase linearly with interaction strength, as shown in Fig. 32a. For clusters in HFRMFs, the interface resists deformation with increasing interaction strength, as demonstrated by Hilou *et al.*[7] This resistance is captured by the interfacial stiffness, which is the sum of line tension (2-D analog of surface tension) and its second derivative with respect to orientation, which accounts for interface curvature. Interfacial stiffness generally increases with increased interaction strength, as shown in Fig. 32b. Due to interfacial anisotropy,

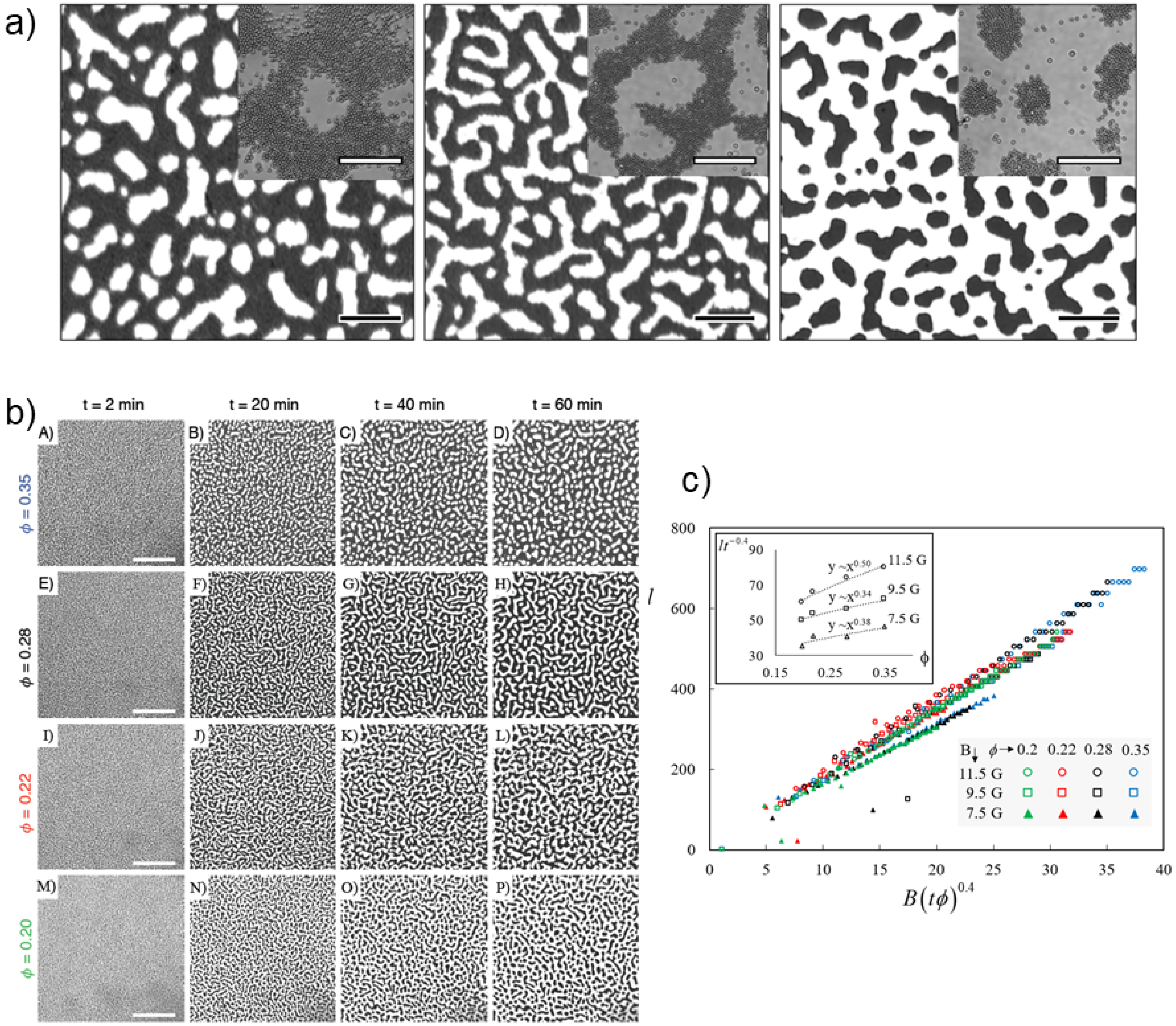

Fig. 31 Nonequilibrium thermodynamics with 2-D superparamagnetic colloids in a HFRMF. a) Microscopy images of various phases: void-rich (left), spinodal (center), and cluster-rich (right), that are observed for a given field strength and particle density. The dark regions represent particle-dense areas. Black scale bar = 300 μm. Insets provide zoomed-in images of the particle assemblies. White scale bar = 25 μm. b) Optical microscopy images of the time evolution of superparamagnetic particles undergoing phase separation at various particle fractions. Scale bar = 500 μm. c) The time evolution of the characteristic length-scale of the colloidal features can be scaled with particle fraction, ϕ, and the external magnetic field strength, H_0 (where $B = \mu H_0$ in the plot). Reproduced from ref. 25 with permission from the Royal Society of Chemistry.

larger variations in the interfacial stiffness values were measured at higher interaction strengths.

The cluster interface in HFRMFs also plays a role in cluster rotation. Although magnetic interactions are time-averaged in a HFRMF, small clusters rotate with a reduced frequency compared to that of the external magnetic field. In particular, Tierno *et al.*[8] used this rotation to estimate an effective magnetic cluster viscosity. They predicted a linear relationship between cluster rotation and field frequency, which matched their data well for field frequencies above ≈ 1kHz, as shown in Fig. 32c. The underlying reason for cluster rotation was attributed to magnetic relaxations within the cluster, generally. This counter-intuitive cluster rotation however, has since been further explored and described as a hydrodynamic effect from individual particles,[167] which some researchers have connected back to magnetic relaxations in the particles at very high field frequencies.[168]

While single particle dynamics is not the focus of this review, it is important to understand some basic properties of individual particles such that their collective effect on cluster rotation can be understood. In a HFRMF, a magnetic particle will rotate if it experiences a nonzero magnetic torque, often described by $\Gamma_m = \mu_0(\mathbf{m} \times \mathbf{H})$, where μ_0 is the permeability of free space, $\mathbf{m}$

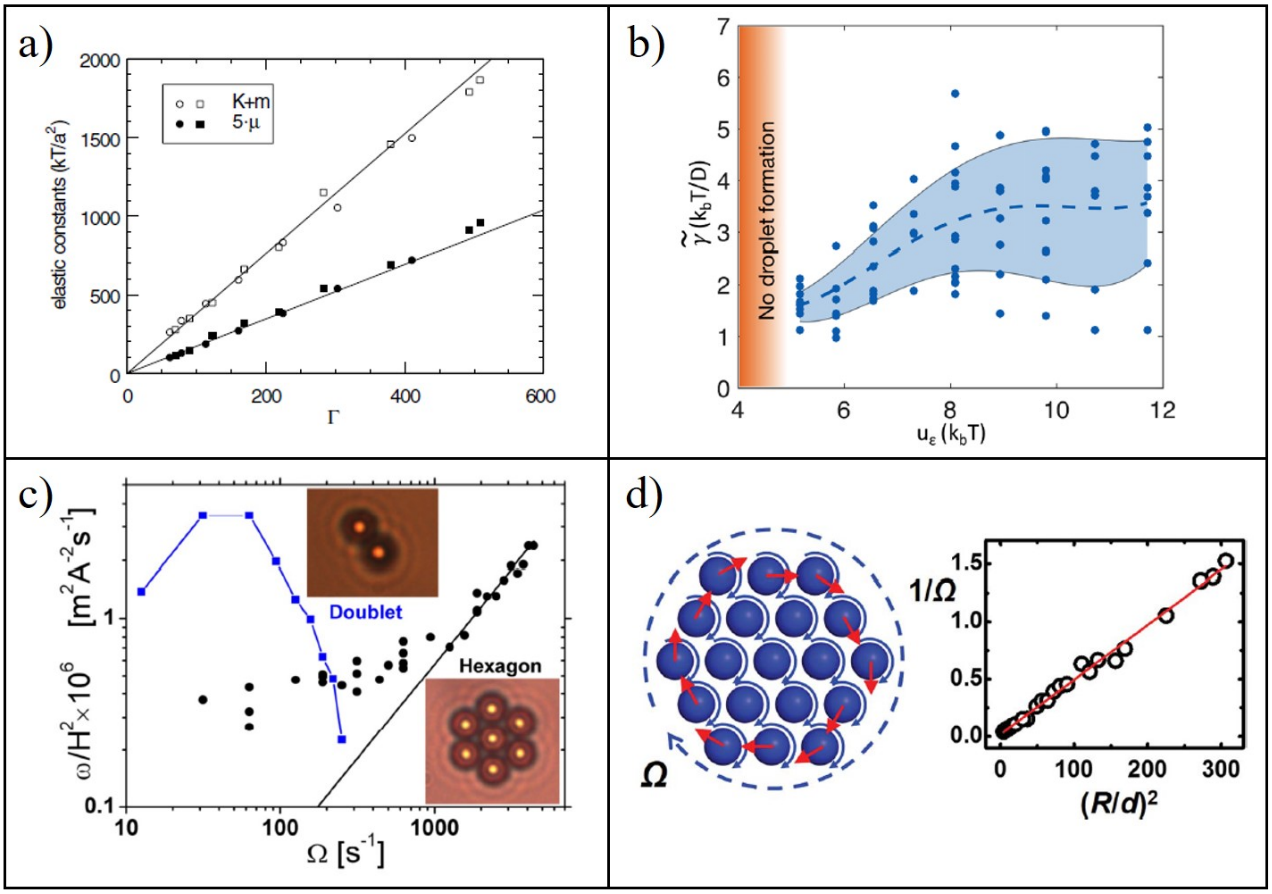

Fig. 32 Rheological properties of paramagnetic clusters. a) Linear trends of bulk (K) and shear (μ) elastic moduli of colloidal clusters increasing with particle pair interaction strength. Reprinted figure with permission from ref. 10. Copyright (2003) by the American Physical Society. b) Interfacial stiffness measurements of colloidal clusters, displaying an upward trend with increased interaction strength. The shaded blue area is the standard deviation of the data points. Adapted figure with permission from ref. 7. Copyright (2018) by the American Physical Society. c) Cluster rotation frequency, normalized with field strength squared, as a function of external field frequency. The insets of a hexagon and a doublet represent the type of structures that are graphed. The solid black line is a prediction for cluster rotation frequency, based on a viscoelastic analysis. Reprinted figure with permission from ref. 8. Copyright (2007) by the American Physical Society. d) [Left] Schematic of unbalanced interfacial shear induced rotation of a cluster. [Right] The inverse of cluster rotation frequency as a function of cluster size. Reproduced from ref. 166 with permission from the Royal Society of Chemistry.

is the dipole moment of the particle, and $\mathbf{H}$ is the total magnetic field. Assuming the dipole is centered within a spherical particle, the particle will only experience a nonzero torque if it's dipole moment is not aligned with the field. Note that any anisotropy of the particle in the plane of field rotation will also result in a nonzero torque, *i.e.* anisotropic shape and/or magnetic composition. Ferromagnetic particles have a permanent dipole. This permanent dipole requires ferromagnetic particles to physically rotate to align with the field direction, but due to viscous drag, their dipole lags behind the field with some constant phase lag angle, thereby creating magnetic torque that rotates the particle. Superparamagnetic particles are typically composed of smaller, magnetic grains randomly oriented within a matrix. As previously described in Sec. 2, in a HFRMF, superparamagnetic particles contain an induced dipole, and theoretically, the dipole is instantaneous, thereby resulting in zero torque. However, in reality superparamagnetic particles do experience a magnetic torque, which has been attributed to the existence of a small permanent dipole at low frequencies and a finite magnetic relaxation time at high field frequencies[168] or possibly a nonhomogeneous magnetic nanoparticle distribution within the larger matrix.[169]

The effect of magnetic particle rotation within a 2-D cluster was simulated by Jäger *et al.*[167] and showed the rotation and translation of individual particles was the cause of cluster rotation. When a particle rotates in a fluid, a flow field is created around the particle, and this flow can shear neighboring particles and alter local flow fields, resulting in particle translation.[170] This rotation-translation coupled motion results in a shear on each particle that was shown through experiments by Yan *et al.*[166] to be balanced within the cluster, but unbalanced at the interface, resulting in rotation. A schematic of this shear-induced rotation is found in Fig. 32d with the corresponding relationship Yan *et al.* found between cluster rotation and cluster size.[166] Collective particle rotation and resulting cluster rotation have both been used to extend magnetic colloidal cluster applications, highlighted below.

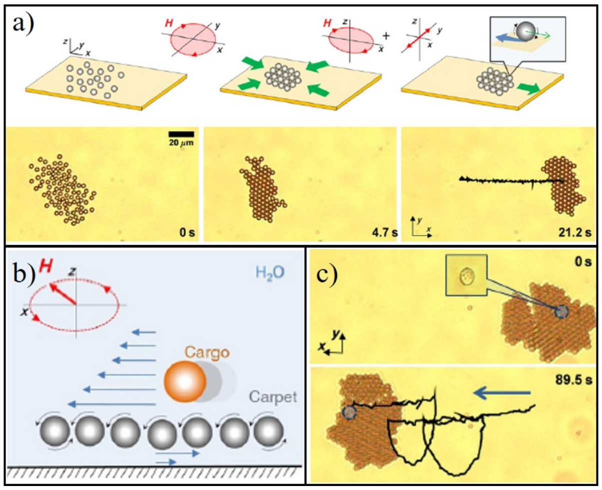

Fig. 33 Coupled magnetic and hydrodynamic fields lead to cluster translation. a) A schematic of the formation of colloidal carpets with a HFRMF and their mechanism for propulsion, with corresponding optical microscopy images below. b) A schematic of the flow fields above the carpet that help move the cargo. c) Microscopy images of the transportation of a yeast cell atop a colloidal carpet. The black line is the track of the yeast cell. Adapted figures with permission from ref. 171. Copyright (2015) by the American Physical Society.

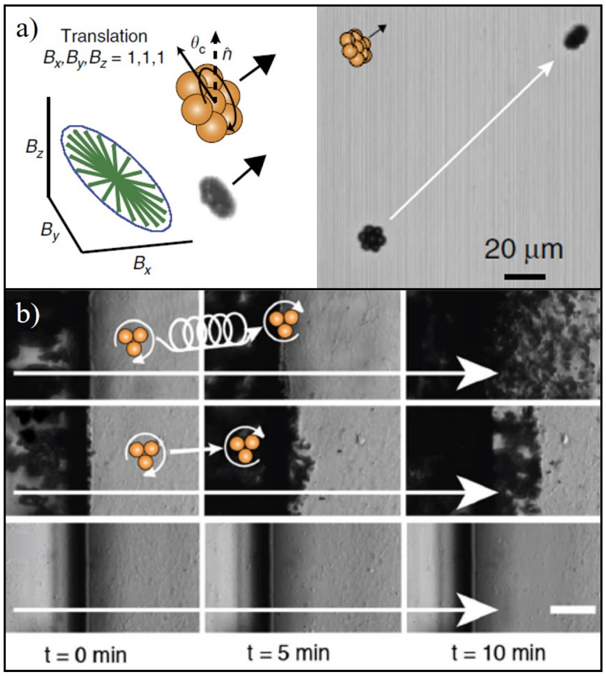

Fig. 34 Translation of colloidal microwheels. a) Schematic of tilted field and corresponding titled microwheel (left). Microscopy image of microwheel propulsion (right). Adapted from ref. 172 under terms of the Creative Commons CC BY 4.0 license. Copyright (2016), Springer Nature. b) Microscopy images, with time, that show the effect of microwheel propulsion on blood clot (grey) break up when functionalized with a chemical activator. Helical motion (top), direct motion (middle), and diffusion of the chemical activator alone (bottom). Scale bar = 40 μm. Adapted from ref. 173, Copyright (2017), with permission from John Wiley & Sons.

6.4 Application-related dynamics of clusters

Beyond the fundamental importance of using magnetic colloidal clusters as experimental models, physical applications for these 2-D assemblies have been explored, stemming from dynamics unique to magnetic clusters. In particular, biomedical applications have been at the forefront of promising applications, in part, because of the already established use of magnetic nanoparticles. Magnetic nanoparticles have found applications in targeted drug delivery and cancer therapies,[174] largely because of their ability to be directed with magnetic fields within the human body. Therefore, the directed motion of colloidal clusters via magnetic fields has been studied for the potential benefits they may hold in such applications.

As mentioned previously, HFRMFs induce individual particle rotation, resulting in local hydrodynamic effects. Martinez-Pedrero & Tierno[171] probed the directed motion of colloidal clusters near substrates. Colloidal carpets, as they were named, derived their motion from hydrodynamic coupling of particle rotation with a surface. Martinez-Pedrero and Tierno took advantage of this effect by using a perpendicular HFRMF to induce particle rotation normal to the surface, which induced translation of the entire cluster in 2-D, as seen in Fig. 33a. The cluster, originally formed with an in-plane HFRMF, was held together during translation via an oscillating in-plane magnetic field component. While in motion, the colloidal carpets were shown to pick up and transport cargo due to the same flow fields created by the rotating particles, but now above the carpet, as shown in Fig. 33b and c. Additionally, due to the strong dipolar attractions between particles within the crystal, the colloidal carpets were shown to self-heal when obstacles were encountered, and in a later work, this self-healing was shown to be tunable,[175] furthering their robust ability to be used as transport vehicles in biomedicine and microfluidic devices.

Tasci *et al.*[172] explored a similar rotation-coupled propulsion mechanism with smaller clusters. The authors lifted their clusters to the plane of field rotation, as shown in Fig. 34a, resulting in translation due to cluster rotation. The clusters were coined as microwheels because parallels could be drawn between their mechanism for motion and that of tires on a road. However, the microwheel rolling occurred for cluster orientations close to parallel with the surface, due to hydrodynamic slipping. Because the clusters could be oriented in any direction and that orientation relative to the chamber surface dictated the direction they were propelled, the authors created pre-programmed field orientations to produce unique patterns of motion. Helical motion, in particular, was used in a later work to showcase the efficiency of the magnetic microwheels to target and break up blood clots better than direct motion or diffusion,[173] as shown in Fig. 34b.

Lifting clusters up from the substrate has also been recently explored numerically with cross-linked clusters. Brisbois *et al.*[176] proposed magnetic clusters with elastic linkers that display unique deformation dynamics when exposed to a precessing field. Deformation dynamics similar to those of cross-linked chains were reported, such as buckling. While experimentally linking particles within a cluster has yet to be studied, such colloidal membranes would further the breadth of cluster dynamics, thereby influencing magnetic colloidal cluster applications.

7 Outlook

This review showcases the complexity in structure and dynamics of spherical superparamagnetic particles in time-varying magnetic fields. This complexity arises from the large variation in the induced dipolar interactions in both time and space. The emphasis in this review has been to illustrate the range of dynamics, from how spherical particles are assembled into hierarchical assemblies, to the resulting response of these structures in time-varying magnetic fields. Understanding how these spherical particle systems behave is important to analyze colloidal systems where additional complexities are introduced. New developments in the synthesis of anisotropic colloidal particles, the capability to couple magnetic fields with other fields, *i.e.* electric or flow, and the ability to probe collective behavior of multiple assemblies offer promise in creating hierarchically organized colloidal systems with novel properties and dynamics.

The use of anisotropic particles has increased the complexity of particle-particle interactions, and consequently, the formed assemblies. Anisotropic magnetic particles are characterized by their magnetization's directional dependence, which emerges from anisotropic particle shape or composition. The complexity of the assembled structures originates from a combination of the peculiarly shaped building blocks and the resulting nontrivial magnetic interactions. Recent reviews have presented the structures and applications of anisotropic magnetic colloids.[11,135,177] Common anisotropically shaped magnetic colloids include rods,[178] ellipsoids,[179–181] dumbbells,[12] and peanut-shaped particles.[182] Anisotropic composition of a particle can be achieved with an inhomogeneous distribution of magnetic material, either internally or externally.[58,183,184] For instance, Janus particles with a ferromagnetic coating on one hemisphere have been synthesized, resulting in a shifted dipole.[185,186] A number of experimental and simulation-based research has shown interesting assemblies when shifted dipoles are considered, with either in-plane or out-of-plane magnetic fields.[19,153,187–189] Janus particles will oftentimes assemble into staggered chains to maintain the head-to-tail dipolar alignment. These staggered structures can assemble into large-scale networks and planar clusters by tuning the dipolar shift.[190–192] Patchy magnetic colloids have also been synthesized to generate directional magnetic interactions.[193,194] The dynamics of these anisotropic colloids in time-varying magnetic fields are only starting to be explored.

Composites containing superparamagnetic particles have also been synthesized to generate magnetically actuated materials that have applications in soft robotics and artificial muscles. When embedded in a liquid crystal (LC), patchy paramagnetic microcubes exhibited complex folding dynamics to accommodate the strain exerted by the long-range orientational order of the LC.[195] Additive manufacturing methods have also been used to generate composite materials with anisotropic magnetization.[196,197] Superparamagnetic colloids embedded in polymer gels or photocurable resins create anisotropic composites that can be controlled with an external magnetic field.[198–201] For instance, linked polymeric squares containing aligned superparamagnetic chains act as microactuators that bend and fold in response to a magnetic field.[202] Ferromagnetic colloids embedded into a thermoplastic elastomer can reversibly curl into flower-like structures.[203] Actuation of these composites has been with static magnetic fields with on/off periods. Imparting time-varying magnetic fields on such composites may lead to new modes of actuation.

Novel fields have also led to new structures and dynamics. For example, simple paramagnetic colloidal swimmers were demonstrated using asymmetric time-varying fields.[204] An interesting phenomena observed was how Brownian motion increased the swimmer speed. The coupling of magnetic particles with other fields has also increased structure complexity. In an analogous manner to superparamagnetic colloidal assembly in magnetic fields, dielectric colloids in electric fields experience colloidal forces that are directly related to the dielectric permeability contrast between the colloids and their suspending liquid. Polymer-based superparamagnetic particles can be dielectric, such that when they are suspended in solvents, *e.g.* water or DMSO, the dielectric permeability contrast is large enough for their assembly to be manipulated with both magnetic and electric fields.[26,205,206] The interplay between multipolar interactions has led to percolating networks and condensed phase-like structures, whose spatial organization spans multiple dimensions. Magneto-acoustic assembly has also been utilized to apply a combined acoustic pressure, with varying magnetic fields, to generate ordered crystals.[207] Additionally, the combination of magnetic and acoustic fields allows clusters to transverse multiple dimensions.[208] In general, the structures covered in this review have focused on 2-D assemblies near substrates, but the application of complementary fields allows for the generation of 3-D assemblies or colloidal assemblies suspended in bulk solutions.

Incorporating hydrodynamic flow fields is another mode to induce hierarchical assembly. As previously described in Sec. 6, the translation of colloidal assemblies, generated by the individual motion of field-driven particles, can result in local flow fields.[97,171] These flow fields oftentimes lead to coupled motion, such as translating colloidal critters[209] or colloidal swarms.[210,211] Other emergent dynamics, such as magnetic colloidal vortices, have contributed to the field of active matter.[212–215] These flocks of particles exhibit organized patterns and synchronized motion. Combining experiments and simulations has led to a better understanding of the coupling of fluid flow and magnetic actuation of superparamagnetic colloidal assemblies. This coupling is of particular interest when considering complex geometries where confinement influences fluid flow,[216] or in large systems of chains and networks that interact cooperatively.[217] Moreover, superparamagnetic assemblies embedded in non-Newtonian fluids illustrate interesting dynamics. For example, magnetic structures in complex fluids have been used as microrheological probes[218,219] and have displayed swimming via reciprocal motion.[220,221] Lastly, fluid-fluid interfaces have also been used to direct new assemblies and study dynamics of magnetic colloids.[222] For instance, a superparamagnetic chain trapped at the air-water interface of an active fluid, comprised of motile *E. coli*, illustrates a competition between magnetic and fluid forces.[223] The dynamics of these assemblies in non-Newtonian and active fluids is an open area of interest.

With the advancement in the synthesis of more complex superparamagnetic colloidal building blocks, and the application of novel force fields, new dynamics and applications continue to be discovered. The advantage of superparamagnetic colloids is that their interactions can be directly tuned by the magnetic field. The majority of dipolar colloids have been assembled with forces well above k_BT, but as seen in Sec. 6, when dipolar interactions compete with Brownian motion, new phase transitions and structural dynamics are observed. These thermal effects raise questions about the role Brownian forces play in collective motion and/or the connectivity of networks. For example, how do thermal fluctuations alter the mechanical properties, such as elastic moduli and porosity, of the 2-D networks? In general, stochasticity governs the structure and resulting properties of cellular networks and polymer gels. Considering the hierarchical structures found in molecular and biological systems, superparamagnetic colloids span the time and length-scales needed to design and emulate the dynamics of these complex systems. The competition between dipolar interactions and other force fields will lead to new hierarchical structures that expand the dynamics and applications of these colloidal systems.

Conflicts of interest

There are no conflicts to declare.

Acknowledgements

This work was funded by the National Science Foundation under Grant No. CBET-17055703.

References

1 J. D. Jackson, *Classical Electrodynamics*, John Wiley & Sons, 1999.

2 R. E. Rosensweig, *Ferrohydrodynamics*, Courier Corporation, 2013.

3 A. Darras, E. Opsomer, N. Vandewalle and G. Lumay, *Scientific Reports*, 2017, **7**, 7778.

4 J. J. Benkoski, S. E. Bowles, R. L. Jones, J. F. Douglas, J. Pyun and A. Karim, *Journal of Polymer Science Part B: Polymer Physics*, 2008, **46**, 2267–2277.

5 S. Kralj and D. Makovec, *ACS Nano*, 2015, **9**, 9700–9707.

6 D. Du, M. Doxastakis, E. Hilou and S. Lisa Biswal, *Soft Matter*, 2017, **13**, 1548–1553.

7 E. Hilou, D. Du, S. Kuei and S. L. Biswal, *Physical Review Materials*, 2018, **2**, 025602.

8 P. Tierno, R. Muruganathan and T. M. Fischer, *Physical Review Letters*, 2007, **98**, 028301.

9 K. Zahn, R. Lenke and G. Maret, *Physical Review Letters*, 1999, **82**, 2721–2724.

10 K. Zahn, A. Wille, G. Maret, S. Sengupta and P. Nielaba, *Physical Review Letters*, 2003, **90**, 155506.

11 P. Tierno, *Phys. Chem. Chem. Phys.*, 2014, **16**, 23515–23528.

12 D. Zerrouki, J. Baudry, D. Pine, P. Chaikin and J. Bibette, *Nature*, 2008, **455**, 380–382.

13 S. Q. Choi, S. G. Jang, A. J. Pascall, M. D. Dimitriou, T. Kang, C. J. Hawker and T. M. Squires, *Advanced Materials*, 2011, **23**, 2348–2352.

14 P. Tierno, *Physical Review Letters*, 2016, **116**, 038303.

15 J. Byrom and S. L. Biswal, *Soft Matter*, 2013, **9**, 9167.

16 N. Osterman, I. Poberaj, J. Dobnikar, D. Frenkel, P. Ziherl and D. Babić, *Physical Review Letters*, 2009, **103**, 228301.

17 F. J. Maier and T. M. Fischer, *The Journal of Physical Chemistry B*, 2016, **120**, 10162–10165.

18 H. Kim and E. M. Furst, *Journal of Colloid and Interface Science*, 2020, **566**, 419–426.

19 S. K. Smoukov, S. Gangwal, M. Marquez and O. D. Velev, *Soft Matter*, 2009, **5**, 1285.

20 S. Kuei, B. Garza and S. L. Biswal, *Physical Review Fluids*, 2017, **2**, 104102.

21 Y. Gao, M. A. Hulsen, T. G. Kang and J. M. J. den Toonder, *Physical Review E*, 2012, **86**, 041503.

22 J. Zhao, D. Du and S. L. Biswal, *Physical Review E*, 2018, **98**, 012602.

23 J. Byrom, P. Han, M. Savory and S. L. Biswal, *Langmuir*, 2014, **30**, 9045–9052.

24 K. Müller, N. Osterman, D. Babič, C. N. Likos, J. Dobnikar and A. Nikoubashman, *Langmuir*, 2014, **30**, 5088–5096.

25 E. Hilou, K. Joshi and S. L. Biswal, *Soft Matter*, 2020, **16**, 8799–8805.

26 B. Bharti, F. Kogler, C. K. Hall, S. H. L. Klapp and O. D. Velev, *Soft Matter*, 2016, **12**, 7747–7758.

27 J. W. Swan, J. L. Bauer, Y. Liu and E. M. Furst, *Soft Matter*, 2014, **10**, 1102–1109.

28 T. Yang, B. Sprinkle, Y. Guo, J. Qian, D. Hua, A. Donev, D. W. M. Marr and N. Wu, *Proceedings of the National Academy of Sciences*, 2020, **117**, 18186–18193.

29 S. Melle, G. G. Fuller and M. A. Rubio, *Physical Review E*, 2000, **61**, 4111–4117.

30 S. Melle, O. G. Calderón, M. A. Rubio and G. G. Fuller, *Journal of Non-Newtonian Fluid Mechanics*, 2002, **102**, 135–148.

31 S. Melle, O. G. Calderón, M. A. Rubio and G. G. Fuller, *Physical Review E*, 2003, **68**, 041503.

32 A. K. Vuppu, A. A. Garcia and M. A. Hayes, *Langmuir*, 2003, **19**, 8646–8653.

33 S. Melle and J. E. Martin, *The Journal of Chemical Physics*, 2003, **118**, 9875–9881.

34 I. Petousis, E. Homburg, R. Derks and A. Dietzel, *Lab on a Chip*, 2007, **7**, 1746.

35 T. G. Kang, M. A. Hulsen, P. D. Anderson, J. M. J. den Toonder and H. E. H. Meijer, *Physical Review E*, 2007, **76**, 066303.

36 N. Casic, S. Schreiber, P. Tierno, W. Zimmermann and T. M. Fischer, *EPL (Europhysics Letters)*, 2010, **90**, 58001.

37 H. Abdi, R. Soheilian, R. M. Erb and C. E. Maloney, *Physical Review E*, 2018, **97**, 032601.

38 A. Yethiraj, *Soft Matter*, 2007, **3**, 1099.

39 M. Wang, L. He and Y. Yin, *Materials Today*, 2013, **16**, 110–116.

40 A. Imperio, L. Reatto and S. Zapperi, *Physical Review E*, 2008, **78**, 021402.

41 G. L. Hunter and E. R. Weeks, *Reports on Progress in Physics*, 2012, **75**, 066501.

42 D. Du, D. Li, M. Thakur and S. L. Biswal, *Soft Matter*, 2013, **9**, 6867.

43 K. Han, Y. T. Feng and D. R. J. Owen, *International Journal for Numerical Methods in Engineering*, 2010, **84**, 1273–1302.

44 D. Du, F. Toffoletto and S. L. Biswal, *Physical Review E*, 2014, **89**, 043306.

45 E. E. Keaveny and M. R. Maxey, *Journal of Computational Physics*, 2008, **227**, 9554–9571.

46 Z. M. Sherman, D. Ghosh and J. W. Swan, *Langmuir*, 2018, **34**, 7117–7134.

47 T. G. Kang, M. A. Hulsen, J. M. den Toonder, P. D. Anderson and H. E. Meijer, *Journal of Computational Physics*, 2008, **227**, 4441–4458.

48 H. V. Ly, F. Reitich, M. R. Jolly, H. T. Banks and K. Ito, *Journal of Computational Physics*, 1999, **155**, 18.

49 X. Luo, A. Beskok and G. E. Karniadakis, *Journal of Computational Physics*, 2010, **229**, 3828–3847.

50 S. Kang and Y. K. Suh, *International Journal for Numerical Methods in Fluids*, 2011, **67**, 58–73.

51 D. Du, P. He, Y. Zeng and S. L. Biswal, *Journal of Magnetism and Magnetic Materials*, 2016, **417**, 100–105.

52 L. H. P. Cunha, I. R. Siqueira, T. F. Oliveira and H. D. Ceniceros, *Physics of Fluids*, 2018, **30**, 122110.

53 L. H. P. Cunha, I. R. Siqueira, F. R. Cunha and T. F. Oliveira, *Physics of Fluids*, 2020, **32**, 073306.

54 D. Du and S. L. Biswal, *Physical Review E*, 2014, **90**, 033310.

55 J. Faraudo, J. S. Andreu and J. Camacho, *Soft Matter*, 2013, **9**, 6654.

56 J. Faraudo, J. S. Andreu, C. Calero and J. Camacho, *Advanced Functional Materials*, 2016, **26**, 3837–3858.

57 J. S. Andreu, J. Camacho and J. Faraudo, *Soft Matter*, 2011, **7**, 2336.

58 J. Ge, L. He, J. Goebl and Y. Yin, *Journal of the American Chemical Society*, 2009, **131**, 3484–3486.

59 L. He, M. Wang, J. Ge and Y. Yin, *Accounts of Chemical Research*, 2012, **45**, 1431–1440.

60 F. L. Calderon, T. Stora, O. Mondain Monval, P. Poulin and J. Bibette, *Physical Review Letters*, 1994, **72**, 2959–2962.

61 D. Li, C. N. Lam and S. L. Biswal, *Soft Matter*, 2010, **6**, 239–242.

62 H. Zhang and M. Widom, *Physical Review E*, 1995, **51**, 2099–2103.

63 A. Darras, E. Opsomer, N. Vandewalle and G. Lumay, *The European Physical Journal E*, 2019, **42**, 123.

64 A. Darras, J. Fiscina, M. Pakpour, N. Vandewalle and G. Lumay, *The European Physical Journal E*, 2016, **39**, 47.

65 H. Morimoto, T. Maekawa and Y. Matsumoto, *Physical Review E*, 2003, **68**, 061505.

66 H. Morimoto, K. Katano and T. Maekawa, *The Journal of Chemical Physics*, 2009, **131**, 034905.

67 S. Relle, S. B. Grant and C. Tsouris, *Physica A*, 1999, **270**, 427–443.

68 F. Martínez-Pedrero, A. El-Harrak, J. C. Fernández-Toledano, M. Tirado-Miranda, J. Baudry, A. Schmitt, J. Bibette and J. Callejas-Fernández, *Physical Review E*, 2008, **78**, 011403.

69 C. P. Reynolds, K. E. Klop, F. A. Lavergne, S. M. Morrow, D. G. A. L. Aarts and R. P. A. Dullens, *The Journal of Chemical Physics*, 2015, **143**, 214903.

70 K. Shahrivar, E. Carreón-González, J. R. Morillas and J. de Vicente, *Soft Matter*, 2017, **13**, 2677–2685.

71 J. H. E. Promislow, A. P. Gast and M. Fermigier, *The Journal of Chemical Physics*, 1995, **102**, 5492–5498.

72 S. Melle, M. A. Rubio and G. G. Fuller, *Physical Review Letters*, 2001, **87**, 115501.

73 K. Shahrivar, E. Carreón-González and J. de Vicente, *Smart Materials and Structures*, 2017, **26**, 105031.

74 P. Domínguez-García, J. M. Pastor and M. A. Rubio, *The European Physical Journal E*, 2011, **34**, 36.

75 P. Domínguez-García, S. Melle, J. M. Pastor and M. A. Rubio, *Physical Review E*, 2007, **76**, 051403.

76 E. Climent, M. R. Maxey and G. E. Karniadakis, *Langmuir*, 2004, **20**, 507–513.

77 F. Martínez-Pedrero, M. Tirado Miranda, A. Schmitt and J. Callejas Fernández, *The Journal of Chemical Physics*, 2006, **125**, 084706.

78 D. Liu, M. R. Maxey and G. E. Karniadakis, *Journal of Micromechanics and Microengineering*, 2005, **15**, 2298–2308.

79 T. Vicsek and F. Family, *Physical Review Letters*, 1984, **52**, 1669–1672.

80 E. Brunet, G. Degré, F. Okkels and P. Tabeling, *Journal of Colloid and Interface Science*, 2005, **282**, 58–68.

81 F. Martínez-Pedrero, M. Tirado-Miranda, A. Schmitt and J. Callejas-Fernández, *Physical Review E*, 2007, **76**, 011405.

82 G. Helgesen, A. T. Skjeltorp, P. M. Mors, R. Botet and R. Jullien, *Physical Review Letters*, 1988, **61**, 1736–1739.

83 P. Meakin, T. Vicsek and F. Family, *Physical Review B*, 1985, **31**, 564–569.

84 S. Miyazima, P. Meakin and F. Family, *Physical Review A*, 1987, **36**, 1421–1427.

85 S. Fraden, A. Hurd and R. Meyer, *Physical Review Letters*, 1989, **63**, 2373–2376.

86 M.-C. Miguel and R. Pastor-Satorras, *Physical Review E*, 1999, **59**, 826–834.

87 J. Černák, G. Helgesen and A. T. Skjeltorp, *Physical Review E*, 2004, **70**, 031504.

88 R. M. Erb, M. D. Krebs, E. Alsberg, B. Samanta, V. M. Rotello and B. B. Yellen, *Physical Review E*, 2009, **80**, 051402.

89 K. Shahrivar, E. Carreón-González and J. de Vicente, *Microfluidics and Nanofluidics*, 2017, **21**, 120.

90 E. M. Furst and A. P. Gast, *Physical Review E*, 2000, **62**, 6916–6925.

91 J. M. Laskar, J. Philip and B. Raj, *Physical Review E*, 2009, **80**, 041401.

92 D. Du, E. Hilou and S. L. Biswal, *Physical Review E*, 2016, **93**, 062603.

93 H. Singh, P. E. Laibinis and T. A. Hatton, *Langmuir*, 2005, **21**, 11500–11509.

94 C. Wilhelm, J. Browaeys, A. Ponton and J.-C. Bacri, *Physical Review E*, 2003, **67**, 011504.

95 A. Vázquez-Quesada, T. Franke and M. Ellero, *Physics of Fluids*, 2017, **29**, 032006.

96 M. Doi and S. Edwards, *The Theory of Polymer Dynamics*, Oxford University Press, Oxford, 1st edn, 1986.

97 C. E. Sing, L. Schmid, M. F. Schneider, T. Franke and A. Alexander-Katz, *Proceedings of the National Academy of Sciences*, 2010, **107**, 535–540.

98 L. Cohen-Tannoudji, E. Bertrand, L. Bressy, C. Goubault, J. Baudry, J. Klein, J.-F. Joanny and J. Bibette, *Physical Review Letters*, 2005, **94**, 038301.

99 C. Goubault, P. Jop, M. Fermigier, J. Baudry, E. Bertrand and J. Bibette, *Physical Review Letters*, 2003, **91**, 260802.

100 T. Yang, T. O. Tasci, K. B. Neeves, N. Wu and D. W. M. Marr, *Langmuir*, 2017, **33**, 5932–5937.

101 S. Huang, G. Pessot, P. Cremer, R. Weeber, C. Holm, J. Nowak, S. Odenbach, A. M. Menzel and G. K. Auernhammer, *Soft Matter*, 2016, **12**, 228–237.

102 E. M. Furst, C. Suzuki, M. Fermigier and A. P. Gast, *Langmuir*, 1998, **14**, 7334–7336.

103 T. Yang, D. W. Marr and N. Wu, *Colloids and Surfaces A: Physicochemical and Engineering Aspects*, 2018, **540**, 23–28.

104 S. L. Biswal and A. P. Gast, *Physical Review E*, 2004, **69**, 041406.

105 F. Gittes, B. Mickey, J. Nettleton and J. Howard, *The Journal of Cell Biology*, 1993, **120**, 923–934.

106 C. P. Brangwynne, G. H. Koenderink, E. Barry, Z. Dogic, F. C. MacKintosh and D. A. Weitz, *Biophysical Journal*, 2007, **93**, 346–359.

107 D. Li, S. Banon and S. L. Biswal, *Soft Matter*, 2010, **6**, 4197.

108 S. L. Biswal and A. P. Gast, *Physical Review E*, 2003, **68**, 021402.

109 M. Roper, R. Dreyfus, J. Baudry, M. Fermigier, J. Bibette and H. A. Stone, *Journal of Fluid Mechanics*, 2006, **554**, 167.

110 A. Cebers, *Journal of Physics: Condensed Matter*, 2003, **15**, S1335–S1344.

111 D. Vella, E. du Pontavice, C. L. Hall and A. Goriely, *Proceedings of the Royal Society A: Mathematical, Physical and Engineering Sciences*, 2014, **470**, 20130609.

112 M. Roper, R. Dreyfus, J. Baudry, M. Fermigier, J. Bibette and H. A. Stone, *Proceedings of the Royal Society A: Mathematical, Physical and Engineering Sciences*, 2008, **464**, 877–904.

113 M. Belovs and A. Cēbers, *Physical Review E*, 2006, **73**, 051503.

114 A. Cebers and K. Erglis, *Advanced Functional Materials*, 2016, **26**, 3783–3795.

115 B. H. McNaughton, K. A. Kehbein, J. N. Anker and R. Kopelman, *The Journal of Physical Chemistry B*, 2006, **110**, 18958–18964.

116 A. Zaben, G. Kitenbergs and A. Cēbers, *Soft Matter*, 2020, **16**, 4477–4483.

117 P. Tierno, J. Claret, F. Sagués and A. Cēbers, *Physical Review E*, 2009, **79**, 021501.

118 G. Helgesen, P. Pieranski and A. T. Skjeltorp, *Physical Review Letters*, 1990, **64**, 1425–1428.

119 W. A. Shelton, K. D. Bonin and T. G. Walker, *Physical Review E*, 2005, **71**, 036204.

120 A. Cebers, *Current Opinion in Colloid & Interface Science*, 2005, **10**, 167–175.

121 A. Cēbers and H. Kalis, *The European Physical Journal E*, 2011, **34**, 30.

122 J. M. Dempster, P. Vázquez-Montejo and M. Olvera de la Cruz, *Physical Review E*, 2017, **95**, 052606.

123 P. Vázquez-Montejo, J. M. Dempster and M. O. de la Cruz, *Physical Review Materials*, 2017, **1**, 064402.

124 J. Elgeti, R. G. Winkler and G. Gompper, *Reports on Progress in Physics*, 2015, **78**, 056601.

125 E. Lauga, *Annual Review of Fluid Mechanics*, 2016, **48**, 105–130.

126 L. Zhang, J. J. Abbott, L. Dong, B. E. Kratochvil, D. Bell and B. J. Nelson, *Applied Physics Letters*, 2009, **94**, 064107.

127 S. Tottori, L. Zhang, F. Qiu, K. K. Krawczyk, A. Franco-Obregón and B. J. Nelson, *Advanced Materials*, 2012, **24**, 811–816.

128 S. L. Biswal and A. P. Gast, *Analytical Chemistry*, 2004, **76**, 6448–6455.

129 R. Dreyfus, J. Baudry, M. L. Roper, M. Fermigier, H. A. Stone and J. Bibette, *Nature*, 2005, **437**, 862–865.

130 E. Gauger and H. Stark, *Physical Review E*, 2006, **74**, 021907.

131 M. Vilfan, A. Potočnik, B. Kavčič, N. Osterman, I. Poberaj, A. Vilfan and D. Babič, *Proceedings of the National Academy of Sciences*, 2010, **107**, 1844–1847.

132 N. Coq, A. Bricard, F.-D. Delapierre, L. Malaquin, O. du Roure, M. Fermigier and D. Bartolo, *Physical Review Letters*, 2011, **107**, 014501.

133 A. Babataheri, M. Roper, M. Fermigier and O. Du Roure, *Journal of Fluid Mechanics*, 2011, **678**, 5–13.

134 J. Dobnikar, A. Snezhko and A. Yethiraj, *Soft Matter*, 2013, **9**, 3693.

135 B. Bharti and O. D. Velev, *Langmuir*, 2015, **31**, 7897–7908.

136 M. Fermigier and A. P. Gast, *Journal of Colloid and Interface Science*, 1992, **154**, 18.

137 M. Hagenbüchle and J. Liu, *Applied Optics*, 1997, **36**, 7664.

138 E. M. Furst and A. P. Gast, *Physical Review E*, 1998, **58**, 3372–3376.

139 J. de Vicente, D. J. Klingenberg and R. Hidalgo-Alvarez, *Soft Matter*, 2011, **7**, 3701.

140 Z. M. Sherman and J. W. Swan, *ACS Nano*, 2016, **10**, 5260–5271.

141 J. H. E. Promislow and A. P. Gast, *Langmuir*, 1996, **12**, 4095–4102.

142 H. Kim, M. Sau and E. M. Furst, *Langmuir*, 2020,

acs.langmuir.0c01616.

143 M. B. Bannwarth, S. Utech, S. Ebert, D. A. Weitz, D. Crespy and K. Landfester, *ACS Nano*, 2015, **9**, 2720–2728.

144 A. Al Harraq, J. G. Lee and B. Bharti, *Science Advances*, 2020, **6**, eaba5337.

145 A. K. Agarwal and A. Yethiraj, *Physical Review Letters*, 2009, **102**, 198301.

146 J. E. Martin, R. A. Anderson and R. L. Williamson, *The Journal of Chemical Physics*, 2003, **118**, 1557–1570.

147 J. E. Martin, E. Venturini, G. L. Gulley and J. Williamson, *Physical Review E*, 2004, **69**, 021508.

148 A. T. Pham, Y. Zhuang, P. Detwiler, J. E. S. Socolar, P. Charbonneau and B. B. Yellen, *Physical Review E*, 2017, **95**, 052607.

149 K. A. Komarov and S. O. Yurchenko, *Soft Matter*, 2020, **16**, 8155–8168.

150 K. A. Komarov, N. P. Kryuchkov and S. O. Yurchenko, *Soft Matter*, 2018, **14**, 9657–9674.

151 I. M. Kulić and M. L. Kulić, *Physical Review Letters*, 2013, **111**, 198301.

152 F. J. Maier and T. M. Fischer, *Soft Matter*, 2016, **12**, 614–618.

153 S. H. Klapp, *Current Opinion in Colloid & Interface Science*, 2016, **21**, 76–85.

154 F. Martinez-Pedrero, A. Ortiz-Ambriz, I. Pagonabarraga and P. Tierno, *Physical Review Letters*, 2015, **115**, 138301.

155 J. N. Israelachvili, *Intermolecular and Surface Forces*, Academic Press, 1992.

156 F. Martínez-Pedrero, J. Benet, J. E. F. Rubio, E. Sanz, R. G. Rubio and F. Ortega, *Physical Review E*, 2014, **89**, 012306.

157 J. M. Kosterlitz, *Journal of Physics C: Solid State Physics*, 1973, **6**, 1181–1203.

158 D. R. Nelson and B. I. Halperin, *Physical Review B*, 1979, **19**, 2457–2484.

159 A. P. Young, *Physical Review B*, 1979, **19**, 1855–1866.

160 N. P. Kryuchkov, F. Smallenburg, A. V. Ivlev, S. O. Yurchenko and H. Löwen, *The Journal of Chemical Physics*, 2019, **150**, 104903.

161 V. J. Anderson and H. N. W. Lekkerkerker, *Nature*, 2002, **416**, 811–815.

162 B. Li, D. Zhou and Y. Han, *Nature Reviews Materials*, 2016, **1**, 1–13.

163 J.-L. Barrat and J.-P. Hansen, *Basic Concepts for Simple and Complex Liquids*, Cambridge University Press, 2003.

164 B. Li, X. Xiao, S. Wang, W. Wen and Z. Wang, *Physical Review X*, 2019, **9**, 031032.

165 J. W. Cahn and J. E. Hilliard, *The Journal of Chemical Physics*, 1958, **28**, 258–267.

166 J. Yan, S. C. Bae and S. Granick, *Soft Matter*, 2015, **11**, 147–153.

167 S. Jäger, H. Stark and S. H. L. Klapp, *Journal of Physics: Condensed Matter*, 2013, **25**, 195104.

168 X. J. A. Janssen, A. J. Schellekens, K. van Ommering, L. J. van IJzendoorn and M. W. J. Prins, *Biosensors and Bioelectronics*, 2009, **24**, 1937–1941.

169 M. M. van Oene, L. E. Dickinson, F. Pedaci, M. Köber, D. Dulin, J. Lipfert and N. H. Dekker, *Physical Review Letters*, 2015, **114**, 218301.

170 M. Reichert and H. Stark, *Physical Review E*, 2004, **69**, 031407.

171 F. Martinez-Pedrero and P. Tierno, *Physical Review Applied*, 2015, **3**, 051003.

172 T. O. Tasci, P. S. Herson, K. B. Neeves and D. W. M. Marr, *Nature Communications*, 2016, **7**, 10225.

173 T. O. Tasci, D. Disharoon, R. M. Schoeman, K. Rana, P. S. Herson, D. W. M. Marr and K. B. Neeves, *Small*, 2017, **13**, 1700954.

174 V. F. Cardoso, A. Francesko, C. Ribeiro, M. Bañobre-López, P. Martins and S. Lanceros-Mendez, *Advanced Healthcare Materials*, 2018, **7**, 1700845.

175 H. Massana-Cid, F. Meng, D. Matsunaga, R. Golestanian and P. Tierno, *Nature Communications*, 2019, **10**, 2444.

176 C. A. Brisbois, M. Tasinkevych, P. Vázquez-Montejo and M. Olvera de la Cruz, *Proceedings of the National Academy of Sciences*, 2019, **116**, 2500–2505.

177 B. M. Teo, D. J. Young and X. J. Loh, *Particle & Particle Systems Characterization*, 2016, **33**, 709–728.

178 B. Jang, E. Gutman, N. Stucki, B. F. Seitz, P. D. Wendel-García, T. Newton, J. Pokki, O. Ergeneman, S. Pané, Y. Or and B. J. Nelson, *Nano Letters*, 2015, **15**, 4829–4833.

179 H. Kim, J. L. Bauer, P. A. Vasquez and E. M. Furst, *Journal of Physics D: Applied Physics*, 2019, **52**, 184002.

180 F. Vereda, J. de Vicente and R. Hidalgo-Álvarez, *ChemPhysChem*, 2009, **10**, 1165–1179.

181 M. Abbas and G. Bossis, *Physical Review E*, 2017, **95**, 062611.

182 A. Pal, T. Zinn, M. A. Kamal, T. Narayanan and P. Schurtenberger, *Small*, 2018, **14**, 1802233.

183 K. Watanabe, H. Ishii, M. Konno, A. Imhof, A. van Blaaderen and D. Nagao, *Langmuir*, 2017, **33**, 296–302.

184 J. Yan, S. C. Bae and S. Granick, *Advanced Materials*, 2015, **27**, 874–879.

185 A. B. Pawar and I. Kretzschmar, *Langmuir*, 2008, **24**, 355–358.

186 J. Zhang, E. Luijten and S. Granick, *Annual Review of Physical Chemistry*, 2015, **66**, 581–600.

187 G. I. Vega-Bellido, R. A. DeLaCruz-Araujo, I. Kretzschmar and U. M. Córdova-Figueroa, *Soft Matter*, 2019, **15**, 4078–4086.

188 B. Ren and I. Kretzschmar, *Langmuir*, 2013, **29**, 14779–14786.

189 T. W. Long, U. M. Cordova-Figueroa and I. Kretzschmar, *Langmuir*, 2019, **35**, 8121–8130.

190 G. Steinbach, M. Schreiber, D. Nissen, M. Albrecht, E. Novak, P. A. Sánchez, S. S. Kantorovich, S. Gemming and A. Erbe, *Physical Review E*, 2019, **100**, 012608.

191 G. Steinbach, D. Nissen, M. Albrecht, E. V. Novak, P. A. Sánchez, S. S. Kantorovich, S. Gemming and A. Erbe, *Soft Matter*, 2016, **12**, 2737–2743.

192 G. Steinbach, S. Gemming and A. Erbe, *The European Physical Journal E*, 2016, **39**, 69.

193 S. Sacanna, L. Rossi and D. J. Pine, *Journal of the American Chemical Society*, 2012, **134**, 6112–6115.

194 K. Han, C. W. Shields, N. M. Diwakar, B. Bharti, G. P. López and O. D. Velev, *Science Advances*, 2017, **3**, e1701108.

195 C. W. Shields, Y.-K. Kim, K. Han, A. C. Murphy, A. J. Scott, N. L. Abbott and O. D. Velev, *Advanced Intelligent Systems*, 2020, **2**, 1900114.

196 K. N. Al-Milaji, R. L. Hadimani, S. Gupta, V. K. Pecharsky and H. Zhao, *Scientific Reports*, 2019, **9**, 16261.

197 J. J. Martin, B. E. Fiore and R. M. Erb, *Nature Communications*, 2015, 7.

198 J. Thévenot, H. Oliveira, O. Sandre and S. Lecommandoux, *Chemical Society Reviews*, 2013, **42**, 7099.

199 H.-N. An, J. Groenewold, S. J. Picken and E. Mendes, *Soft Matter*, 2014, **10**, 997–1005.

200 M. M. Schmauch, S. R. Mishra, B. A. Evans, O. D. Velev and J. B. Tracy, *ACS Applied Materials & Interfaces*, 2017, **9**, 11895–11901.

201 D. Borin, *Philosophical Transactions of the Royal Society A: Mathematical, Physical and Engineering Sciences*, 2020, **378**, 20190256.

202 J. Kim, S. E. Chung, S.-E. Choi, H. Lee, J. Kim and S. Kwon, *Nature Materials*, 2011, **10**, 747–752.

203 J. A.-C. Liu, J. H. Gillen, S. R. Mishra, B. A. Evans and J. B. Tracy, *Science Advances*, 2019, **5**, eaaw2897.

204 D. Du, E. Hilou and S. L. Biswal, *Soft Matter*, 2018, **14**, 3463–3470.

205 A. F. Demirors, P. Beltramo and H. R. Vutukuri, *ACS Appl. Mater. Interfaces*, 2017, 7.

206 K. Han, C. W. S. Iv and O. D. Velev, *Adv. Funct. Mater.*, 2018, 14.

207 Y. Yang, A. T. Pham, D. Cruz, C. Reyes, B. J. Wiley, G. P. Lopez and B. B. Yellen, *Advanced Materials*, 2015, **27**, 4725–4731.

208 D. Ahmed, T. Baasch, N. Blondel, N. Läubli, J. Dual and B. J. Nelson, *Nature Communications*, 2017, **8**, 770.

209 M. Driscoll, B. Delmotte, M. Youssef, S. Sacanna, A. Donev and P. Chaikin, *Nature Physics*, 2017, **13**, 375–380.

210 J. E. Martin and A. Snezhko, *Reports on Progress in Physics*, 2013, **76**, 126601.

211 B. Yigit, Y. Alapan and M. Sitti, *Soft Matter*, 2020, **16**, 1996–2004.

212 M. Driscoll and B. Delmotte, *Current Opinion in Colloid & Interface Science*, 2019, **40**, 42–57.

213 G. Kokot and A. Snezhko, *Nature Communications*, 2018, 7.

214 T. Mohorič, G. Kokot, N. Osterman, A. Snezhko, A. Vilfan, D. Babič and J. Dobnikar, *Langmuir*, 2016, **32**, 5094–5101.

215 V. Liljeström, C. Chen, P. Dommersnes, J. O. Fossum and A. H. Gröschel, *Current Opinion in Colloid & Interface Science*, 2019, **40**, 25–41.

216 A. Ortiz-Ambriz and P. Tierno, *Nature Communications*, 2016, **7**, 10575.

217 F. Martinez-Pedrero, A. Cebers and P. Tierno, *Soft Matter*, 2016, **12**, 3688–3695.

218 L. Chevry, N. K. Sampathkumar, A. Cebers and J.-F. Berret, *Physical Review E*, 2013, **88**, 062306.

219 J.-F. Berret, *Nature Communications*, 2016, **7**, 10134.

220 T. Qiu, T.-C. Lee, A. G. Mark, K. I. Morozov, R. Münster, O. Mierka, S. Turek, A. M. Leshansky and P. Fischer, *Nature Communications*, 2014, **5**, 5119.

221 K. Han, C. W. Shields, B. Bharti, P. E. Arratia and O. D. Velev, *Langmuir*, 2020, **36**, 7148–7154.

222 W. Fei, Y. Gu and K. J. Bishop, *Current Opinion in Colloid & Interface Science*, 2017, **32**, 57–68.

223 M. Shafiei Aporvari, M. Utkur, E. U. Saritas, G. Volpe and J. Stenhammar, *Soft Matter*, 2020, **16**, 5609–5614.

A Appendix

List of Variables

α	Phase Lag Angle
α_c	Critical Phase Lag Angle
α_{magic}	Magic Phase Lag Angle
β	Precessing Angle
$\beta(t)$	Time-Dependent Precessing Angle
β_{magic}	Precessing Magic Angle
χ	Effective Magnetic Susceptibility
χ_m	Magnetic Susceptibility of a Material
ε	Pair-Interaction Potential Well-depth
η	Solvent Viscosity
γ	Reduced Surface Potential
Γ_m	Magnetic Torque
Γ_v	Viscous Torque
$\hat{\mathbf{e}}$	Unit Vector
$\hat{e}_x$	x-component of Unit Vector
$\hat{e}_y$	y-component of Unit Vector
$\hat{e}_z$	z-component of Unit Vector
κ	Reciprocal of Debye Length
κ	Reciprocal of the Debye Length
λ	Magnetic Coupling Parameter
$\mathbb{M}$	Grand Potential Tensor
$\mathrm{d}\theta_L/\mathrm{d}t$	Angular Velocity of a Chain
μ	Magnetic Permeability of Medium
μ_0	Magnetic Permeability of Free Space

Ω	Angular Frequency of Chain/Cluster
ω	Angular Frequency of External Magnetic Field
ω_c	Critical Angular Frequency of External Magnetic Field
ϕ	Surface Particle Packing Fraction
ϕ_z	External Magnetic Field Phase
ϕ_{3D}	Volume Particle Packing Fraction
ψ_6	Local Bond-orientational Order Parameter
ρ_∞	Ion Concentration in Bulk Fluid
σ^M	Maxwell Stress Tensor
$\mathbf{B}$	External Magnetic Induction Field
$\mathbf{F}_i^\alpha$	Tangential Magnetic Force on Particle i in a Chain
$\mathbf{F}_i^\theta$	Tangential Magnetic Force on Particle i due to Another
$\mathbf{F}^r_{i,\text{total}}$	Total Radial Magnetic Force on Particle i
$\mathbf{F}_i^r$	Radial Magnetic Force on Particle i due to Another
$\mathbf{F}_i$	Total Magnetic Force on Particle i
$\mathbf{H}$	Total Magnetic Field
$\mathbf{H}_0$	External Magnetic Field
$\mathbf{H}_0(t)$	Time-Dependent External Magnetic Field
$\mathbf{H}_{dip}$	Magnetic Field Produced by a Dipole
$\mathbf{I}$	Identity Tensor
$\mathbf{k}$	Wave Vector
$\mathbf{M}$	Magnetization of Medium
$\mathbf{m}_i$	Dipole Moment of Particle i
$\mathbf{n}$	Normal Vector
$\mathbf{r}_{ij}$	Distance Vector between Dipoles i and j
Ma	Mason Number
Ma_c	Critical Mason Number
Mn	Magnetoelastic Number
Re	Reynolds Number
θ	Angle between $\mathbf{H}_0$ and $\mathbf{r}_{ij}$
θ_6	Local Orientation of Particle in Cluster
θ_{ik}	Angle between Vector connecting Particles i and k, and the Positive x-axis
θ_L	Angle between a Chain and the Positive x-axis
θ_{magic}	Magic Angle between $\mathbf{H}_0$ and $\mathbf{r}_{ij}$
ϑ	Angle between r_{ij} and the Precessing Axis
ζ	Magnetic Potential Field
A	Area
a	Particle radius
D	Diffusion Coefficient
E	Young's Modulus
EI	Bending Rigidity
f	Frequency
$g(r)$	Radial Pair Distribution Function
$G_N(t)$	Number of Chains with N Particles at Time t
$g_6(r)$	Bond-orientational Correlation Function
H_0	External Magnetic Field Strength
$H_0(t)$	Time-Dependent External Magnetic Field Strength
H_{max}	Maximum External Magnetic Field Strength
H_{min}	Minimum External Magnetic Field Strength
H_{xy}	External Magnetic Field Strength in-plane
H_z	External Magnetic Field Strength out-of-plane
I	Moment of Inertia
k_B	Boltzmann Constant
L	Contour Length
l_p	Persistance Length
L_s	Minkowski Functional: Characteristic Length
m_i	Magnitude of Dipole Moment of Particle i
N	Number of Particles
n	Number of Chain Fragments
N^*	Chain Length
N_n	Number of Nearest Neighbors
n_b	Number of Bending Modes in a Linked Chain
p	Minkowski Functional: Perimeter
r	Distance from Center of Particle
R_0	Initial Average Interparticle Spacing
R_1	Maximum Capture Radius
R_c	Capture Radius
r_{ij}	Center-to-center Interparticle Distance between Particles i and j

r_l	Lateral Separation Distance between Chains
$S(\mathbf{k})$	Structure Factor
$S(t)$	Size-weighted Average Chain Length
T	Temperature
t	Time
T^*	Effective Dimensionless Temperature
t_B	Diffusion-limited Aggregation's Characteristic Time-scale
t_{det}	Deterministic Aggregation's Characteristic Time-scale
t_{off}	Pulse-off Time of Oscillating External Magnetic Field
U	Potential Energy
U_l	Lateral Interaction Potential Between Chains
U_{ij}	Potential Energy Between Interacting Particles i and j
U_{mag}	Total Magnetic Interaction Potential for a Particle in a Chain
U_{min}	Minimum Potential Energy
V	Particle Volume
X	Minkowski Functional: Euler Characteristic
y	Position Along a Chain
z	Dynamic Scaling Exponent